Hierarchical Multiscale Modeling of Ni-base Superalloys

A Thesis

Presented to

The Academic Faculty

by

Jin E. Song

In Partial Fulfillment

of the Requirements for the Degree

Master of Science in the

School of Mechanical Engineering

Georgia Institute of Technology

August, 2010

Hierarchical Multiscale Modeling of Ni-base Superalloys

Approved by:

Dr. David L. McDowell, Advisor
School of Mechanical Engineering
Georgia Institute of Technology

Dr. Ken Gall
School of Mechanical Engineering
Georgia Institute of Technology

Dr. Richard W. Neu
School of Mechanical Engineering
Georgia Institute of Technology

Date Approved: July 5, 2010

ACKNOWLEDGEMENTS

First, I would like to thank my advisor Prof. David L. McDowell with a great support and guidance to complete this thesis. I would also like to thank the reading committee members Prof. Richard W. Neu and Prof. Ken Gall for their time, guidance and for understanding the delay of publishing this thesis.

Furthermore, I appreciate the sponsorship of Pratt & Whitney, with AFRL as prime contractor, for the MAI project.

Lastly, I want to thank my friends and family for their support and patience.

TABLE OF CONTENTS

LIST OF TABLES

LIST OF FIGURES

SUMMARY

Ni-base superalloys are widely used in components of aircraft gas turbine engines due to high creep resistance and strength at intermediate temperatures. Because manufacturing and developing the components of gas turbine engines is a competitive design problem, a constitutive model that can accurately anticipate material behavior is valuable. Additionally, Ni-base superalloys demonstrate multiple deformation mechanisms under operating conditions, and these add complexity to predictions of material behavior. Therefore, it is desirable to develop a constitutive model that can accurately capture multiple deformation mechanisms and that is applicable to materials at the component level.

This thesis develops a hierarchical multiscale modeling scheme that can capture microstructural details and associated phenomena at fine scales and that can implicitly convey information to the macroscale model without directly accessing the model at each length scale. In order to establish a hierarchical constitutive model, models at different length scales have to be formulated to capture desired phenomena that are considered to be important in the application. For disk alloys, high temperature strength and fatigue resistance are priorities. Therefore, a modified Chaboche-type macroscale viscoplastic model that can be calibrated to multiple loading histories under different conditions is first introduced. For this macroscale model, emphasis is placed on capturing a broad range of responses adequately without modeling fine scale phenomena. In order to

capture complex phenomena, various relevant internal state variables are introduced. This work also develops a hierarchical parameter estimation scheme which can effectively calibrate the macroscale model parameters to multiple experimental data in order to link complex relations between the observed physical phenomena (e.g., relaxation, hardening, softening) and parameters.

Similarly, at a finer length scale, this study formulates a microstructure-sensitive crystal plasticity model to predict the macroscale response of the material of interest. Observed deformation mechanisms under conditions pertinent to the application of Ni-base superalloys are reviewed, and microtwinning is added to the crystal plasticity model to supplement the existing ability capture deformation by dislocation glide. The microtwinning process is studied with regard to triggering by the dislocation dissociation at tertiary and secondary γ' precipitates. To this end, the mechanisms of the dissociation process are analyzed based on phase field model simulation results provided by Prof. Y. Wang at the Ohio State University, and the characteristics are implemented to the crystal plasticity model via the microtwinning shearing rate. The microtwinning-incorporated crystal plasticity model is then analyzed by conducting multiple simulations on a polycrystal finite element model to understand the evolution of state variables, and the added microtwinning formulation is tested to establish preliminary validity.

CHAPTER 1

INTRODUCTION

Ni-base superalloys are extensively used in hot sections of aircraft gas turbine engines (Reed, 2006). Among many components made with Ni-base superalloys, turbine disks, which hold turbine blades, are considered to be among the most important components of turbine engines. In general, disks in a turbine engine experience temperatures of 650°C or above in the rim, while the mechanical stress exerted on the bore reaches 1.0 GPa (Reed, 2006). Therefore, materials with high temperature strength and superior creep resistance are desired in disk alloy applications.

The efficiency and performance of turbine engines are significantly improved if the turbine entry temperature (TET) is (Reed, 2006). Hence, there have been countless attempts to design a new material that can endure higher temperatures, while maintaining the strength and other mechanical properties at high levels for applications. A newly developed disk alloy still requires a series of comprehensive testing analyses to ensure performance and durability under various conditions, which can involve enormous research and experimental resources.

In general, disk alloys can be processed or treated to yield different microstructure attributes, and hence different material properties. However, to achieve improved material properties of a disk alloy by tailoring microstructure attributes, the material structure property relations have to be very thoroughly understood. In the past, trial-and-

error based experimental analysis was often used to understand the relation between the thermomechanical process steps given to a disk alloy and its mechanical properties. In last few decades, computing power has been used to improve our capacity to model disk alloys. In the mean time, analysis tools and techniques such as high resolution transmission electron microscopy have been used to investigate operative deformation mechanisms in great details, and new information regarding deformation modes and configurations has been obtained. As a result of such developments, constitutive models based on observed deformation mechanisms associated with interactions of dislocations with γ' precipitates can be formulated. Furthermore, with the aid of improved computational power, it is becoming possible to implement elements of physically-based, fine scale constitutive models at a component size level. These improvements in our capacity to model fine scale phenomena in a constitutive relation and to use constitutive relations to correlate and predict responses of specimens offer support for materials design and microstructure-sensitive lifting.

Disk alloys having identical chemical composition but subjected to different heat treatments can possess different material properties; they may even exhibit different deformation mechanisms. Therefore, there have been many attempts to formulate a constitutive relation at a fine length scale (e.g., microstructure-sensitive crystal plasticity model) for a disk alloy to reflect multiple phenomena observed under different conditions (e.g., temperature, stress/strain level or strain rate), and these can significantly affect material behavior at multiple length scales. In order to effectively incorporate such constitutive relations over multiple length scales, a hierarchical modeling scheme can be considered. Multilevel hierarchical modeling can provide an effective tool to capture

microstructure details and associated phenomena at multiple length scales (McDowell, 2008).

Multilevel hierarchical modeling can be further extended to support location-specific design of a disk in which different material properties are desired at different locations. Each disk in a jet engine has an outer 'rim' section where high temperature strength and creep tolerance are considered important, and an inner thick section called the 'bore' where higher cyclic strain amplitude is expected and fatigue resistance is important at a somewhat lower temperature. Consequently, the rim region is heat treated to contain slightly larger grains and finer γ' precipitates, and the bore section is treated to contain smaller grains with coarser γ' precipitates. In order to achieve different microstructures within a single component, a manufacturing technique such as a dual heat treat (DHT) is implemented (Mourer and Williams, 2004). A design tool that can utilize such a technique based on a concurrent modeling scheme is still in a preliminary stage. However, using a multilevel hierarchical modeling scheme, it is envisioned that a disk can be concurrently designed both in terms of material and component geometry aspects, suggesting trade-offs in gradients of microstructure and component design for the application. This hierarchical modeling scheme should have the ability to access information from fine scales, such as phase field or crystal plasticity models, and implicitly deliver it to the component level. Consequently, the layout of the microstructure morphology and the mechanical dimensions of a disk may be tailored to achieve improved optimum performance for a given application and given component mass.

This research focuses on employing models framed at multiple length scales that account for the operative deformation mechanisms of a Ni-base disk alloy and support a hierarchical modeling scheme that can estimate macroscopic mechanical responses. The main objectives of the research are to:

- Develop a rate dependent macroscopic internal state variable (ISV) constitutive model with all essential features.
- Analyze state variable evolution in the crystal plasticity model, and develop a grain-scale polycrystal plasticity model including microtwinning induced shearing rate to capture complex loading histories.
- Establish a multiscale hierarchical parameter estimation scheme to estimate material parameters for multiple complex loading histories, building on prior work of Shenoy (2006).
- Suggest a hierarchical multiscale model of a constitutive relation which can implicitly link a crystal plasticity to a macroscale ISV constitutive model.

The thesis is organized as follows:

- Chapter 2 briefly reviews the hierarchical modeling framework developed by Shenoy (2006) and suggests the framework for this research. The 3rd generation Ni-base superalloy considered in this work is also introduced briefly.
- Chapter 3 reviews the macroscopic constitutive model and discusses employing proper ISVs for the disk alloy applications. Development of the hierarchical parameter estimation scheme for the calibration process is also introduced.

- Chapter 4 reviews deformation mechanisms observed in disk alloys and introduces an enhanced crystal plasticity model for modeling their responses.
- Chapter 5 analyzes the evolution of shear strains and internal state variables of the crystal plasticity model based on preliminary strain-controlled and stress-controlled simulations.

CHAPTER 2

BACKGROUND

2.1 Multiple Level Hierarchical Modeling

Multiple level hierarchical modeling can be a desirable tool to formulate a set of constitutive relations addressing phenomena over multiple length scales. Fine scale qualities such as microstructure attributes can greatly affect the deformation mechanism, which in turn determines the performance of components. Component level simulations are impractical using models that explicitly incorporate microstructure. Hence, quantitatively relating the material process to the microstructure and to the mechanical response using a hierarchical modeling scheme can be practical in disk alloy design and analysis. Hierarchical modeling, however, requires contributions from models at each length scale, which can take great effort and time to achieve. Hierarchical modeling is an especially attractive design scheme for disk alloy applications, because (1) the performance of an aircraft gas turbine engine is directly related to the material's capability to withstand the operating conditions, (2) multiple material properties have to be considered, and these are difficult to capture with a constitutive relation at single length scale, (3) multiple deformation mechanisms exist in operating conditions, and transition of deformation mechanisms can critically affect the performance of applications, (4) the cost of disks in aircraft gas turbine engines forms a substantial portion of the cost of the entire engine (Reed, 2006), and it is advantageous to push

design to near the limit of the component or material to draw more performance or durability out of the same cost, and (5) broad applicability is desired – once established, this hierarchical multiscale model can be used for other disk alloys or for other applications with only slight modifications to the framework which saves cost and time in development of new analysis schemes.

Shenoy (2006) developed a framework that linked a microstructure-sensitive crystal plasticity model to a macroscale ISV model using simulations of both actual and large number of virtual microstructures to train an Artificial Neural Network (ANN) for disk alloy IN-100 with variations in microstructure at 650°C. The ANN was then need to relate microstructure attributes to macroscopic ISV model parameters to facilitate a microstructure sensitive macroscopic ISV model. The framework was formulated to improve life predictions of this disk alloy. The hierarchical modeling scheme involved a grain scale polycrystal plasticity model that capture the variations in attributes including grain size, γ' precipitate size distribution, and the γ' precipitate volume fraction. The procedures for establishing the link between the microstructure-sensitive crystal plasticity model and the empirical macroscale model are as follows:

1. Using the calibrated crystal plasticity model, a set of stress-strain curves are generated for a range of microstructures. This is considered as the virtual database of stress-strain curves.
2. Using the parameter estimation process, macroscale ISV model parameters are estimated for the stress-strain-time curve in the virtual database of stress-strain time responses created by the calibrated crystal plasticity model.

3. An ANN is trained to map the parameters of the macroscale ISV model to microstructure attributes.
4. The trained ANN can generate Chaboche-type macroscale ISV model parameters for any input of microstructure attributes.

The multilevel hierarchical modeling scheme of this research is based on derived from Shenoy's framework, but with some extensions for different conditions including a range of temperature, input loading histories, and different desired outcomes of the modeling scheme. The multilevel hierarchical modeling has not been fully tested, due to limited experimental data to date, as we are considering a new alloy system. Therefore, the goal of this thesis is to outline and exercise a hierarchical modeling scheme that will be applicable to microstructure-sensitive modeling of new systems.

An overview of the hierarchical modeling scheme is depicted in Figure 2.1. Assuming various experimental datasets with different temperature and loading conditions, both the polycrystal plasticity model and a Chaboche-type macroscale ISV model are calibrated to experimental data. The crystal plasticity model is linked to the phase field model which conveys information from a finer scale to the length scale of grains. The estimated parameters of the macroscale ISV model are virtually linked via an ANN to changes in the temperature, microstructure attributes, and loading conditions. The trained ANN should be able to generate associated macroscale ISV model parameters for a given combination of temperature, loading condition and microstructure attributes.

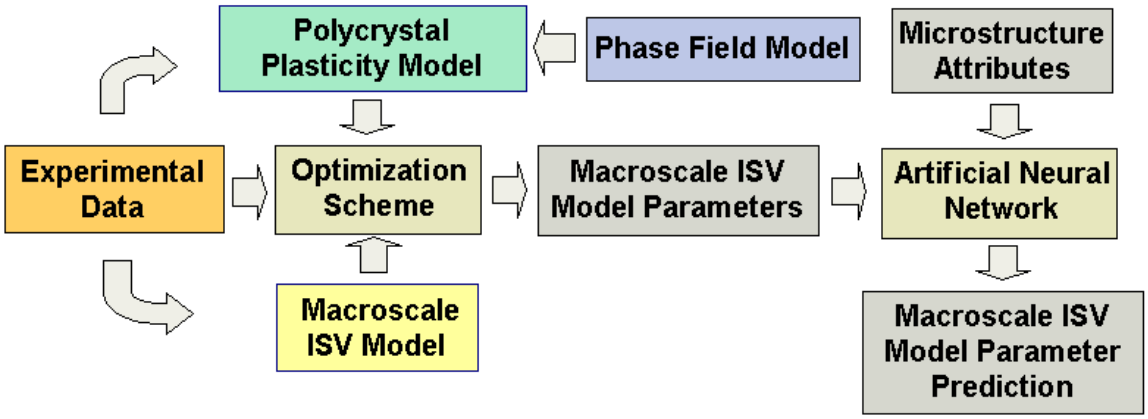

Figure 2.1 Hierarchical multiscale modeling scheme for linking from the length scale of dislocations and precipitates to the macroscale.

2.2 Material Microstructures and Details

The third generation disk alloy ME3 is the primary material considered for the modeling and analysis in this work. In 1998, the ME3 alloy was developed in the NASA/General Electric/Pratt & Whitney High Speed Research/Enabling Propulsion Materials (HSR/EPM) disk program aiming for extended durability at 600°C to 700°C (Gabb et al., 2004). The new material contained Ta which greatly reduced dwell fatigue crack propagation rate (Reed, 2006). Also, with relatively high Co concentration (18.2%), the γ' solvus temperature was lowered and the heat treatment window could be widened to enable super-solvus heat treatment and dual microstructure heat treatments. Its grain size and γ′ precipitate size distribution and volume fractions (approximately 50%) can be controlled with consolidation, extrusion, forging and heat treatment processes (Gabb et al., 2004). As in other Ni-base superalloys, the precipitate sizes of ME3 are also divided into three groups: primary γ' precipitates from 1 to 10 microns diameter (not applicable if heat treated at supersolvus temperature), secondary

precipitates ranging from 0.1 to 1 microns form during quench (highly influenced by cooling rate and path), and tertiary precipitates (less than 0.1 microns) (Gabb et al., 2004). Considered microstructure variations of ME3 can be divided into two groups: slow cooled bore and fast cooled rim. When the material is supersolvus heat treated, the bore is observed to have larger secondary γ′ precipitates with less volume fraction, and the rim has smaller sized but larger volume fraction of γ′ precipitates.

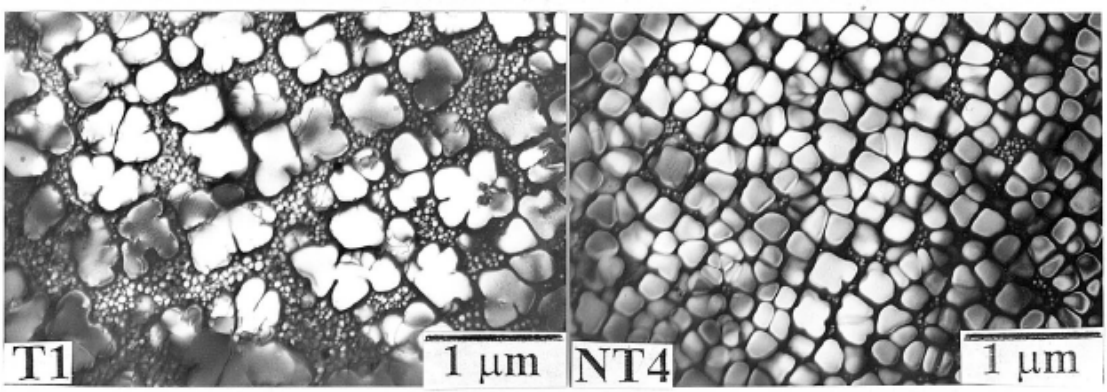

Figure 2.2 Microstructure of bore and rim specimens from supersolvus heat treated disks S100-bore (left), rim (right) (Gabb et al., 2004).

Among widely used disk alloys, ME3, ME16 and René104 are sometimes referred to as third generation disk alloys which are characterized by the similar chemical compositions. As these are relatively new materials, their analysis is not thoroughly available yet, and the operative deformation mechanisms are not as well categorized, as will be discussed in Chapter 4.

CHAPTER 3

MACROSCALE INTERNAL STATE VARIABLE CONSTITUTIVE MODEL FOR NI-BASE SUPERALLOY AND HIERARCHICAL PARAMETER ESTIMATION SCHEME

3.1 Introduction

Constitutive models for various metals and alloys at the macroscopic length scale are designed to capture complex nonlinear and time-dependent material behavior during inelastic deformation. Macroscale constitutive models generally involve single or multi-yield surfaces associated with viscoplastic strain rate, and they consist of a flow rule and internal state variables (ISVs). At the macroscale, the physical representation of heterogeneity at finer length scales is not explicitly addressed. Therefore, material homogeneity is assumed locally in such models. Macroscopic constitutive models can be applied at length scales up to the component level, if uniform averaged response and properties of the representative volume element (RVE) at local material points can be assured.

Macroscopic models capture complicated inelastic behavior by introducing various types of evolving ISVs. Using the viscoplastic flow potential, the inelastic strain rate is controlled by the evolution of ISVs, each of which describes physical phenomena typically observed in alloys or metals under deformation. Constants associated with the ISV evolution equations are typically experimentally determined, owning to the many-

body nature of the problem (e.g., large number of dislocation growth and interactions with different sizes/shapes of precipitates and grains). Furthermore, macroscopic models do not have explicit microstructure dependence implemented (although this can be introduced with an ISV). Consequently, when microstructure is varied, the constitutive model parameters have to be determined anew. If physical relations for ISVs over a broad range of microstructure are to be realized, a substantial number of experimental data sets must be available.

In spite of somewhat indirect connection to evolving microstructure attributes, macroscopic ISV constitutive models are favored in many industrial applications due to computational efficiency and ease of implementation.

3.2 Two-Term Flow Rule Model

The macroscale viscoplastic model is written for clarity in terms of uniform temperature and small strains, although formulated for arbitrary large strain (small elastic strain). In this section, we present the uniaxial form of the model, assuming isotropic linear elasticity. The strain rate is assumed to have elastic and inelastic components, i.e.,

$$\dot{\varepsilon}_t = \dot{\varepsilon}_e + \dot{\varepsilon}_p \tag{3.1}$$

And the stress is assumed to be related to the elastic modulus and strain by

$$\sigma = E(\varepsilon_t - \varepsilon_p) = E\varepsilon_e \tag{3.2}$$

The inelastic strain rate is obtained from the derivative of a viscoplastic potential with respect to stress and is related to the overstress in a highly nonlinear fashion (Chaboche, 1989). A two-term flow rule model is introduced with distinctive overstresses and temperature dependence such that (cf. Chaboche, 1989)

$$\dot{\varepsilon}_p = A_1 \left\langle \frac{\sigma_{v1}}{K_1} \right\rangle^{n_1} \operatorname{sgn}(\sigma - \chi) + A_2 \left\langle \frac{\sigma_{v2}}{K_2} \right\rangle^{n_2} \operatorname{sgn}(\sigma - \chi) \tag{3.3}$$

where K_1 and K_2 are drag stresses, n_1 and n_2 are flow rule exponents, and A_1 and A_2 are temperature-dependent coefficients. The direction of the inelastic strain rate is determined by sgn($\sigma - \chi$). The McCauley bracket $\langle\ \rangle$ results in zero when the value inside is negative, consequently allowing the inelastic strain rate to remain zero during elastic deformation. The flow exponents n_1 and n_2 are assigned such that $n_1 > n_2$ is satisfied always to distinguish the role of each term – the first term is capable of capturing higher stress level and strain rate responses, while the second term is more sensitive to low stress level creep and relaxation responses..

The overstresses of the flow rule in Eq. (3.3) are defined individually by

$$\begin{aligned} \sigma_{v1} &= |\sigma - \chi| - R - \kappa \\ \sigma_{v2} &= |\sigma - \chi| \\ R(0) &= \chi(0) = 0 \end{aligned} \tag{3.4}$$

Here, κ is the threshold stress representing the initial yield stress, χ is the kinematic stress (back stress) capturing the directional shift of the viscoplastic potential surface. The isotropic hardening stress, R, represents the increase (hardening) or decrease (softening) in size of the yield surface. By assigning different overstresses, each of the two terms of Eq. (3.3) are dominant at different levels of stress. The first term of the flow rule with the first overstress is effective only when the overstress is high enough to overcome the back stress, isotropic hardening stress and threshold stress. On the other hand, the second overstress is positive over a much broader stress range, owing to the fact that only the back stress needs to be overcome; but its associated inelastic strain rates are quite low. Consequently, the second term of the flow rule governs the inelastic behavior completely

when the first overstress is still negative. Once the first overstress becomes positive, however, the first term of the flow rule rapidly increases and dictates the inelastic strain rate.

3.3 State Variables

3.3.1 Back Stress Evolution

The kinematic hardening model translates the yield surface without changing its size to describe the Bauschinger effect; therefore, the back stress corresponds to the center of the yield surface. The Bauschinger effect is a phenomenon observed in metals in which the yield stress is substantially different in compression following initial tensile yielding and flow (Khan and Huang, 1995). A nonlinear kinematic hardening-rule of the Armstrong and Frederick for is employed (1966), i.e.,

$$\dot{\chi} = C\left(\alpha\dot{\varepsilon}_p - \chi\left|\dot{\varepsilon}_p\right|\right), \tag{3.5}$$

where C and α are material constants representing the rate and the saturation level of the back stress, respectively, and $\left|\dot{\varepsilon}_p\right|$ is the effective inelastic strain increment. The dynamic recovery term (or recall term) introduces the nonlinearity of the back stress evolution which allows the back stress to correctly model the Bauschinger effect.

In addition to the dynamic recovery term, a static thermal recovery term must be added to capture the recovery effect which is caused by a diffusion-assisted processes observed during dwell or creep at high temperatures (Shenoy, 2006). The combined formulation of the dynamic and static thermal recovery of kinematic hardening are first introduced by (Malinin and Khadjinsky, 1972) without explicit temperature dependence, i.e.,

$$\dot{\chi} = C\left(\alpha\dot{\varepsilon}_p - \chi\left|\dot{\varepsilon}_p\right|\right) - \beta\left|\chi\right|^{r-1}\chi \tag{3.6}$$

where β and r are temperature dependent recovery coefficients. The first two terms of the back stress govern the back stress evolution under high inelastic strain rate loads. On the other hand, when the inelastic strain rate is at a low level (e.g., long dwell period), the static thermal recovery term can become influential, and the recovery state can become prominent, depending on the magnitude of the back stress. The diffusional recovery of back stress becomes increasingly significant as temperature increases.

3.3.2 Superimposed Two-term Back Stress Model

Back stress is a multiscale phenomenon manifested at multiple length scales with contributions that are inherently passed on to coarse scale models (McDowell, 2008). In some cases, conflicts can arise if multiple phenomena are modeled using single back stress. Therefore, individual back stress terms such as Eq. (3.5) or Eq. (3.6) can be superimposed so that important manifestations are not omitted, as suggested in the work of Moosbrugger and McDowell (1988), i.e.,

$$\begin{aligned} \chi &= \sum_{i=1}^{M}\chi_i \\ \dot{\chi}_i &= C_i\left(a_i\dot{\varepsilon}_p - \chi_i\left|\dot{\varepsilon}_p\right|\right) - \beta_i\left|\chi_i\right|^{r_i-1}\chi_i \end{aligned} \tag{3.7}$$

The model suggests that any number of back stresses can be superimposed as necessary.

Lowe and Miller (1984) used two back stresses and defined them as short range and long range. Superimposing two back stress terms is also attempted to express the transition from initial yielding associated with short-range back stress (intergranular) to asymptotic plastic flow regime associated with long-range back stress (intragranular)

(McDowell, 1992). Consequently, the superimposed two-term back stress evolution can describe transitions from the rapid inelastic flow during cyclic loading to progressive hardening conditions (Chaboche, 1989). Additionally, the superimposed back stress can implicitly describe the dislocation remobilization after unloading by assigning a large back stress magnitude and plastic modulus (Chaboche, 1989).

3.3.3 Scale Effects in Back Stress Evolution

An assessment of back stress at length scales of grains is presented in the work of Haddou et al. (2004). The flow stress is divided into two components based on experimentally obtained hysteresis loops at saturated state: an isotropic stress which corresponds to the radius of the yield surface and a back stress which is responsible for the directional component of hardening. The relationship between the back stress and plastic strain amplitude ε_{pa} as a function of the average grain size, d, is analyzed and formulated in their work, following the Hall-Petch relation, i.e.,

$$\chi\left(\varepsilon_{pa}\right) = \chi_0\left(\varepsilon_{pa}\right) + k_x\left(\varepsilon_{pa}\right) d^{-0.5} \tag{3.8}$$

where χ_0, and k_x are parameters that are functions of the plastic strain amplitude ε_{pa}. In Eq. (3.8), the first term of the back stress, χ_0, is not sensitive to grain size, and is referred to as the intragranular back stress, whereas the second term with grain size dependence is the intergranular back stress and tends to evolve rapidly in early stage of straining. In contrast, the intragranular stress evolves slowly at first and increases inelastic strain increases.

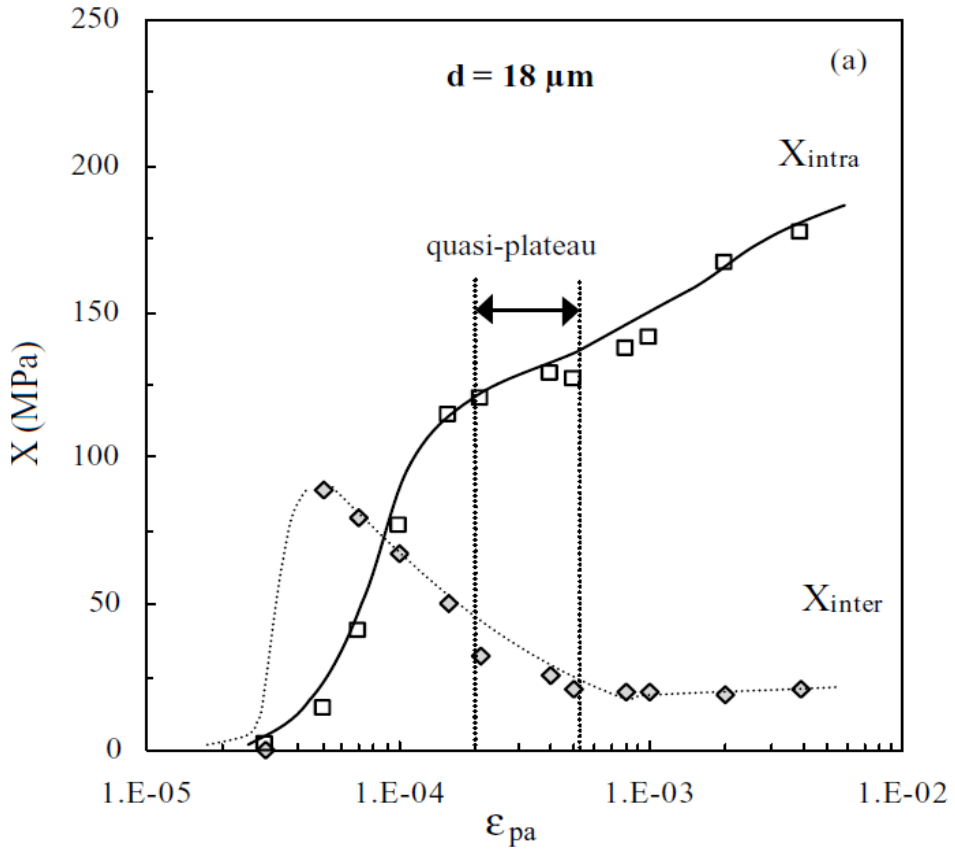

Figure 3.1 Intergranular and intragranular back stress behavior at grain size of 18 µm of polycrystalline Ni based on cyclically saturated hysteresis loops (Haddou et al., 2004).

Based on the superimposed multiple back stress model at the macroscale (Moosbrugger and McDowell, 1988) and the intragranular (long range) and intergranular (short range) back stress separation model (Haddou et al., 2004), this research uses a superimposed two-term back stress model with a rapidly evolving (short range) and a slowly evolving (long range) back stress. Due to the nature of the macroscale viscoplastic ISV model, the back stress terms are not directly related to microstructure attributes. Instead, the back stress evolution law of the macroscale model is mathematically formulated to capture both the short and long range effects.

The two term back stress model is applied with static recovery term, i.e.,

$$\dot{\chi}_1 = C_1\left(a_1\dot{\varepsilon}_p - \chi_1\left|\dot{\varepsilon}_p\right|\right) - \beta_1\left|\chi_1\right|^{r_1-1}\chi_1$$
$$\dot{\chi}_2 = C_2\left(a_2\dot{\varepsilon}_p - \chi_2\left|\dot{\varepsilon}_p\right|\right) - \beta_2\left|\chi_2\right|^{r_2-1}\chi_2 \quad (3.9)$$

$$\chi = \chi_1 + \chi_2 \quad (3.10)$$

where C_1 and C_2 control the rate of the short and long range back stress evolution towards the saturated values of a_1 and a_2, respectively, such that $C_1 > C_2$ and $a_1 < a_2$ are satisfied. The static thermal recovery terms are insignificant under high inelastic strain rate conditions (high stress magnitude and high strain rate) in which the first two terms of the back stress evolution are dominant. However, when the inelastic strain rate is low, the hardening is subdued and the static thermal recovery terms start to become prominent. When the strain rate is reduced significantly (e.g., long dwell period), the static thermal recovery terms can become dominant (Chaboche, 1989).

3.3.4 Isotropic Hardening Variable

The isotropic hardening variable, R, captures the softening or hardening of the material strength by changing the size of the yield surface with respect to the inelastic strain. The increase of the yield surface size is physically related to the evolution of the dislocation density during deformation (Cailletaud and Chaboche, 1979). The simplest form of the isotropic stress evolution model is given by (Lee and Zaverl Jr, 1978)

$$\dot{R} = b(Q - R)\left|\dot{\varepsilon}_p\right| \quad (3.11)$$

where Q is the stabilized value of the isotropic stress, and b controls the rate of the stabilization process. A constant value of Q, however, becomes invalid when the strain amplitude of the cyclic loading changes, since the stabilized value of R generally grows as the amplitude of the applied cyclic strain is increased. Moreover, the isotropic stress

also tends to saturate more rapidly when the applied strain amplitude increases (Khan and Huang, 1995). Therefore, strain amplitude dependence of the asymptotic value of the isotropic hardening variable is desired. Additionally, since the saturated value of the isotropic stress depends on the prior loading history, and the cyclic inelastic flow is related to the inelastic strain range, a relation between the isotropic hardening variable R and the memory parameter q can be given by (Chaboche, 1983; Chaboche, 1989; McDowell, 1985; Ohno, 1982)

$$\dot{Q} = \mu\left(Q_{max} - Q\right)\dot{q} \tag{3.12}$$

$$q = \max(\left|\varepsilon_p\right|, q) \tag{3.13}$$

where Q_{max} is the maximum value that Q can reach, μ controls the evolving rate of Q and q is the inelastic strain range memorization term which stores the maximum inelastic strain amplitude and enables the stress response of the maximum strain range when the strain level is varied (Chaboche, 1989).

The isotropic hardening variable should also include a recovery term to reflect the recovery of dislocation state at high temperatures (Nouailhas, 1989), i.e.,

$$\dot{R} = b(Q - R)\left|\dot{\varepsilon}_p\right| - \gamma\left|R - Q_r\right|^{m-1}\left(R - Q_r\right) \tag{3.14}$$

where γ and m are recovery constants, and Q_r is the lower bound of the stabilized value Q, so that Q lies between Q_r, incomplete recovery of state, and Q_{max} when static thermal recovery is considered. The lower bound Q_r is introduced to incorporate the microstructural recovery effect and is defined as (Nouailhas, 1989)

$$Q_r = Q - Q_r^*\left(1 - \left(\frac{Q_{max} - Q}{Q_{max}}\right)^2\right) \tag{3.15}$$

where Q_r^* is a temperature dependent material constant.

3.4 Macroscale ISV Model Implementation

The constitutive relation of the macroscale ISV model is implemented as a Fortran90 subroutine using an explicit fourth order Runge-Kutta scheme. The code (referred to as 'macro model code' hereafter) is designed to read input loading history, in either time-stress or time-strain format and to divide each input time step into sub-increments as necessary. Then, for each sub-increment, the code estimates stress or strain response based on the macroscale constitutive relation using the ISV constants provided in a separate input file. For the purpose of computational efficiency and simplicity, only uniaxial input loading histories are computed in the code. A schematic overview of the code implementation is displayed in Figure 3.3.

3.5 Weighting Scheme

The weighting scheme is slightly modified from the previously developed scheme (Shenoy et al., 2008) which was developed to characterize the loading history and to distinguishc the contribution of each data point to the calibration process. Weight factors are initially assigned by the 'macro model code' at each time increment as one of four types under strain-controlled loading conditions: (1) elastic – when the strain is inside the yield surface (applied strain below yield strain), (2) dwell period – when the amplitude of the strain rate is near zero (e.g., below 10^{-10}/s), (3) maximum strain – when the applied strain magnitude exceeds the prior maximum strain magnitude in the input loading strain

history, and (4) cyclic loading – in the remaining places of the input strain loading history when inelastic cyclic deformation is experienced as depicted in Figure 3.2.

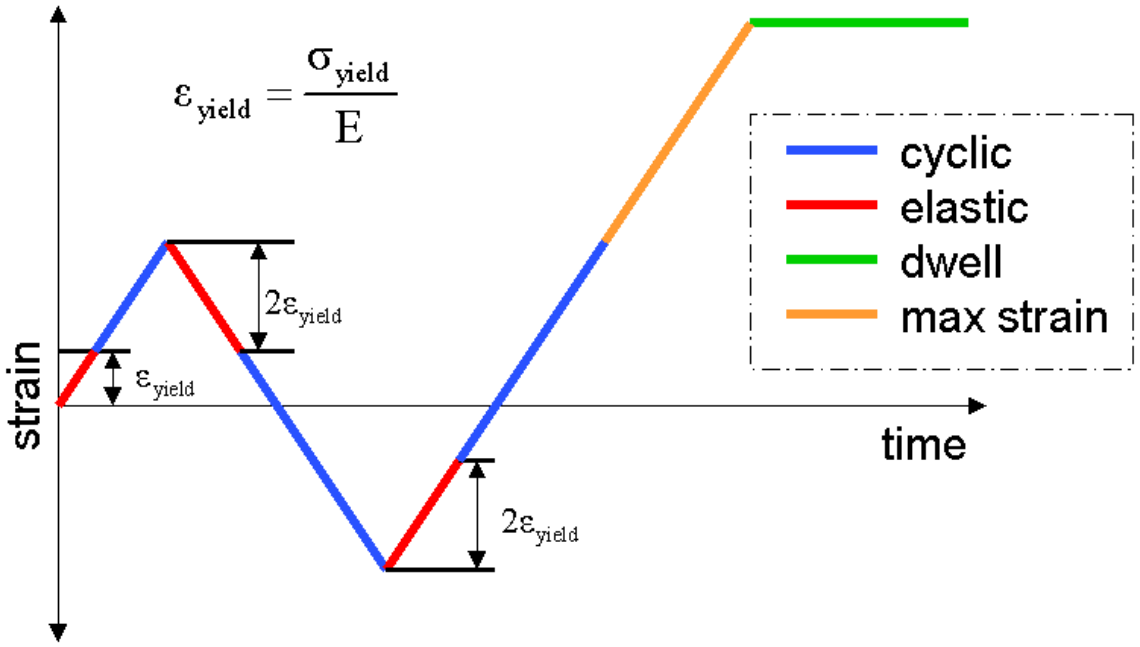

Figure 3.2 Strain characterization and weight factor assignments (Shenoy et al., 2008).

Once weighting factors are determined for all time increments, assigned weight factors are further adjusted to be sensitive to the data acquisition rate which is often a concern if the input loading data is acquired directly from experimental results. This process is performed by multiplying initially assigned weight factors by normalized time (e.g., $\Delta t / \Delta t_{ref}$).

3.6 Error Definition

In order to quantify and measure the discrepancy between the responses obtained from the macroscale constitutive relation and experimental results, the accumulated error

is computed by summing up the difference at each time increment under strain-controlled loading, i.e.,

$$\text{Accumulated Error} = \sum\left[\left(\text{weight factor}\right)^2 \cdot \left(\sigma_{\text{exp}} - \sigma_{\text{macro}}\right)^2\right] \tag{3.16}$$

If stress-controlled loading condition is considered, the accumulated error would be calculated as

$$\text{Accumulated Error} = \sum\left[\left(\text{weight factor}\right)^2 \cdot \left(\varepsilon_{\text{exp}} - \varepsilon_{\text{macro}}\right)^2\right] \tag{3.17}$$

3.7 Hierarchical Parameter Estimation Scheme

An optimization software package, ModelCenter 9.0 (Phoenix Integration, Inc., 2009), is used to calibrate the macroscopic constitutive model response to the experimental results. It does this by minimizing the accumulated error, as calculated by Eq. (3.16) or Eq. (3.17). The software can minimize or maximize selected objective(s) by altering designated variables that are bounded by user-specified upper and lower constraints. The variables (input) and the objective function (output) are linked by the two Fortran90 codes; the 'macro model code' and the 'error code,' both of which are compiled and run sequentially in ModelCenter 9. The macroscopic ISV model parameters are assigned as input variables, and the accumulated error is selected as the objective function (output) of the optimization to be minimized. The number of input variables employed in the optimization software can be determined at each session of parameter estimation. An overview of the parameter estimation scheme is depicted in Figure 3.3.

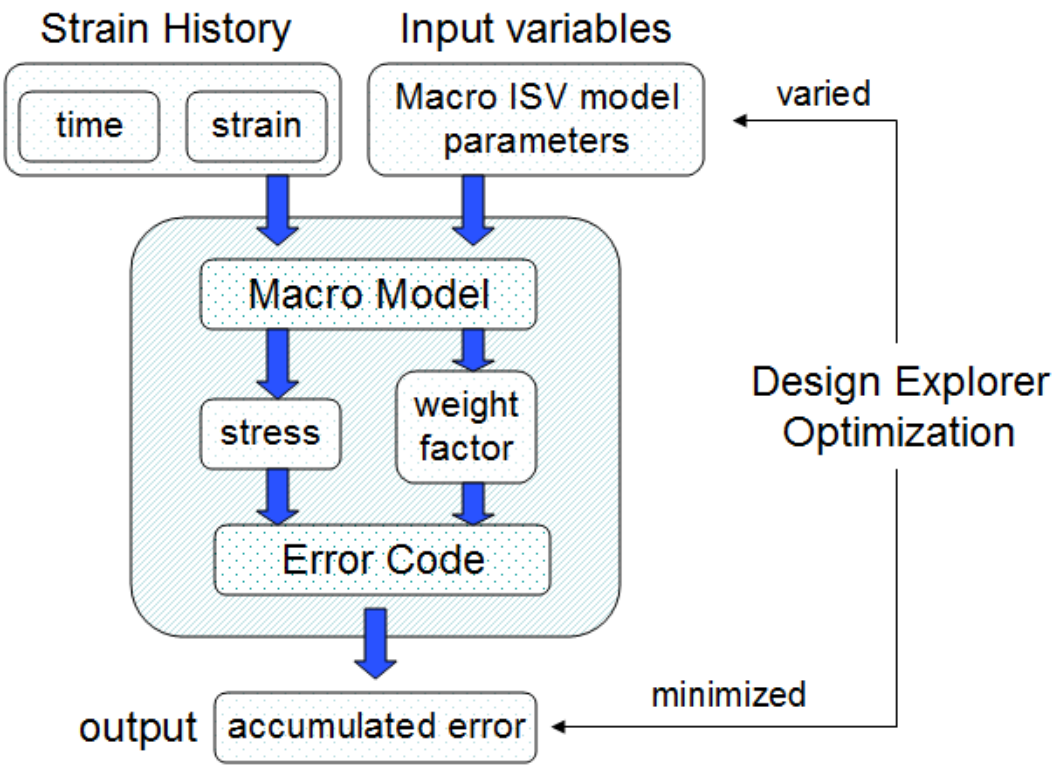

Figure 3.3 Schematic view of the parameter estimation process.

Within ModelCenter, the user can select the type of optimization algorithm to be implemented for the design problem; for the parameter estimation of this research, the 'design explorer' option is chosen, as indicated in Figure 3.3. This algorithm begins with preliminary runs of the analysis codes ('macro model code' and 'error code') to generate a surrogate model, which can be considered as a design space created by input variables and the objective function. The algorithm uses a gradient based optimization algorithm, Sequential Quadratic Programming, on the surrogate model to find and record local minima. Then, values at the local minima of the surrogate model (equivalent to design outputs) are compared to actual analysis outputs (accumulated errors). If the local minima of the surrogate model and the accumulated errors calculated by the analysis codes differ

significantly, the surrogate model is updated. The updated surrogate model is again used to find local minima, and it suggests the design solution with macroscale ISV model parameters with the minimum discrepancy (i.e., accumulated error).

3.7.1 Input Loading History Partitioning (Level 1 and Level 2)

The experimental loading history is often designed to be complex so that realistic loading conditions can be implemented, and various physical phenomena are captured with a limited number of experimental runs. However, experimental data with such a complex loading history often introduce difficulties in model calibration. In experiments with metals, especially Ni-base superalloys, cyclic loading with multiple strain amplitudes are often employed with a constant strain rate or sometimes two different constant strain rates, followed by dwell time period(s). As discussed in the previous sections, ISVs capture specific physical phenomena, and the parameters associated with the state variables are distinctively sensitive in those sections of the loading history where the characteristic roles of ISVs are highlighted. On this basis, a complex strain history can be considered as a collection of simple loading histories, sequentially applied (i.e., history effect) with distinctive characteristics; hence they can be divided into several partitions (e.g., initial, cyclic 1, dwell 1, cyclic 2, dwell 2).

Instead of conducting parameter estimation on the entire experimental response, quantifying individual discrepancies (accumulated errors) and optimizing the input variables on the divided partitions of experimental response can be much more reliable. Also, the overall calibration process can be controlled by monitoring the progress of the parameter estimation on each partition. On this basis, parameter estimation can be

conducted at two levels: (1) partition 'level 1' and (2) full experiment 'level 2' - one full experiment without partitioning. While minimizing the absolute discrepancy at the full experiment level (level 2) is the main goal of the calibration process, fitting input variables to individual partitions at level 1 can also be an effective way to estimate the input variables.

Depending on the complexity of the input loading history of the experimental data, only the experimental result is divided into partitions. Each partition is treated as an individual entity of the parameter estimation and is assigned input variables to generate an accumulated error using Eq. (3.16). Once the accumulated error for each partition is computed, the optimization algorithm of the ModelCenter suggests the ISV model parameter set with the minimum accumulated error for that particular partition. In general, these parameter sets obtained from different partitions of the same experimental result do not correspond. Therefore, after parameter estimation at the partition level (level 1) is completed, the accumulated errors of all partitions are combined into a single number quantifying the overall discrepancy of the entire experiment, i.e.,

$$\text{Total Error}=\sum_{n=1}^{\#\text{of subsections}}\left[\frac{\left(\text{accumulated error}\right)_n}{\left(\text{elapsed time}\right)_n}\times\left(\text{weight factor}\right)_n\right] \tag{3.18}$$

where the accumulated error of each partition is normalized by the length of time spent in the partition. The weight factors are manually assigned to partitions so that the emphasis of those partitions that determine the macroscale ISV model parameters can be controlled.

Minimizing the total error by combining the accumulated errors of partitions comprises level 2 parameter estimation, in which the influence of each partition is controlled outside the level 1 parameter estimation scheme. With level 1 and level 2

parameter estimation schemes executed in a hierarchical manner, a two-level parameter estimation scheme is established as depicted in Figure 3.4. The parameter estimation scheme can be applied to experimental results for a complex loading history; this results in a macroscale ISV parameter set that best represents the overall experimental response.

Some experiments can involve relatively more complex loading histories, therefore generate more partitions. When more partitions are involved, ISV evolution in subsequent partitions is affected by the evolution in prior partitions. Therefore, parameters must be calibrated to experimental data of the initial partitions to a certain degree, and then the calibrated parameters should be used as the initial value in the parameter estimation of the subsequent partitions. Therefore, parameter estimation at level 1 or level 2 is not a parallel process, but a sequential process in which the parameter estimation process of the subsequent partitions can strongly depend on estimated parameters of the prior partitions.

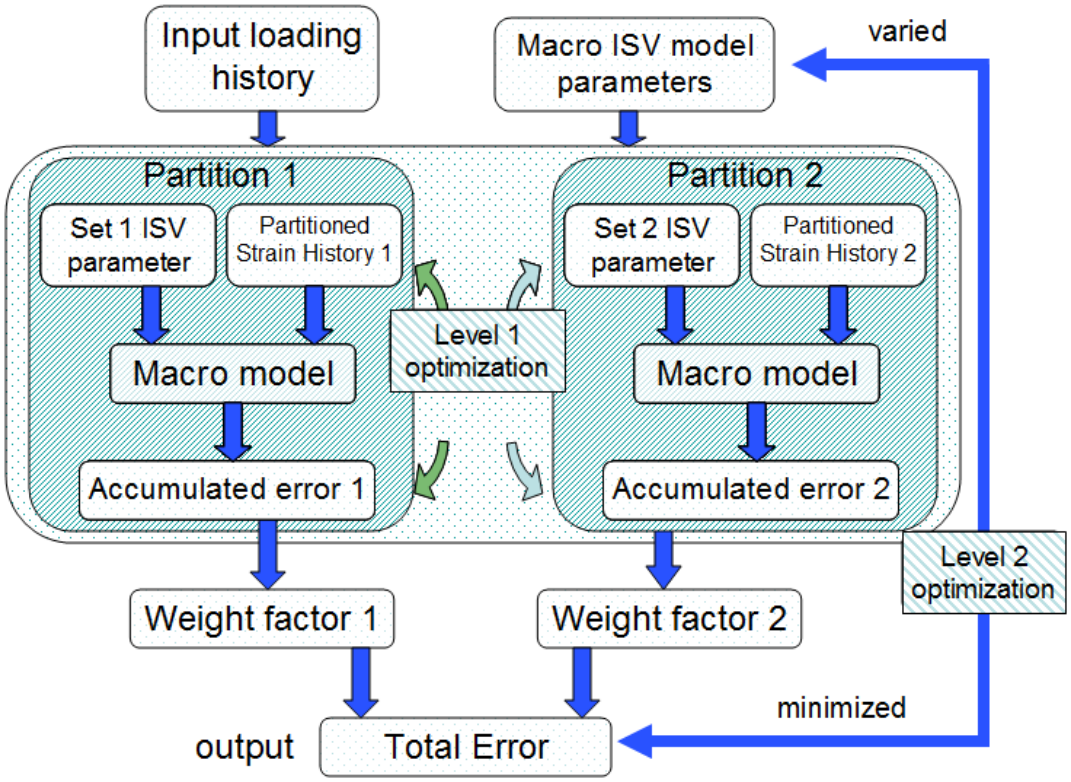

Figure 3.4 Level 1 and level 2 parameter estimation for a single partitioned experimental data.

3.7.2 Multiple Loading Histories (Level 3)

A single experiment even with a complex loading history is usually insufficient to fully characterize the deformation response of a disk alloy. Therefore, multiple experiments are conducted on identical material under various conditions (e.g., a range of strain rates, temperatures and loading histories). Furthermore, the same loading histories under same conditions should be applied to multiple microstructures to characterize the influence of microstructure and to validate microstructure-sensitive models. When the two-level parameter estimation scheme, introduced in the previous section, is applied to multiple experiments conducted on the same microstructure, multiple sets of model parameters will be obtained, which theoretically should coincide. In general, however,

the calibrated parameter sets will differ, perhaps significantly. Since a calibrated constitutive model should be sufficiently general in scope to represent the responses obtained from various experiments, the calibrated parameter sets from the different experiments have to be combined into one that satisfactorily estimates all. The process of obtaining such a parameter set introduces an additional level to the parameter estimation scheme, establishing a three-level hierarchical parameter estimation scheme, as depicted in Figure 3.5.

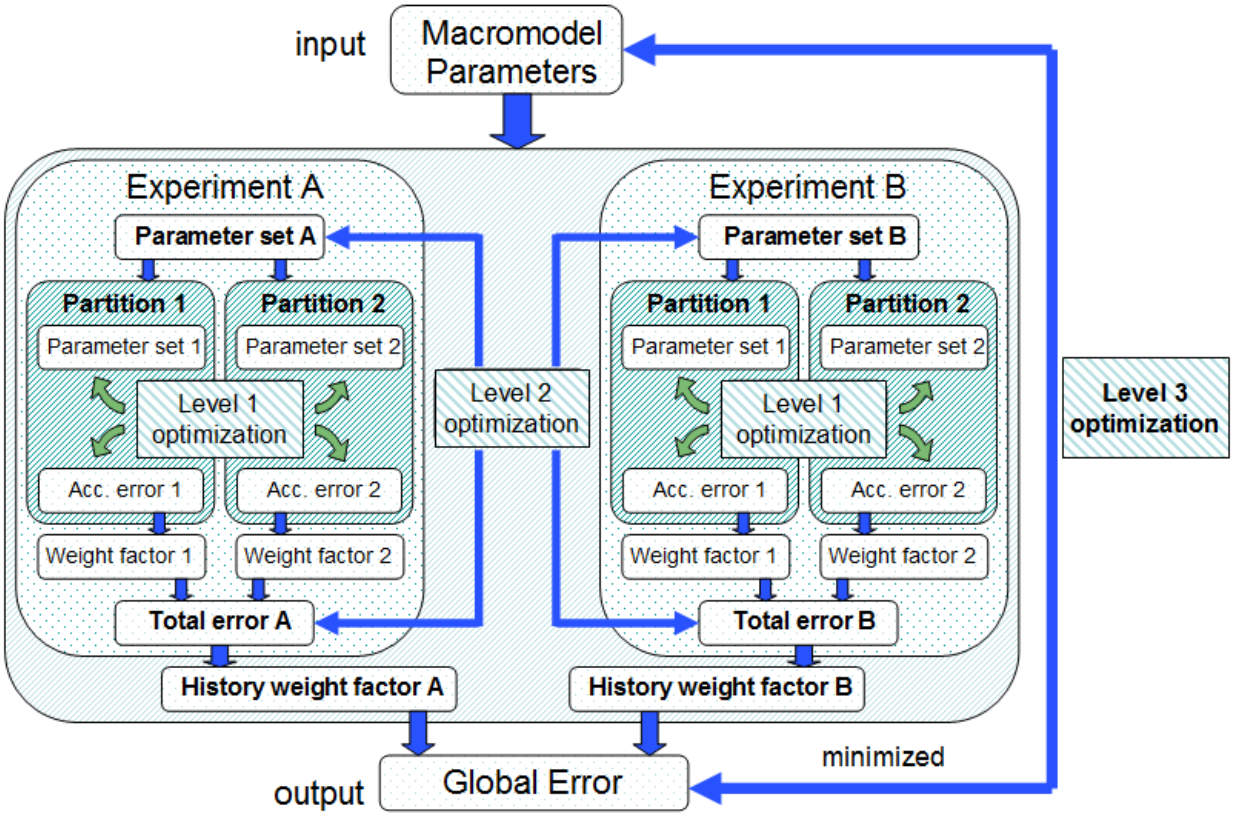

Figure 3.5 Three level hierarchical parameter estimation scheme overview for multiple experimental data sets.

As introduced in the previous section, each experimental data set for the same material involves the two-level hierarchical parameter estimation scheme, with its first level at partitions of a complex loading history and the second level on individual full experiments. The top level (level 3) rectifies results from multiple experiments and minimizes the global error by varying the macroscale ISV model parameters.

The global error is calculated based on the total errors of experiments (level 2) obtained from Eq. (3.18)), i.e.,

$$\text{Global Error} = \sum_{m=1}^{\#\text{ of experiments}} \left[\frac{\left(\text{Total Error}\right)_m}{\sum_{n=1}^{\#\text{ of partitions}} \left(\text{weight factor}_n\right)} \times \left(\text{history weight factor}\right)_m \right] \tag{3.19}$$

where the total errors from level 2 are normalized by the sum of weight factors assigned at the partitions of the experiments. The history weight factors are manually assigned to the experimental responses, and they are multiplied to the normalized total errors. Therefore, the global error is the summation of the normalized total errors with the different contributions from experiments. The history weight factors are assigned such that a certain characteristic behavior of the relevant applications of the material can be emphasized. For instance, fitting to relaxation dominant experiments should be prioritized over high rate cyclic experiments, if such loading and deformation behavior are critical to the application.

The three-level hierarchical parameter estimation scheme introduced in this section can concurrently incorporate all experimental data of a material into a single constitutive relation. Implementation of such a hierarchical parameter estimation scheme also prevents constitutive models from being calibrated with undue focus on a single response

or a small number of experimental responses in a way that restricts its applicability to a narrow range of conditions. Therefore, the multilevel parameter estimation scheme can establish a trade-off among experiments by balancing local and global fittings.

3.8 Parameter Clustering

The systematic hierarchical parameter estimation scheme introduced in the previous section provides an effective tool for calibrating parameters to multiple experiments with complex loading histories. However, even with such a hierarchical parameter estimation scheme, fitting all parameters simultaneously to experimental data is undesirable regardless of the complexity of the associated loading history, mainly because many parameters in a constitutive relation are nonlinear and discontinuous in their domain of the design space. Concurrently fitting such parameters can be computationally overwhelming, because characterizing a multi-dimensional design space generated by numerous parameters with uncertain domains and then searching for local minima in the design space can be extremely difficult. Therefore, parameters are divided into several groups (called clusters) based on the physical phenomena they represent, and the parameter estimation is conducted on a smaller number of parameters so that the design space can remain relatively simple.

Parameters can be clustered for the parameter estimation scheme in various ways depending on the loading conditions and material characteristics. In general, this process is done effectively when parameters are clustered by the state variables relevant to specific phenomena. Clusters for the macroscale ISV model are shown in Table 3.1.

Table 3.1 Clusters and parameters of the parameter clustering strategy for the macroscale ISV model.

Cluster	Parameter
Yield	κ and E
Flow rule	K_1, K_2, A_1, A_2, n_1 and n_2
Isotropic hardening	Q_{max}, b, and μ
Short range back stress	a_1 and C_1
Long range back stress	a_2 and C_2
Back stress static thermal recovery	β_1, β_2, r_1 and r_2
Isotropic hardening static thermal recovery	Qr*, γ and m

Clusters can be subdivided further into smaller groups, if necessary, and a parameter can be in multiple clusters without being confined to a single cluster. Different types of clustering strategies have been attempted based on the Chaboche-type macroscale model (Nouailhas, 1989; Tong et al., 2004; Zhan and Tong, 2007; Zhao et al., 2001).

As discussed in the previous section, parameters associated with ISVs are distinctively sensitive under relevant conditions where the characteristics of the ISVs are highlighted. For example, some parameters are more influential in regions of high stress when the inelastic strain is above a certain value, while other parameters are less prominent under the same conditions but dominant at lower stress levels. Hence, the domains of parameters should be also taken into account, and parameters in a cluster should have similar domains.

The clustering strategy can be most effective when used with the hierarchical parameter estimation scheme introduced in the previous section, especially at level 1 of the hierarchical parameter estimation scheme, where a complex loading history is divided into several simple partitions. For such a localized and simplified loading history at partition level, only one or few clusters will be distinctively influential to the model response, whereas many other clusters have negligible or no effect at all on the response and on the accumulated error of the particular partition of the loading history. Consequently, except for the one or two critical clusters, the other clusters can be excluded from the input variables of parameter estimation and the design space for the particular partition, which can reduce the computational load and enhance the optimization speed of ModelCenter significantly.

The strategy of clustering parameters is also very effective at level 2 of the hierarchical parameter estimation scheme where an individual experiment is optimized. As explained earlier, it is difficult, if possible, to fully characterize a material's behavior with a single experiment; hence multiple experiments are conducted on each material. Experiments are designed in a way that each can reveal specific behaviors of the material. Consequently, each experiment has different relative importance of clusters that are engaged in determining the model response, and employing only the effective clusters with an appropriate set of weight factors can greatly improve the effectiveness of the parameter estimation process.

In the following subsections, clusters of parameters are briefly introduced and the process of calibrating each parameter to given experimental data in conjunction with the hierarchical parameter estimation scheme is presented.

3.8.1 Yield Cluster

The values of parameters associated with yielding (κ and E) can be estimated graphically from a simple tensile/compressive loading response, or at any unloading region, if the strain rate is sufficiently high. In the case of the macroscale ISV model, the elastic modulus E can be approximated by measuring the slope of the linear stress-strain response under monotonic loading, whereas the initial yield strength κ can be estimated by measuring the deviation from linearity in the loading or unloading region at higher strain rates. The estimated parameters can be further refined using the level 1 parameter estimation scheme with a strain history partitioned to slightly beyond the initial load, where E and κ most influence the accumulated error of the partition. Once the parameters of the yield cluster are estimated, they are excluded from the input variables of the parameter estimation, so that they do not affect the calibration process any further. This is mainly because the optimization software tends to adjust the decrease in stiffness observed at high temperatures and high strains by lowering the parameters of the yield cluster while compromising elastic behavior.

3.8.2 Isotropic Hardening Cluster

The isotropic hardening cluster includes parameters associated with the isotropic hardening evolutions including Q_{max}, b, and μ. The first step of estimating the isotropic hardening cluster is to check whether hardening or softening is observed in the experimental response. In the macroscopic ISV model, depending on how prominently the hardening or softening develops, the magnitude and sign of Q_{max} and the saturation rates μ and b can be estimated. As described previously, Q_{max} represents the asymptotic

value of the isotropic stress, which can be estimated by measuring the increase or decrease in stress level between the initial cycle and the saturated cycle. The saturation rates μ and b can be estimated using experimental responses that contain cycles from initial load to saturation. Depending on the condition of the load, however, the asymptotic value of the isotropic stress and the saturation rates, even for the same material can be estimated differently, as the increase or decrease of the stress level between the initial cycle and the saturated cycle does not necessarily represent Q_{max}. the absolute saturation value of Q. Additionally, this cluster tends to have multiple combinations of parameters that can successfully capture the hardening or softening demonstrated within a partition. Therefore, the parameters need to be also estimated at level 2 and level 3 of the parameter estimation scheme so that the asymptotic value of the isotropic stress and the saturation rates can represent all of the available experimental responses.

Furthermore, at high temperatures, depending on strain rates and strain levels, hardening of the isotropic stress and the short range back stress can become indistinguishable. In other words, an increase in the short range back stress will have to accompany a decrease in the isotropic hardening and vice versa to balance out the total hardening. Therefore, the isotropic hardening cluster and the back stress cluster should not be estimated independently even at the partition level of the parameter estimation scheme (level 1).

At any step of level 1 or level 2 of the parameter estimation scheme, the initially estimated isotropic hardening parameters are only tentative, as the subsequent parameter estimation process on the back stress cluster can considerably alter the overall output response. Therefore, once the back stress cluster is estimated, the isotropic hardening

cluster should be updated with the new back stress cluster. Similarly, the back stress cluster also has to be updated when any changes are made to the isotropic hardening cluster in an iterative fashion.

3.8.3 Back Stress Cluster

In the macroscale model, the back stress is decomposed into long and short range back stresses. Therefore, the back stress parameters are divided into two clusters: a_1 and C_1 in the short range back stress cluster, and a_2 and C_2 in the long range back stress cluster.

The short range back stress reaches its saturation value rapidly. Therefore, parameters associated with the short range back stress, a_1 and C_1, should be estimated in the early phase of a cyclic partition of a loading history where the short range back stress evolves to the asymptotic value C_1 rapidly. On the other hand, the long range back stress normally has an extremely low evolving rate a_2; thus, its asymptotic value C_2 is not reached even at high strain/stress levels. Therefore, parameters in the short range back stress can be estimated in the early phase of the first cyclic partition where the long range back stress is still in its initial stage of evolution. Once the short range back stress cluster is estimated with the initial cyclic response, the long range back stress cluster can be estimated with partitions of subsequent cycles in which the long range stress starts to influence the response.

In the early phase of parameter estimation process for the back stress cluster, assigning proper initial values of the input variables can greatly alter the path of the process, some of which can be referenced from previous calibrated models (Schwertel

and Schinke, 1996). Also, the asymptotic values of the long and short range back stresses have to be closely monitored and constrained at all levels of the hierarchical parameter estimation scheme.

Even with proper initial input variables assigned and with both back stresses evolving at reasonable rates, many combinations of the evolving rates and the asymptotic values of the back stresses, especially at the partition level (level 1), can result in nearly identical overall responses in a limited input loading range, as in the isotropic hardening cluster. Therefore, the parameter estimation on each back stress cluster has to be conducted further at levels 2 and level 3 of the parameter estimation scheme to ensure validity under different strain rates, and strain or stress levels.

3.8.4 Flow Rule Cluster

The flow rule cluster for the macroscale model should be sufficiently estimated after isotropic hardening and back stress clusters are calibrated to a reasonable degree. The drag stresses K_1 and K_2 should be assigned to be slightly greater than σ_{v1} and σ_{v2}, respectively, to prevent the inelastic strain rate from overshooting and diverging. The temperature dependent fitting parameters A_1 and A_2 determine the contributions of the first and second overstresses (σ_{v1} and σ_{v2}) to the inelastic strain rate and are often estimated iteratively with the drag stresses. Flow exponents n_1 and n_2 are also important in determining the degree of inelasticity represented from each term of the flow rule, and they are initially referenced from calibrated crystal plasticity model parameters and further estimated with multiple experimental data.

The flow rule clusters are subdivided into the first term cluster and the second term cluster. The first term cluster contains A_1, K_1 and n_1 and the second term cluster includes A_2, K_2 and n_2. The clusters are estimated sequentially: (1) the first term cluster is calibrated to the cyclic partitions (level 1) with high strain/stress where the second term cluster is not critically affecting the overall response, then (2) the second term cluster is calibrated to responses at low strain rates (e.g., dwell period or creep).

3.8.5 Static Thermal Recovery Cluster

Static thermal recovery clusters exist both for the isotropic hardening variable and the back stress evolution in order to capture the diffusional recovery effects observed at high temperatures and low strain rates. These recovery terms are deactivated in the early phase of the parameter estimation process until the back stress, isotropic hardening and flow rule clusters are preliminarily estimated based on partitions with higher strain rates. The parameters in the static thermal recovery cluster should be activated when partitions with dwell periods are subjected to the level 1 parameter estimation scheme. Additionally, the static thermal recovery parameters should not affect the parameter estimation process of other state variables and only limitedly effective under low rate conditions.

The back stress recovery cluster includes β_1, β_2, r_1 and r_2, where β_1, and r_1 are recovery constants for the long range back stress and β_2, and r_2 are for the short range back stress. The parameters of back stress recovery clusters are responsible for lowering the back stress magnitude at very low strain rates (e.g., below 10^{-7}/s).

The isotropic hardening static thermal recovery cluster includes parameters Q_r*, γ and m. This cluster is also estimated at low strain rates under similar conditions as those

imposed for fitting the back stress static thermal recovery clusters. When calibrated to the responses of a low strain rate loading history, γ and m are estimated first which determine the magnitude of the relaxation rate. The evolution rate of the lower asymptotic value of the isotropic hardening variable Q_r depends on the magnitude of Q_r*. Therefore, once the isotropic hardening and the magnitude of the drop in stress due to static thermal recovery are reasonably assumed, Q_r* can be estimated based on the asymptotic value of the minimum isotropic hardening variable.

3.8.6 Refining Process

With all clusters calibrated using the hierarchical parameter estimation scheme, parameter calibration must be refined further. The parameters of multiple clusters, even outside the most influential ones, can be simultaneously calibrated over partitioned loading histories (level 1) or over a an individual experiment (level 2). This is viable even with the enormous design space size, because the constraints of input variables can be tightly assigned while the accumulated errors of the so-far calibrated parameters are near the local minima. When no further improvement is observed after several iterations of calibration, the parameters of only less-relevant clusters (e.g., the short range back stress cluster and first flow rule cluster in a dwell emphasized experiment) can be calibrated simultaneously to identify unrealized interdependencies exist among the clusters.

As the last step of the calibration process, all macroscale model parameters are calibrated simultaneously over all experimental data. If the global error is improved notably in doing so, changes to material parameters must be identified, and the cluster containing the parameters that have significantly changed should be calibrated again at

level 2 and possibly at level 1, if necessary. Finally, the fully calibrated constitutive model should be implemented back to every individual experiment (level 2) involved in the parameter estimation process and visually checked to establish that the estimated parameters represent the material behavior adequately.

CHAPTER 4

POLYCRYSTAL PLASTICITY MODEL FOR THIRD GENERATION NI-BASE SUPERALLOY

4.1 Introduction

Ni-base superalloys are widely used for disks of aircraft gas turbine engines due to their high creep and fatigue resistance at a relatively high operating temperature range (600°C to 700°C). Accurate knowledge of the deformation behavior of the material under realistic operating conditions is crucial to ensure the durability and reliability of superalloys. Also the efficiency and performance of components can be improved by optimally processing existing disk alloys or developing new and improved alloys targeting desired properties. For Ni-base superalloys, various deformation mechanisms are observed depending on their microstructures, temperature, and loading conditions. The diversity is mainly caused by the complexity of interactions with γ' precipitates in the face-centered cubic γ matrix. Even though the macroscopic ISV model introduced in the previous chapter can accurately anticipate responses once calibrated, the model is not intrinsically capable of reflecting all deformation mechanisms in new generations of disk alloys, since the model is formulated to only capture the experimentally observed phenomena. Therefore, a physically based constitutive model that can properly capture transitions of multiple deformation mechanisms and that is capable of accurately

predicting responses over multiple deformation mechanisms of Ni-base superalloys is desirable.

In this chapter, deformation mechanisms commonly observed in Ni-base superalloys are reviewed, and a constitutive relation for microtwinning is formulated based on information from a phase field model. The microtwinning constitutive relation is combined with a dislocation density based crystal plasticity viscoplastic constitutive model which captures shearing dominated deformation in Ni-base superalloys. The 3D crystal plasticity model is implemented as a User MATerial subroutine (UMAT) in ABAQUS (Simulia, 2006).

4.2 Deformation Mechanisms

There have been numerous deformation mechanisms introduced at the length scale of grains to explain the complex deformation behaviors of Ni-base superalloys. Difficulties in assessing such a complex deformation mechanism mainly originate from the interaction between dislocations and γ' precipitates. Examples of suggested deformation mechanisms for Ni-base superalloys include (1) isolated faulting of the γ' precipitates, (2) shearing of γ' precipitates, (3) thermally activated microtwinning, (4) extended, continuous faulting of precipitates and matrix, (5) Orowan looping, (6) dislocation climb by-pass, and (7) formation of stacking fault ribbons (cf. Unocic et al., 2008; Kovarik et al., 2009). The aforementioned deformation mechanisms are suggested without establishing clear connections among them, as they are structured according to observed configurations under intentionally limited testing conditions, which makes it difficult to capture the transition from one mechanism to another.

Current applications of Ni-base superalloys in turbine disks require an operating temperature up to 700ºC under significant loads. Such an elevated operating temperature can be achieved by a high volume fraction of bi-modal or tri-modal γ′ particles which provide significant restriction on plastic flow by employing high energy configurations (e.g., anti-phase domain boundaries (APB), complex stacking faults (CSF), superlattice intrinsic stacking faults (SISF), and superlattice extrinsic stacking faults (SESF)), whose dominance varies depending on conditions such as temperature, stress, strain or microstructure (Unocic et al., 2008).

High energy configurations (high activation energy) affect the deformation process especially in the temperature range of 600ºC to 800ºC. The deformation mechanisms between these temperatures are complex and vary greatly depending on microstructure. Outside of this range, however, rather simple interactions between the γ′ particles and dislocation movements control the deformation process. For instance, at 800ºC or above, dislocations are observed to climb to another plane and are pinned at precipitates, which can cause the dislocations to bow between γ′ particles (Manonukul et al., 2002).

4.2.1 Deformation Mechanism at Intermediate Temperature

The deformation mechanisms at intermediate temperatures (600 to 800ºC), primarily under low stress creep condition without prior overload, can be divided into two types, depending on the microstructure attributes: microtwinning and isolated faulting as shown in Figure 4.1. According to the creep test results obtained by Viswanathan et al. (2005), isolated faulting is observed in coarse microstructures with larger γ' precipitates while microtwinning is found in fine γ' microstructures.

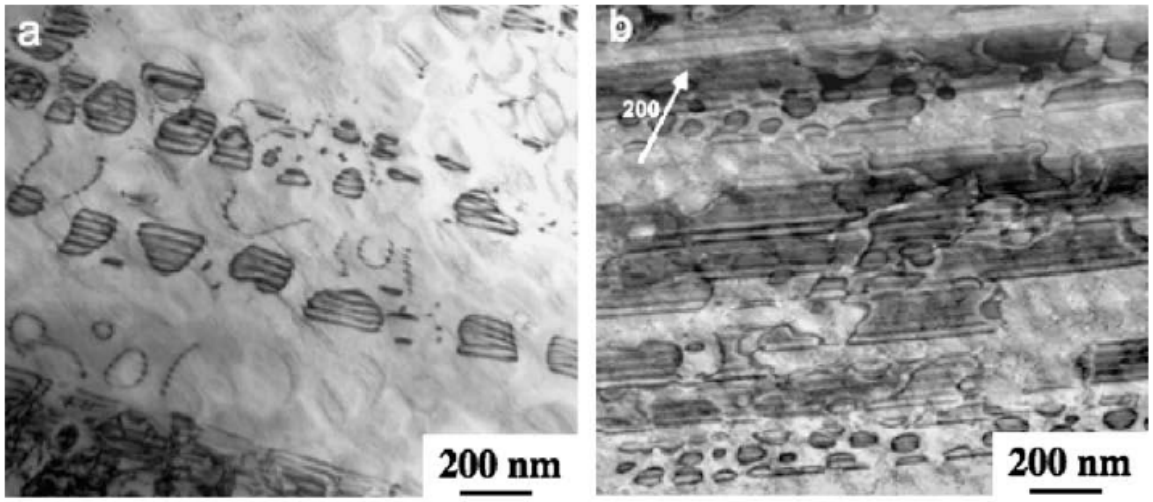

Figure 4.1 Deformation mechanisms for creep on René 88 DT: (a) isolated faulting with large γ′ precipitates, (b) microtwinning with small γ′ precipitates (Kovarik et al., 2009b).

Microtwinning is a recently understood mechanism covering a relevant range of operating conditions of polycrystalline Ni-base superalloys in disk and blade applications. Microtwinning, however, has been drawing more attention in single crystals of Ni-base superalloys in which the creep resistance is considered important (Ardakani et al., 1999; Kakehi, 2000). Kakehi (1999) observed that microtwinning is favored over dislocation slip near the temperature regime where the yield stress of Ni-base superalloys is the highest, because the critical stress for twinning becomes relatively lower than the critical stress for slip. Kolbe also suggested a diffusion-controlled microtwinning mechanism after investigating deformations on NIMONIC 105 and NIMONIC PE 16 in the temperature regime around 780ºC where the critical resolved shear stress (CRSS) starts to decrease (2001). Kolbe's suggested mechanism was not fully validated at that time, but more recently similar suggestions were made on the basis of creep loading tests by Viswanathan et al. (2005) conducted on differently cooled René 88 DT specimens to 0.5% strain at stress levels in the range of 790 to 972 MPa. The cooling rate was

observed to influence the microstructure considerably, determining the γ′ precipitate sizes and the volume fractions. Fast cooled specimens (at 205ºC/min) had finer microstructure with high tertiary γ′ volume fraction and small secondary and tertiary γ′ precipitate sizes (Viswanathan et al., 2005). A similar relation was observed in fast cooled specimens (rim) of René 104 with a noticeable improvement in creep resistance compared to the slow cooled section (bore) as shown in Figure 4.2 (Unocic et al., 2008). Transmission electron microscopy (TEM) images of tested specimens of both materials (René 88 DT and René 104) revealed that the specimens with finer γ' microstructures were deformed by highly planar faulted structures which sheared both precipitate and matrix with a/6$\langle 112 \rangle$ type Shockley partial dislocations (Unocic et al., 2008; Viswanathan et al., 2006).

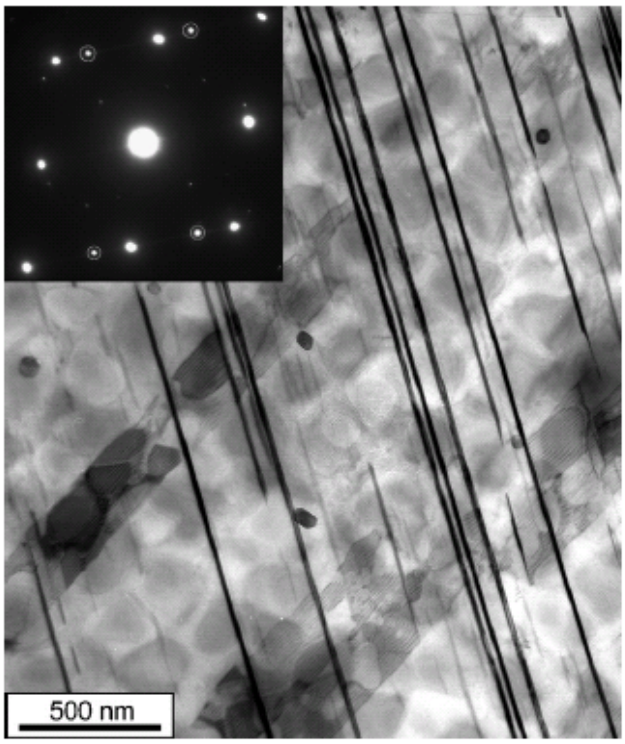

Figure 4.2 Microtwinning deformation in René 104 sample crept at 690 MPa and 677ºC (Unocic et al., 2008).

The planar faults were examined further with high resolution TEM (HRTEM), and they were identified as twins with a thickness of 4 to 50 atomic planes, thus referred to as "microtwins" (Kovarik et al., 2009a). A HRTEM image of a microtwin observed in a test specimen of René 88 DT is displayed in Figure 4.3.

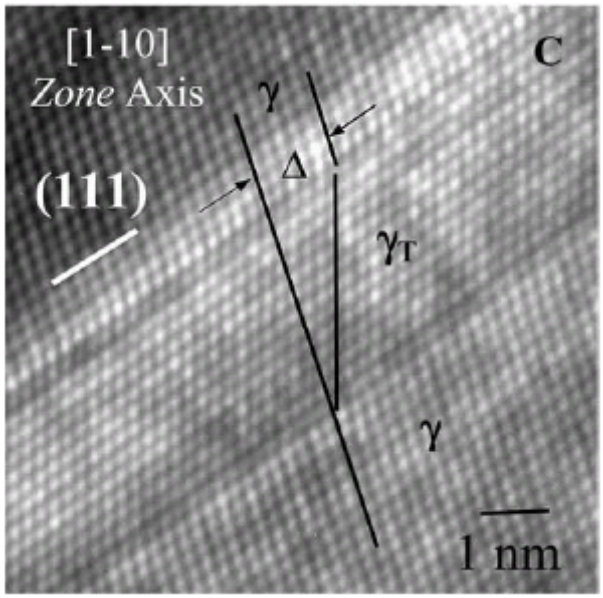

Figure 4.3 HRTEM of René 88 DT specimen after creep load showing a microtwin (Viswanathan et al., 2005).

On the other hand, Ni-base superalloys with larger γ′ precipitates, such as slow cooled (24ºC/min) René 88 DT, demonstrated a quite different mechanism (Viswanathan et al., 2005). Stacking faults were observed to dominate the deformation process, but the faults were limited only to the secondary γ′ precipitates, therefore referred to as isolated faults. Many of the faulted secondary precipitates were also looped by Shockley partial dislocation while the γ matrix was deformed by $a/2\langle 110\rangle$ type dislocations. In the case of René 104 specimens with the coarser γ′ microstructure, the γ matrix was also deformed

by a/2$\langle 110 \rangle$ type dislocations, but in the secondary γ′ precipitates, SISFs were observed instead, which also sheared the γ matrix (Unocic et al., 2008). The tertiary γ′ precipitates scattered in the γ matrix were sheared by a/2$\langle 110 \rangle$ type dislocations and created anti-phase boundaries (APB) in both René 88 DT and René 104 (Unocic et al., 2008; Viswanathan et al., 2005).

In René 88 DT specimens crept under a high stress (972 MPa); microtwinning and Shockley partials were not observed. Instead, a/2$\langle 110 \rangle$ type full dislocations sheared the γ matrix, and the secondary γ′ precipitates were looped around by dislocations of the same type (Orowan looping). Analysis also showed some hints of the transitioning process of the deformation mechanism from isolated faulting to APB shearing (Viswanathan et al., 2005).

4.2.2 Reordering Process

Analyzing observed deformation mechanisms helps to logically map the observed phenomena and establish an effective deformation mechanism model. Development of a deformation model that can concurrently explain multiple deformation mechanisms occurring in a wide range of conditions is still in very early stages. There have been several deformation mechanism models introduced based on the observed microtwins in single crystal superalloys such as SRR99 (Ardakani et al., 1999), CMSX-4 (Knowles and Chen, 2003) and NIMONIC 105 and PE6 (Kolbe, 2001). However, the microtwinning induced deformation in polycrystal disk alloys is still a relatively new concept as creep deformation is not considered as crucial in disk alloy applications as in turbine blades.

Among the microtwin models of single crystal superalloys, Kolbe confirmed that the microtwins were created after Shockley partial dislocations sheared both the γ matrix and γ′ precipitates. Kolbe suggested a diffusion-mediated atomic reordering concept in which the temperature dependent diffusional process can transform stacks of complex stacking faults (CSFs) into true microtwins. The concept still remains as a theoretical model, lacking full validation. However, a few connections can be made from the analyses based on experimental tests, and the theoretical model can feasibly be applied at higher length scales.

It has been already confirmed by TEMs and contrast analyses that the series of Shockley dislocations shear both the matrix and the γ′ precipitates when microtwinning is the dominant deformation mechanisms in Ni-base superalloys (Viswanathan et al., 2005; Viswanathan et al., 2006; Unocic et al., 2008). When a wake of Shockley partials encounters γ′ precipitates, Al-Al nearest neighbor violations occur and energetically less favored CSFs are created, which is also confirmed using HRTEM (Sarosi et al., 2006). As the CSFs are created, pseudotwins are formed in the γ′ precipitates, and the structure changes from Ll_2 to orthorhombic (Karthikeyan et al., 2006). Kolbe (2001) suggested that the pseudotwins transform into true microtwins and the initial Ll_2 structure is restored by a series of diffusion steps, as described in Figure 4.4.

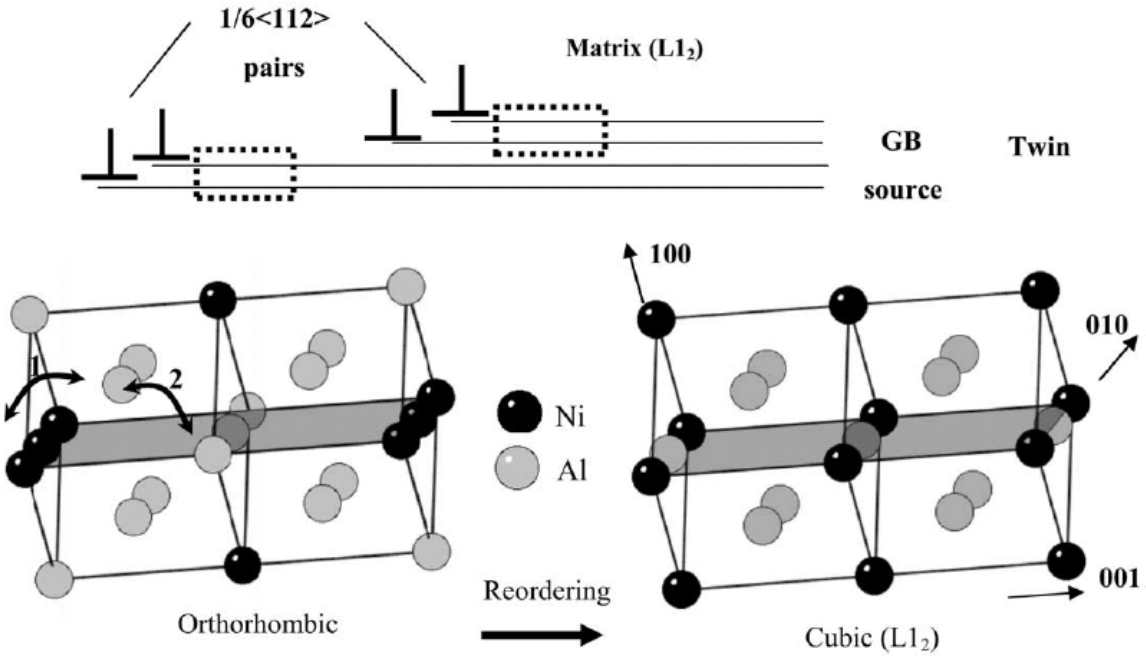

Figure 4.4 Microtwinning mechanism and reordering process (Viswanathan et al. 2005).

Since the diffusion process is strongly temperature dependent, the suggested reordering process is also thermally activated. This explains why the microtwinning is only observed at intermediate temperatures (Karthikeyan et al., 2006). Furthermore, when the applied stress is high enough to provide additional deformation energy athermally, other mechanisms, such as Orowan looping or APB shearing, are preferred over thermally activated microtwinning. Therefore, it can be construed that dislocation dissociation and microtwinning occur only at moderate stress levels and at intermediate temperatures.

According to HRTEM images, thicker microtwins tend to form more of the lower energy Ll_2 structure, while thinner ones consist of the high energy multi-layered CSF structure (Viswanathan et. al, 2006). Also, as thicker microtwins are observed more in highly crept specimens, it can be presumed that the microtwinning process is not a static

phenomenon but a transient process that converts high energy pseudotwins to true twins by a diffusion-mediated process such as reordering (Viswanathan et al., 2006).

4.2.3 Recent Findings and Partial Verification

There have been multiple approaches to understanding the connections among observed configurations and the structure of deformation mechanisms in Ni-base superalloys based on detailed analyses on microtwins. Recently, Unocic et al. (2008) attempted to find a detailed relation between the microstructure and the deformation mechanism. As observed in the previously discussed experiments, the coarse γ′ microstructure materials are deformed by full a/2$\langle 110 \rangle$ type dislocations. According to Unocic et al. (2008), in the coarse γ′ microstructure, the spacing between secondary γ′ precipitates is wide enough for the full dislocations to pass between the γ′ precipitates. In turn, the presence of small tertiary γ′ precipitates in the γ matrix slows down the dislocation movement and leaves APBs in the tertiary γ′ precipitates. Therefore, an increase in the volume fraction of tertiary γ′ precipitates enhances the material strength. However, generating APBs requires high activation energy, and creating APBs over an increasing population of the tertiary γ′ precipitates becomes energetically unfavorable above certain volume fraction of the tertiary γ′. Instead, dissociation of dislocation starts to occur and APBs in the tertiary γ′ particles are replaced by low energy SESFs. Since high energy APBs are created only in the tertiary γ′ particles, whereas low energy SESFs are formed in both tertiary γ′ particles and γ matrix, there is a transition point at which one becomes energetically favorable over the other, as depicted in Figure. 4.5.

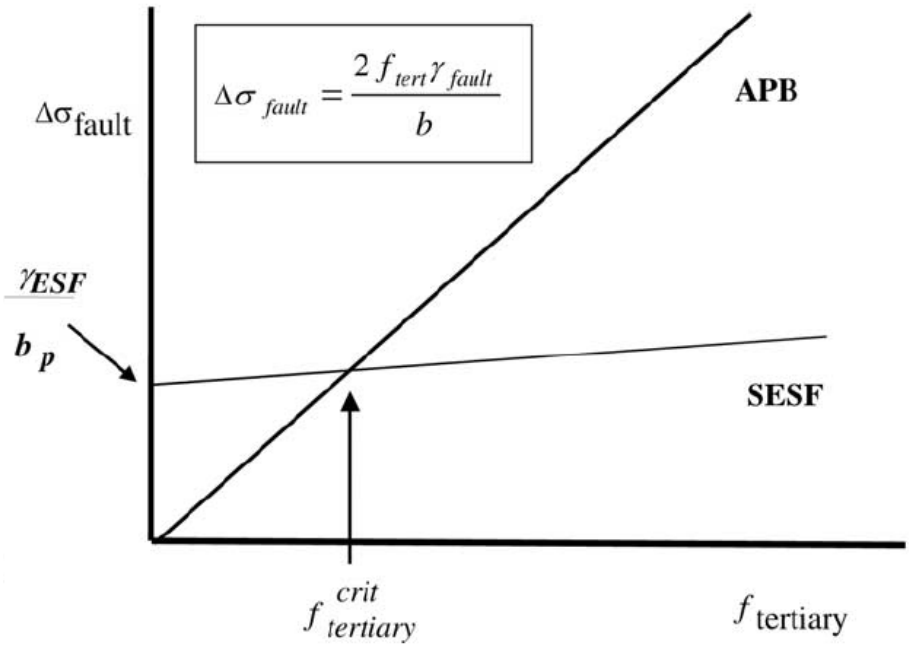

Figure 4.5 Schematic plot of the tertiary γ′ precipitate shearing mechanism determination based on the tertiary γ′ volume fraction (Viswanathan et al., 2005).

Additionally, tertiary γ′ precipitates are observed to cluster and start to increase in size and decrease in volume over extended time under creep loads at intermediate temperatures; this is known as a microstructural coarsening effect (Viswanathan et al., 2005). The microstructural coarsening occurs during creep deformation, and small tertiary γ′ particles grow while the applied load is maintained. If the microstructural coarsening becomes significant enough to decrease the tertiary γ′ volume fraction to reach the critical tertiary γ′ volume fraction, low energy SESFs start to replace APBs and dislocation dissociations take place. Afterwards, the deformation can gradually transit from microtwinning to isolated faulting or Orowan looping as observed experimentally (Viswanathan et al., 2005). Such observations suggest that a constitutive model for these types of applications should be capable of reflecting variations of microstructure attributes.

On the other hand, if the γ′ precipitates are relatively small and the spacing between the secondary γ′ precipitates is too narrow to allow the a/2$\langle 110 \rangle$ type dislocations to pass, dislocations are dissociated and a/6 $\langle 112 \rangle$ Shockley partials are generated, which consequently creates microtwins by a reordering process (Unocic et al., 2008).

According to Kolbe (2001), microtwins experience transformations from pseudotwins to true twins, and the initial Ll_2 structure is restored by a diffusion-mediated reordering process. Based on diffraction pattern analysis, it is confirmed that observed microtwins are indeed restored to Ll_2 structures, which provides another point supporting Kolbe's reordering hypothesis (Sarosi et al., 2006).

Additionally, in the work of Kovarik et al. (2009a; 2009b), high-angle annular dark field (HAADF) images were used for analyzing microtwins comprehensively. The HAADF scanning TEM images reveal the changes in the thickness of microtwins and the separations between Shockley partials (two to six planes apart), which indicates that the energy drop relative to the total energy in the thickness changing section is significant. The large relative energy drop is interpreted to be caused by conversion of pseudotwins to true twins by a reordering process. The HAADF images also confirm that the operative dislocations of both microtwins are a/6$\langle 112 \rangle$

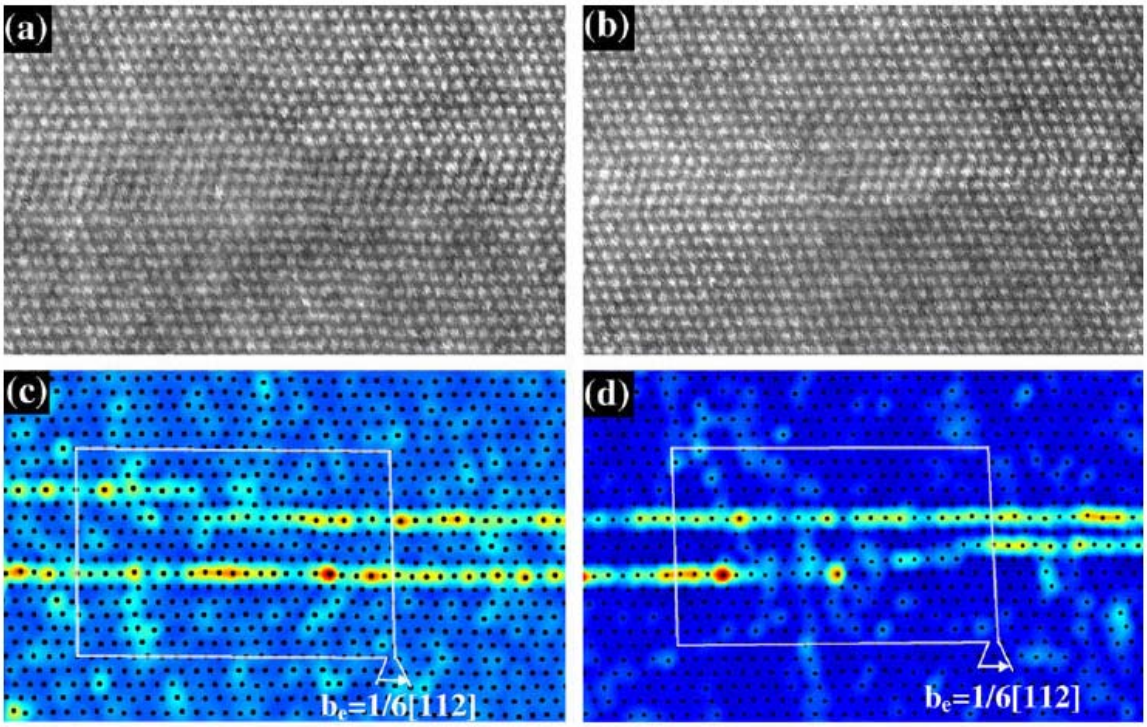

Figure 4.6 (a) HAADF image showing a/6<112> Shockley partials at the microtwin interface and changing the thickness from 4 to 6 layers. (b) HAADF image showing the microtwins changing the thickness from 2 to 4 layers. (c and d) RGB color coded HAADF images blue being the perfect crystal and warmer colors representing deviation from a perfect crystal (Kovarik et al., 2009b).

4.3 Phase Field Model

To study the dislocation dissociation and interactions with γ′ precipitates in Ni-base superalloys, the microscopic phase field (MPF) model was developed previously (Shen et al., 2003). The phase field model of a dislocation employs γ-surface data which reveals the dislocation structure and relates field variables to the crystalline energy so that various planar defects are quantitatively characterized and dislocation configurations are predicted (Shen et al., 2003). The MPF model can reflect arbitrary configurations of dislocation geometries and microstructures based on shear type inelastic strain fields and

the voxel-to-voxel elastic interaction kernel, which can identify characteristics of the dislocation dissociation process (Kovarik et al., 2009b).

Recently, an MPF model has been developed to simulate a a/2$\langle 110 \rangle$ dislocation dissociated into Shockley partials (Kovarik et al., 2009b). The simulation has been conducted on a single screw dislocation interacting with 300nm diameter γ′ particles spread at 75nm apart. The resolved shear stress is applied in the direction parallel to the leading partial dislocation, which promotes the dislocation dissociation to the greatest degree, i.e., the force acting on the leading partial is twice that acting on the trailing partial. The MPF model is applied to three different cases: (1) without tertiary γ′ particles, (2) with tertiary γ′ particles, and (3) with tertiary γ′ particles and higher ISF energy. As shown in Figure 4.7(a), the favorably loaded leading partial dissociates from the full dislocation and proceeds to the matrix channel while the trailing partial remains. Between the two partials, a wide ISF band is created. On the other hand, if tertiary γ′ particles are considered in the matrix, the dissociated leading partial dislocation has to generate CSFs on the tertiary γ′ particles, which significantly hinders the migration of the leading partial dislocation. In addition, the tertiary γ′ particles provide an extra impediment on the motion of the a/2$\langle 110 \rangle$ full and Shockley trailing dislocations for creating APBs on the tertiary γ′ particles in the matrix. This leaves less energy for creating ISFs between the leading and trailing partials, thus the gap between the partial becomes much narrower as the volume fraction of tertiary γ′ particles is increased. When simulated with an increased ISF energy from 10 mJ/m^2 to 100 mJ/m^2, the a/2$\langle 110 \rangle$ dislocation is immobilized at the particle without advancing any further. In addition, the dislocation dissociation does not occur as there is not enough energy to generate ISFs.

Also, if the applied shear stress is raised enough to bypass the secondary γ′ particles via Orowan bowing, dislocations are not dissociated; hence microtwinning will not occur. It is also suggested that the orientation of the applied shear stress with respect to the operative Burgers vector is a critical factor, as dissociation will only occur when the stress is loaded in the direction favorable to the leading partial, and microtwinning will occur only if dislocations can be dissociated (Kovarik et al., 2009b). In summary, dislocation dissociation, a precursor of microtwinning, occurs only when the loading direction is favorably oriented to the leading partial dislocation direction. In these circumstances, the stress resolved in that direction has to be high enough to create ISFs in the γ matrix and APBs and CSFs on tertiary γ′ particles, but it must not be so high as to bypass the secondary γ′ particles. Based on the analysis of results of simple MPF simulations, the MPF models can provide valuable information to understand the mechanism of microtwinning, which in turn can contribute to the predictive character of the constitutive model.

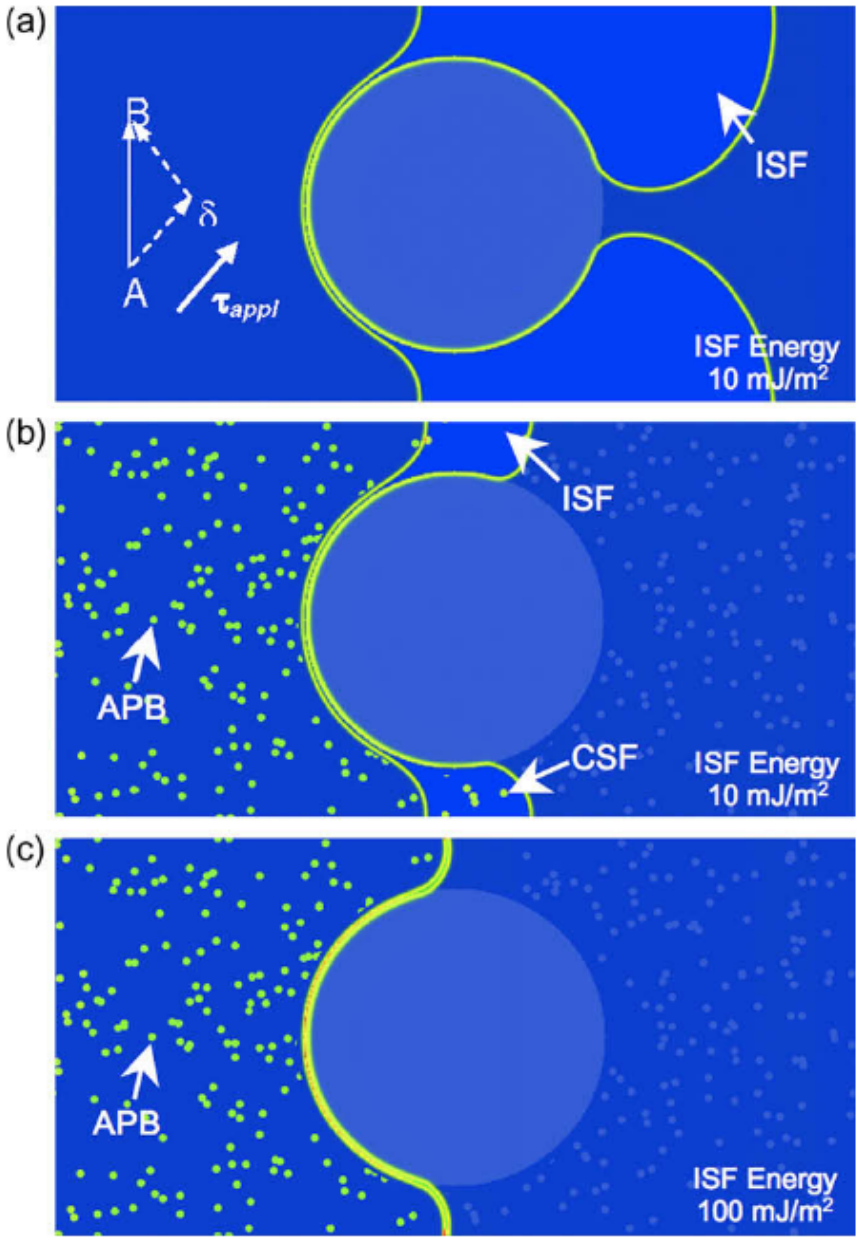

Figure 4.7 MPF model simulation of full dislocation movement interacting with secondary γ′ particles (a) without tertiary γ′, (b) with tertiary γ′ and (c) with an increased ISF energy and tertiary γ′ (Kovarik et al., 2009b).

4.4 Directional Dependence Study of the MPF Model Simulations (MAI program)

Starting in 2008, The Air Force Research Laboratory launched the Durable High-Temperature Disk Material program to develop a durable high temperature disk alloy.

Within the program, Y. Wang of the Ohio State University conducted MPF simulations of the dissociation of a screw dislocation with the maximum resolved shear stress magnitude and its applied direction being varied. The simulations were conducted in 2D with only uniaxial loadings considered. In order to physically associate the limited simulation conditions with 3D models, the 2D plane on which the simulations take place can be considered as a slip plane of a 3D model. Therefore, the shear stress applied in the MPF model can be considered as the resolved shear stress acting on a slip plane.

The MPF simulation results showed that the maximum resolved shear stress magnitudes required to dissociate dislocations into Shockley partial dislocations on the {111} slip plane(s) or to pass dislocations through the γ' precipitate were dependent on the loading direction respect to the slip direction (unpublished communication, MAI program, 2009). Based on their work, the upper and lower bounds of the resolved shear stress magnitudes required for dislocations to dissociate can be formulated as a function of the maximum resolved shear stress orientation. The upper bound is set on the maximum resolved shear stress magnitudes that allow a/2 $\langle 110 \rangle$ type dislocations to dissociate without bypassing γ' particles (referred to as the upper dissociation threshold hereafter). The lower bound is the minimum magnitude of the maximum resolved shear stress needed for the a/6 $\langle 112 \rangle$ type leading partial dislocation to be dissociated from a full a/2 $\langle 110 \rangle$ type dislocation (lower dissociation threshold) as a function of the maximum resolved shear stress direction. In other words, if the maximum resolved shear stress is less than the lower dissociation threshold, decorrelation of a dislocation cannot occur, and the full dislocation movement will be immobilized at γ' particles.

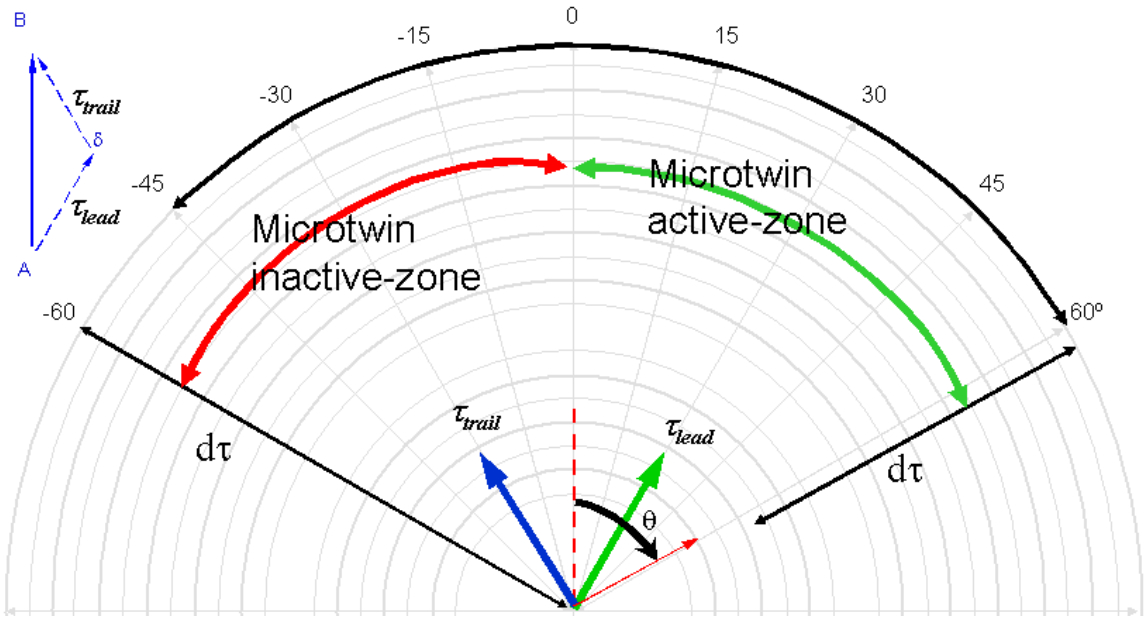

Figure 4.8 Angular convention of dislocation dissociation and microtwin active/inactive zones defined by phase field model simulations.

A couple of important aspects are noteworthy based on the analysis of MPF model results. First, dislocations do not dissociate when the maximum resolved shear stress is acting in the direction favorable to the trailing partial dislocation (–60°~0° in Figure 4.8), regardless of the magnitude of the resolved shear stress. They are either pinned at the entrance of the matrix channel (i.e., stress magnitude is not high enough to transmit dislocations), or they are transmitted as full dislocations with no dissociation involved. This implies that the lower and upper dissociation thresholds collapse when the dislocations are loaded favorably to the trailing partials, and dislocations do not dissociate.

In Figure 4.8, angle 0° is set in the a/2$\langle 110 \rangle$ type full Burgers vector; the region to the right where the leading partial dislocation is oriented, is the dislocation dissociation possible zone (i.e., θ=0 to 60° covered in a green two-sided arrow). On the other hand,

the region on the left side (θ=0 to –60° in Figure 4.8) can be defined as the dislocation dissociation free zone (i.e., favorable to the trailing partial dislocation). The focus of this study is placed in the dislocation dissociation possible zone where the microtwinning dominated deformation can be expected.

From the angular study based on MPF simulation results, it can be concluded that the resolved shear stress required to initiate dislocation dissociation is minimum at the angle θ=30° (i.e., in the direction of the leading partial dislocation). Additionally, the magnitudes of the resolved shear stress required to spread the leading partial dislocation from the trailing partial dislocation, increase as the orientation of the maximum resolved shear stress on the slip plane deviates from the leading partial dislocation direction, as shown as threshold stress in blue in Figure 4.9.

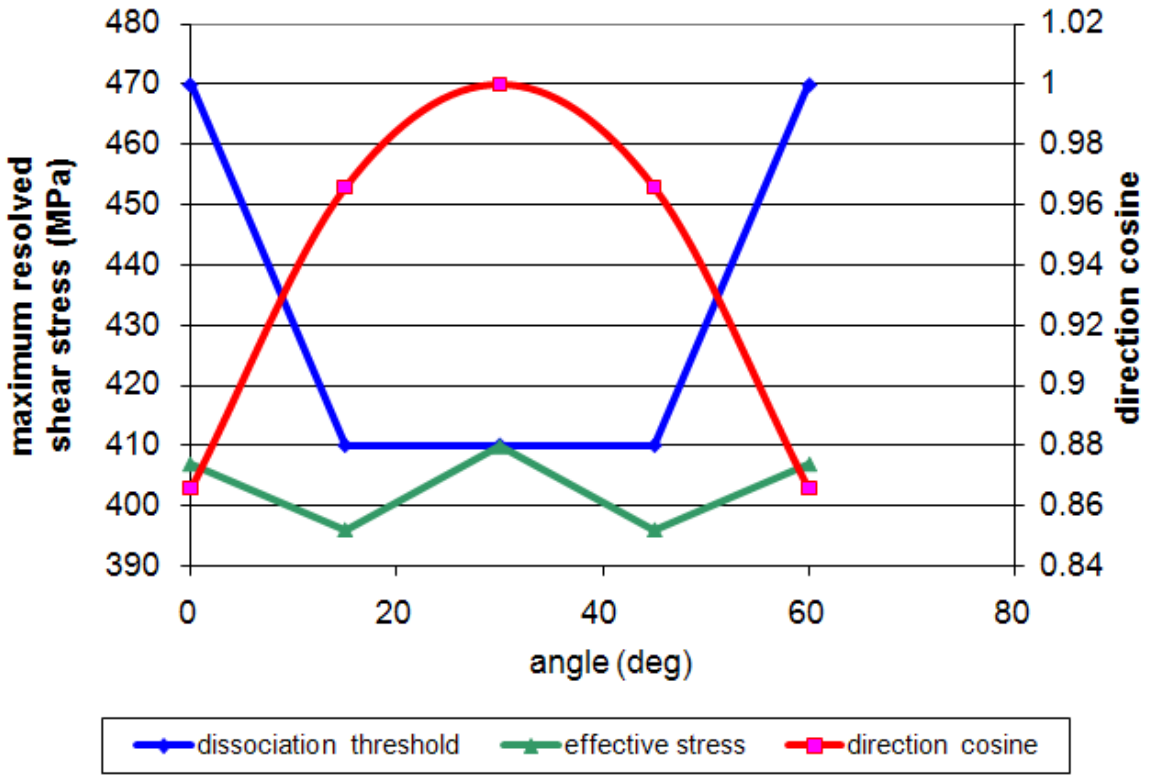

Figure 4.9 Angular dependence of lower dissociation threshold shear stress, directional factor (direction cosine) and the resolved shear stress acting on the leading partial direction based on MPF results at OSU.

The minimum resolved shear stress required for dissociation in the angular domain of the dissociation possible zone is plotted in blue in Figure 4.9. The lower dissociation threshold stress is measured to be constant between 15 and 45°, but it increases rapidly outside the angular range, which indicates that the stress required to initiate the dissociation of dislocation grows as the resolved shear stress direction deviates from the leading partial direction. With the angles formed between the direction of the maximum resolved shear stress and the Shockley partial dislocations, it is possible to use the dot product of the two: (1) the unit vector in the direction of the maximum resolved shear stress and (2) a unit vector in the direction of the Burgers vector of the leading partial

dislocation, in order to calculate a scalar projection of one onto the other. This scalar value is the direction cosine of angle θ, with its peak reaching at 1 when θ =30° and symmetrically diminishing to 0.866 as the resolved shear stress direction deviates from θ =30° to θ = 0° or 60°. This direction cosine is depicted with a red curve in Figure 4.9.

Additionally, when the dissociation threshold stress and the directional factor are multiplied, the product can be considered as the resolved stress acting on the leading partial dislocation at the verge of dissociation; the resulting plot is shown as green in Figure 4.9. Even though the calculated resolved shear stress shows some fluctuation, the deviation is within 5%.Since the threshold shear stress values were obtained from the MPF chart with limited resolution, one can say that the threshold stresses resolved in the leading partial dislocation directions are fairly consistent. Hence, it is reasonable to assume that the variations in lower microtwinning threshold stress are caused by the orientation of the maximum resolved shear stress relative to the direction of the leading partial dislocation.

In summary, the MPF results suggest the following: First, concerning the lower threshold stress of the dislocation dissociation, the magnitude of the resolved shear stress acting on the leading partial dislocation triggers the dissociation of dislocation, which in turn initiates the evolution of the microtwinning process. Second, the difference between the resolved shear stress acting on the leading and trailing partial dislocations can be related to the separation between the two partials, hence to the growth of the microtwin. This difference increases as the direction of the maximum resolved shear stress is oriented away from the trailing partial dislocation, which provides an extremely low driving force to recombine the two partials.

4.5 Implementation of Microtwinning in the Crystal Plasticity Model

The observed configurations of the microtwinning process at the length scales of the microstructure can be implemented in the crystal plasticity model in an average sense at the length scale of a grain. Even though the microtwinning deformation mechanism and its process are not fully understood in terms of influence on the macroscopic response, the observations are still worth implementing in the crystal plasticity model. The crystal plasticity model then links the microtwinning deformation configuration to the macroscopic response while retaining the representation of dislocation mechanisms at higher stress levels; in this way the model establishes a hierarchy of models linking the diffusion-mediated reordering process to the MPF model and to the crystal plasticity model.

4.6 Crystal Plasticity Framework

The crystal plasticity constitutive model implemented in this research assumes a homogenous representative volume element (RVE) without γ' precipitates and γ matrix being explicitly modeled at the length scale of a grain. The averaged response is calculated with microstructure-sensitivity being implicitly embedded. A two-term flow rule is used to model the rate-dependent response. The grain size and crystallographic orientation are explicitly implemented in the model, with the dislocation substructure implicitly addressed.

The γ/γ′ phase Ni-base superalloy considered in this work is assumed to have a total of 18 slip systems at any given crystal orientation angle: 12 octahedral and 6 cube slip systems, all of which are assumed to be active above the threshold stress.

The model presented in this section closely related to the work of Shenoy (2006) and is later explained in further detail and accuracy by Przybyla and McDowell (2010). The modifications to the model are mainly introduced to accommodate recently observed phenomena of disk alloys such as microtwinning and highlight relaxation.

4.6.1 Kinematics

The continuum crystal plasticity is based on the multiplicative decomposition of the deformation gradient into plastic and elastic portions. The deformation gradient **F** is given by

$$\mathbf{F} = \frac{d\mathbf{x}}{d\mathbf{X}} \tag{4.1}$$

where **x** and **X** are the coordinates of the current and reference configurations, respectively. The deformation is assumed to occur in two distinct steps (Asaro, 1983). The plastic deformation gradient, $\mathbf{F}^p$, captures plastic deformation by the dislocation motion while the orientation and crystal lattice spacing are unchanged. The elastic deformation follows and describes the lattice structure distortion. The elastic deformation also embeds an arbitrary rigid body rotation, denoted as $\mathbf{F}^e$.

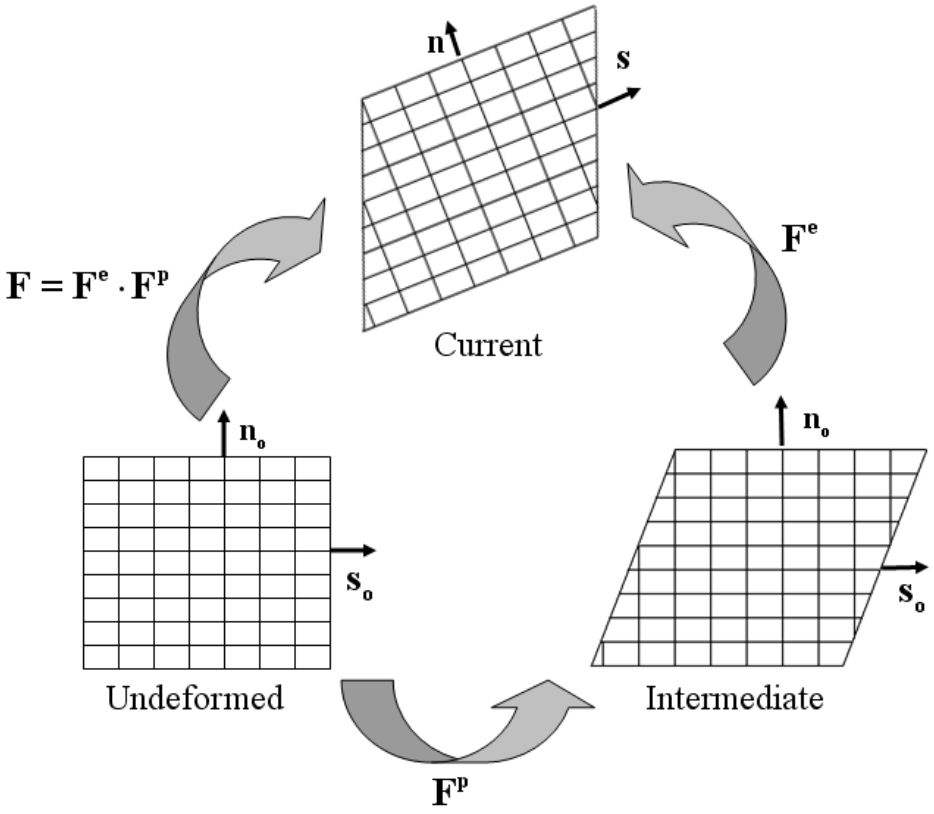

Figure 4.10 Kinematics of elastic-plastic single crystal deformation in undeformed, intermediate and current configurations.

The slip direction $\mathbf{s}_0$ and the unit normal vector to the slip plane $\mathbf{n}_0$ of the crystal lattice in the reference configuration are deformed to **s** and **n** in the current configuration via elastic lattice distortion and rigid body rotation**,** respectively. The deformation gradient is decomposed into elastic and plastic parts, i.e.,

$$\mathbf{F} = \mathbf{F}^{e} \cdot \mathbf{F}^{p} \tag{4.2}$$

Using the deformation gradient, the velocity gradient **L** in the current configuration is

$$\mathbf{L} = \dot{\mathbf{F}} \cdot \mathbf{F}^{-1} = \dot{\mathbf{F}}^{e} \cdot \left(\mathbf{F}^{e}\right)^{-1} + \mathbf{F}^{e} \cdot \dot{\mathbf{F}}^{p} \cdot \left(\mathbf{F}^{p}\right)^{-1} \cdot \left(\mathbf{F}^{e}\right)^{-1} \tag{4.3}$$

The velocity gradient can be decomposed into the symmetric deformation rate **D** and the anti-symmetric spin tensor **W**, i.e.,

$$\mathbf{L} = \mathbf{D} + \mathbf{W} \tag{4.4}$$

The deformation rate and the spin tensor can be further decomposed into elastic and plastic parts as in the deformation gradient.

$$\mathbf{D} = \mathbf{D}^{e} + \mathbf{D}^{p},\ \mathbf{W} = \mathbf{W}^{e} + \mathbf{W}^{p} \tag{4.5}$$

Since the plastic deformation is assumed to be driven by the dislocation motion, the plastic rate of deformation and the spin tensors can be related to the shearing rate $\dot{\gamma}^{\alpha}$ of slip system α (Asaro, 1983), i.e.,

$$\begin{aligned} \mathbf{L}^{p} &= \sum_{\alpha=1}^{n_{slip}} \dot{\gamma}^{\alpha} \left(\mathbf{s}_{o}^{\alpha} \otimes \mathbf{m}_{o}^{\alpha} \right) = \dot{\mathbf{F}}^{p} \cdot \left(\mathbf{F}^{p} \right)^{-1} = \mathbf{D}^{p} + \mathbf{W}^{p} \\ \mathbf{D}^{p} &= \frac{1}{2}\left(\mathbf{L}^{p} + \mathbf{L}^{pT} \right),\ \mathbf{W}^{p} = \frac{1}{2}\left(\mathbf{L}^{p} - \mathbf{L}^{pT} \right) \end{aligned} \tag{4.6}$$

where α denotes the slip system of interest. The plastic deformation rate and the shearing rate can be used in the numerical integration of the crystal plasticity constitutive relation.

4.6.2 Stress

The kinematic relations of crystalline slip systems can be related to the kinetics of deformation such that slip system shearing rates are written in terms of the resolved shear stress on slip systems. The elastic part of the deformation gradient is given by

$$\mathbf{F}^{e} = \mathbf{F} \cdot \left(\mathbf{F}^{p} \right)^{-1} \tag{4.7}$$

The elastic Green strain is defined as

$$\mathbf{E}^{e} = \frac{1}{2}\left[\mathbf{F}^{eT} \cdot \mathbf{F}^{e} - \mathbf{I} \right] \tag{4.8}$$

where $\mathbf{I}$ is the identity matrix. The elastic Green strain is related to the 2nd Piola-Kirchhoff stress tensor in the intermediate configuration by

$$\boldsymbol{\sigma}^{pk2} = \mathbf{C} : \mathbf{E}^{e} \tag{4.9}$$

where $\mathbf{C}$ is the 4th rank elastic stiffness tensor, and $\boldsymbol{\sigma}^{pk2}$ is the 2nd Piola-Kirchhoff stress. The 2nd Piola-Kirchhoff stress is then converted to the Cauchy stress in the current configuration, i.e.,

$$\boldsymbol{\sigma} = \frac{1}{\det\left(\mathbf{F}^{e}\right)} \mathbf{F}^{e} \cdot \boldsymbol{\sigma}^{pk2} \cdot \mathbf{F}^{eT} \tag{4.10}$$

The resolved shear stress on slip system α is given by

$$\boldsymbol{\tau}^{\alpha} = \left(\mathbf{F}^{eT} \cdot \mathbf{F}^{e} \cdot \boldsymbol{\sigma}^{pk2}\right) : (\mathbf{s}_{o}{}^{\alpha} \otimes \mathbf{m}_{o}{}^{\alpha}) \tag{4.11}$$

Assuming $\mathbf{F}^{eT} \cdot \mathbf{F}^{e} \cong 1$ as the elastic deformation in high strength material is infinitesimal, the resolved shear stress can be simplified, i.e.,

$$\boldsymbol{\tau}^{\alpha} \cong \boldsymbol{\sigma}^{pk2} : (\mathbf{s}_{o}{}^{\alpha} \otimes \mathbf{m}_{o}{}^{\alpha}) \tag{4.12}$$

The resolved shear stress can be used in the flow rule to calculate the shearing rate on αth slip system which will be discussed further in the following sections.

4.6.3. Flow Rule

The flow rule specifies the inelastic shearing rate on the αth slip system using the resolved shear stress and the ISV evolution. The flow rule used in this crystal plasticity model is comprised of two terms: (1) the slip system shearing rate term describing collective deformation by dislocation glide on octahedral and cube slip systems, and (2) the microtwin shearing rate representing the deformation by microtwinning on octahedral slip systems. Therefore, the shearing rates for cube slip systems are solely determined by the first term. The shearing rate on the αth slip system is given by

$$\dot{\gamma}_{oct}^{\alpha} = \left[\dot{\gamma}_1 \exp\left(-\frac{Q_1}{k_B T} \right) \left\langle \frac{\left| \tau^{\alpha} - \chi^{\alpha} \right| - \kappa^{\alpha}}{D^{\alpha}} \right\rangle^{n} \right] \operatorname{sgn}\left(\tau^{\alpha} - \chi^{\alpha} \right) + \dot{\gamma}_{mt}^{\alpha} \tag{4.13}$$

where τ^{α} is the resolved shear stress, κ^{α} is the threshold slip resistance stress, χ^{α} is the back stress, and D^{α} is the drag stress on the α^{th} slip system. Also, k_B is the Boltzmann's constant, T is temperature in K, and Q_1 is the activation energy for dislocation obstacle bypass. The McCauley bracket $\langle\ \rangle$ returns zero when the value inside the bracket is negative, defining the regime of elastic deformation.

The microtwin-induced shearing rate, formulated to capture the deformation by microtwinning, is calculated using the Orowan equation following the model introduced by Karthikeyan et al. (2006), i.e.,

$$\dot{\gamma}_{mt}^{\alpha} = b_{tp} v^{\alpha} \rho_{mt}^{\alpha} \tag{4.14}$$

where b_{tp} is the Burgers vector for the twinning partial dislocation, v^{α} is the velocity of the microtwin, and ρ_{mt}^{α} is the microtwin density. The microtwinning shearing rate is formulated so that it is dominant only at low stress levels at which the microtwinning is a viable deformation mechanism. Detailed descriptions of state variables and their evolution equations are discussed in the following sections.

4.6.4 Threshold Slip Resistance

The threshold slip resistance is analogous to the yield stress in macroscopic response. Therefore, if the resolved shear stress exceeds the threshold slip resistance, dislocations start to glide. The threshold slip resistance depends on the microstructure attributes and captures hardening behavior induced by dislocation interactions. Shenoy expressed slip resistance by combining two terms: the initial reference critical resolved shear stress

(CRSS) and the Taylor hardening term (2006). It should be noted that Shenoy's slip resistance formulation (2006) was recently updated for accuracy of presentation by Przybyla and McDowell (2010). The initial CRSS is microstructure-sensitive and is determined for octahedral and cube slip systems by

$$\kappa_{o,oct}^{\alpha}=\left[\tau_{o,oct}^{\alpha}+c_{p1}\sqrt{\xi\frac{f_{p1}^{'}}{d_1}}+c_{p2}\sqrt{\xi\frac{f_{p2}^{'}}{d_2}}+c_{p3}\sqrt{\xi f_{p3}^{'}d_3}+\frac{c_{gr}}{\sqrt{d_{gr}}}\right]+\left(f_{p1}+f_{p2}\right)\tau_{ns}^{\alpha}$$

$$\kappa_{o,cub}^{\alpha}=\left[\tau_{o,cub}^{\alpha}+c_{p1}\sqrt{\xi\frac{f_{p1}^{'}}{d_1}}+c_{p2}\sqrt{\xi\frac{f_{p2}^{'}}{d_2}}+c_{p3}\sqrt{\xi f_{p3}^{'}d_3}+\frac{c_{gr}}{\sqrt{d_{gr}}}\right] \qquad (4.15)$$

$$\text{where, } \xi=\frac{\Gamma_{APB}}{\Gamma_{APB\_ref}}$$

Here, $f_{p1}^{'}$, $f_{p2}^{'}$ and $f_{p3}^{'}$ are normalized primary, secondary and tertiary γ′ precipitate volume fractions, respectively. The γ′ precipitate and grain sizes are respectively incorporated as d_1, d_2, d_3, and d_{gr}, while c_{p1}, c_{p2}, c_{p3} and c_{gr} are fitting parameters for strength due to the corresponding γ′ particles and grain sizes. The microstructure attributes significantly affect the initial CRSS and control the macroscopic mechanical response.

The stress τ_{ns}^{α}, applicable only to the octahedral slip systems, captures the non-Schmid effect, caused by the transformation from the glissile to sessile core dissociation by implementing the Paidar-Pope-Vitek (PPV) model. The non-Schmid stress is defined as (Sheh and Stouffer, 1990)

$$\tau_{ns}^{\alpha}=h_{pe}\tau_{pe}^{\alpha}+h_{se}\tau_{se}^{\alpha}+h_{cb}\left|\tau_{cb}^{\alpha}\right| \qquad (4.16)$$

where τ_{pe}^{α}, τ_{se}^{α}, τ_{cb}^{α} are the resolved shear stresses on the primary, secondary and cube slip systems, and h_{pe}, h_{se}, h_{cb} are corresponding temperature dependent material constants. According to the PPV model (Paidar et al., 1984), screw dislocations on (111) planes can

be dissociated into two super-Shockley partials by APB bands. The configurations of the screw dislocations can be divided into two: (1) the glissile with its core in the same plane and (2) the sessile with a non-planar core in the $(1\bar{1}1)$ plane which increases the threshold slip resistance.

The shear stresses on the primary and the cube slip systems of Eq. (4.16) reflect the cross-slip mechanism and capture the tension/compression asymmetry. The sign of the shear stress on the primary slip system, τ_{pe}^{α}, determines whether the constriction or separation of the Shockley partial dislocations will occur; this in turn determines the possibility of the cross-slip from the octahedral plane to the cube plane. The magnitude of the resolved shear stress on the cube slip system, τ_{cb}^{α}, on the other hand, determines whether the cross slip will occur; this is independent of the direction of the resolved shear stress. As suggested in the PPV model, the shear stress on the secondary slip system, τ_{se}^{α}, is included in the model.

The initial CRSS and Taylor hardening terms are combined, and the overall slip resistance for octahedral and cube slip systems can be written as

$$\kappa_{\lambda}^{\alpha}=\kappa_{o,\lambda}^{\alpha}+\alpha\tilde{\mu}\tilde{b}\sqrt{\rho_{\lambda}^{\alpha}} \tag{4.17}$$

where α is a statistical coefficient with a strong dependence on the volume fraction of the primary γ' precipitates, and ρ^{α} is the dislocation density of a slip system which will be discussed further in the following section. Additionally, $\tilde{\mu}$ and $\tilde{b}$ are the volume fraction averaged shear modulus and the Burgers vector, respectively, i.e.,

$$\begin{aligned}\tilde{\mu} &= \left(f_{p1}+f_{p2}+f_{p3}\right)\mu_{\gamma'}+f_{m}\mu_{m}\\ \tilde{b} &= \left(f_{p1}+f_{p2}+f_{p3}\right)b_{\gamma'}+f_{m}b_{m}\end{aligned} \tag{4.18}$$

where $\mu_{\gamma'}$ and μ_{γ} are the shear moduli of γ' precipitate and γ matrix phases, and $b_{\gamma'}$ and b_{γ} are the magnitudes of the Burgers vectors for γ' precipitate and γ matrix phases, respectively.

4.6.5 Dislocation Density

The hardening behavior of disk alloys can be considered to arise from the competition between storage and annihilation of dislocations under various loading conditions (Estrin and Mecking, 1984). The dislocation density on the α^{th} slip system is formulated as (Shenoy, 2006)

$$\dot{\rho}_{\lambda}^{\alpha}=h_{\lambda}^{\alpha\alpha}\left\{Z_0+k_1\sqrt{\rho_{\lambda}^{\alpha}}-k_2\rho_{\lambda}^{\alpha}\right\}\left|\dot{\gamma}_{\lambda}^{\alpha}\right| \qquad (4.19)$$

where (i.e., $h_{oct}^{\alpha\alpha}=4.8$, $h_{cub}^{\alpha\alpha}=2.4$, $h^{\alpha\beta}=0$ for $\alpha=\beta$)

where k_1 and k_2 are constants, and Z_0 is given by

$$Z_0=\frac{k_{\delta}}{\tilde{b}d_{\delta eff}}\ ,\ d_{\delta eff}=\left(\frac{1}{d_{1\delta}}+\frac{1}{d_{2\delta}}\right)^{-1} \qquad (4.20)$$

Here, k_{δ} is a constant, and $d_{2\delta}$ is the spacing between secondary γ′ precipitates which can be estimated by the volume fraction and the average particle size. The first term, Z_0, accounts for the effect of restricted activities of dislocations associated with narrow matrix channels between secondary γ' particles. The second term captures the dislocation density growth controlled by the athermal storage of dislocations traveling a distance proportional to the average spacing of dislocations and becoming immobilized when encountered by other dislocations (Estrin and Mecking, 1984; Mecking and Kocks, 1981). The third term $k_2\rho_{\lambda}^{\alpha}$ represents the dynamic recovery which reduces dislocation density by annihilation and rearrangement of accumulated dislocations. The dynamic

recovery term is thermally activated; therefore, k_2 can be temperature and inelastic strain rate dependent (Estrin and Mecking, 1984).

The model is designed to only consider the self-hardening rate with the latent-hardening effect excluded. Also, the effective precipitate spacing, $d_{\delta eff}$, is calculated based only on the secondary γ′ precipitate spacing, as the primary γ′ precipitates do not exist in the supersolvous disk alloys considered in this work.

4.6.6 Back Stress

The kinematic hardening in the crystal plasticity model is also intended to capture the directional effect as in the macroscale ISV model. The back stress in the crystal plasticity model is formulated so that its evolution can be associated with pile-ups of dislocations within matrix channels (McDowell, 2008). The back stress evolution is given by

$$\dot{\chi}_\lambda^\alpha = C_\chi \left\{ \eta \mu_\gamma \tilde{b} \sqrt{\rho_\lambda^\alpha}\, \mathrm{sgn}\left(\tau^\alpha - \chi_\lambda^\alpha\right) - \chi_\lambda^\alpha \right\} \left|\dot{\gamma}^\alpha\right| \tag{4.21}$$

where C_χ is a fitting parameter, and η is also a coefficient which determines the contribution to the flow stress, i.e.,

$$\eta = \frac{\eta_o Z_o}{Z_o + k_1 \sqrt{\rho_\lambda^\alpha}} \tag{4.22}$$

According to Shenoy (2006), η is the geometrically necessary dislocations (GND) partition of the total dislocation density rate which contributes to the back stress evolution, incorporating the γ' precipitate size spacing effect.

4.6.7 Dislocation Dissociation

In the polycrystal plasticity model, as introduced in a previous section, a total of 18 slip systems, 12 octahedral (3 slip directions on 4 slip planes), and 6 cube slip systems (2 slip directions on 3 slip planes) are assumed to be active in the temperature regime of interest (1300°F to 1400°F). Moreover, all slip systems were assumed to be active at relatively higher temperatures. Among 18 slip systems, only 12 octahedral slip systems are considered as possible candidates for embedding microtwins. Furthermore, at a given integration point within a given grain, it is assumed for simplicity that only one slip system can undergo dissociation and generate a microtwin.

The MPF model simulation result analyzed in Section 4.4 is based on only one slip system with its Shockley partial dislocations and corresponding angular relation, which is an oversimplified representation of the dislocation dissociation mechanism as multiple slip systems are present on each octahedral slip plane. On each octahedral slip plane, three slip directions are 120° apart and can act concurrently, as shown in Figure 4.11.

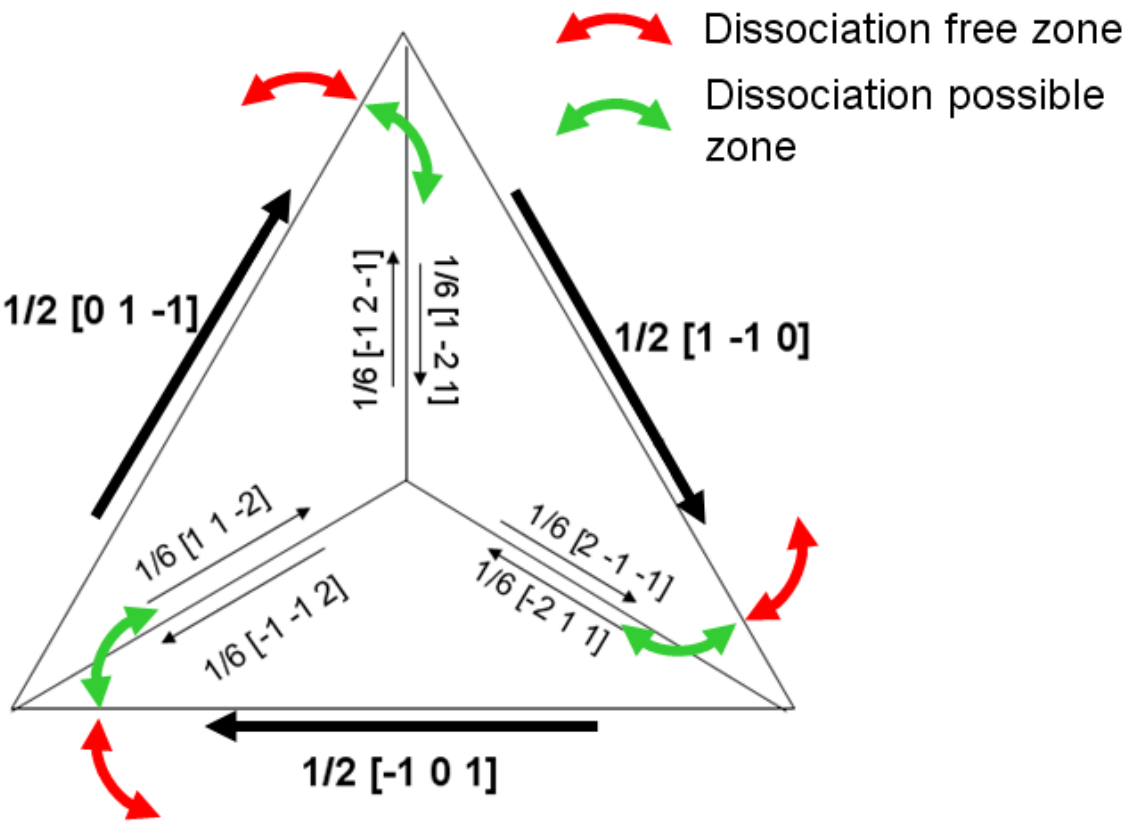

Figure 4.11 Full dislocation slip directions and Shockley leading and trailing partial dislocation Burgers vectors with the dissociation possible/impossible zones on a (111) plane.

The green arrows represent a 60° angular span to the sides of the Burgers vectors of the leading partial dislocations where dissociation into partials is possible, and the red arrows represent a 60° angular span to the sides of the trailing partials where dissociation of a dislocation is not observed. The leading and trailing partial Burgers vectors for octahedral slip systems are listed in Table 4.1.

For an integration point within any grain of the polycrystal Ni-base superalloy, there are four octahedral slip planes as shown in Figure 4.10, each containing three slip directions. Because only one slip system with its leading partial dislocation is most favorably oriented for dissociation, all 12 octahedral slip systems and the associated

Shockley partial dislocation systems have to be tracked to detect the onset of the dissociation. In order for a dislocation to initiate decorrelation on a given slip system, it has to satisfy the following two conditions: (1) the resolved shear stress acting on the slip plane is favorably oriented with respect to the leading partial dislocation of the slip system and (2) the magnitude of the resolved shear stress acting on the leading partial dislocation meets or exceeds the threshold stress for dissociation. Once a slip system meets these two criteria for the dissociation at a given integration point, the corresponding dislocation should initiate to dissociate and nucleate a microtwin; the remaining slip systems should be completely excluded from further consideration of the dislocation dissociation and the microtwin generation. Then, the shearing rate associated with microtwinning can be formulated based on the kinetics of microtwin growth.

In the current polycrystal plasticity scheme, the 2nd Piola-Kirchhoff stress, $\boldsymbol{\sigma}^{pk2}$, in the intermediate configuration is used as the driving force for slip. The traction vector for slip system α acting on a slip plane in the intermediate configuration is given by

$$\mathbf{T}^{\alpha} = \mathbf{n}_{o}^{\alpha} \cdot \boldsymbol{\sigma}^{pk2} \tag{4.23}$$

where $\mathbf{n}_{o}^{\alpha}$ is the unit vector normal to the slip plane containing slip system α. The traction vector can be used to calculate the resolved shear stress acting on either a leading or a trailing partial dislocation for slip system α, i.e.,

$$\tau_{lead/trail}^{\alpha} = \mathbf{T}^{\alpha} \cdot \mathbf{n}_{lead/trail}^{\alpha} \tag{4.24}$$

where $\mathbf{n}_{lead/trail}^{\alpha}$ is a unit vector in the direction of either the leading or trailing partial dislocation, as appropriate. The dissociation condition can be expressed as

$$\max_{\alpha=1,\ldots,12} \left(\tau_{lead}^{\alpha} \right) \geq \kappa_{mt,o} \tag{4.25}$$

where $\kappa_{mt,o}^{\alpha}$ is the lower dissociation threshold stress which is equivalent to the lower microtwinning threshold stress.

Each slip plane contains 3 slip systems, each of which spans 120° of the plane. Therefore, based on phase field model simulations the orientation dependence of dislocation dissociation on a single slip system is insufficient to represent the presence of twelve potentially active slip systems. Instead, the pie chart in Figure 4.11 shows the dislocation dissociation zones on a (111) plane with the full and partial dislocation Burgers vectors. The full Burgers vectors are 120° apart and are denoted in bold. The leading and trailing partials are spread 30° from full Burgers vectors. Again, the regions with green arrows represent the angular domains in which dissociation may occur, while in the regions with red arrows dissociation is inhibited. The boundaries between the dissociation possible and free zones are assumed to coincide with the direction of the full Burgers vectors, based on the MPF results. Figure 4.12 is essentially an extended multi-slip representation of the orientation dependence chart covering all 3 slip systems and 6 partial dislocations on a given octahedral plane, focusing on the lower microtwinning threshold stress as the dissociation criterion. As one may notice, the dissociation possible zones are centered on the leading partial dislocation directions, spanning 30° to each side of the leading partial dislocation. On the other hand, the dissociation free zones center about the orientation of the trailing partial dislocations and represent the conditions for which the dissociation is unfavorable.

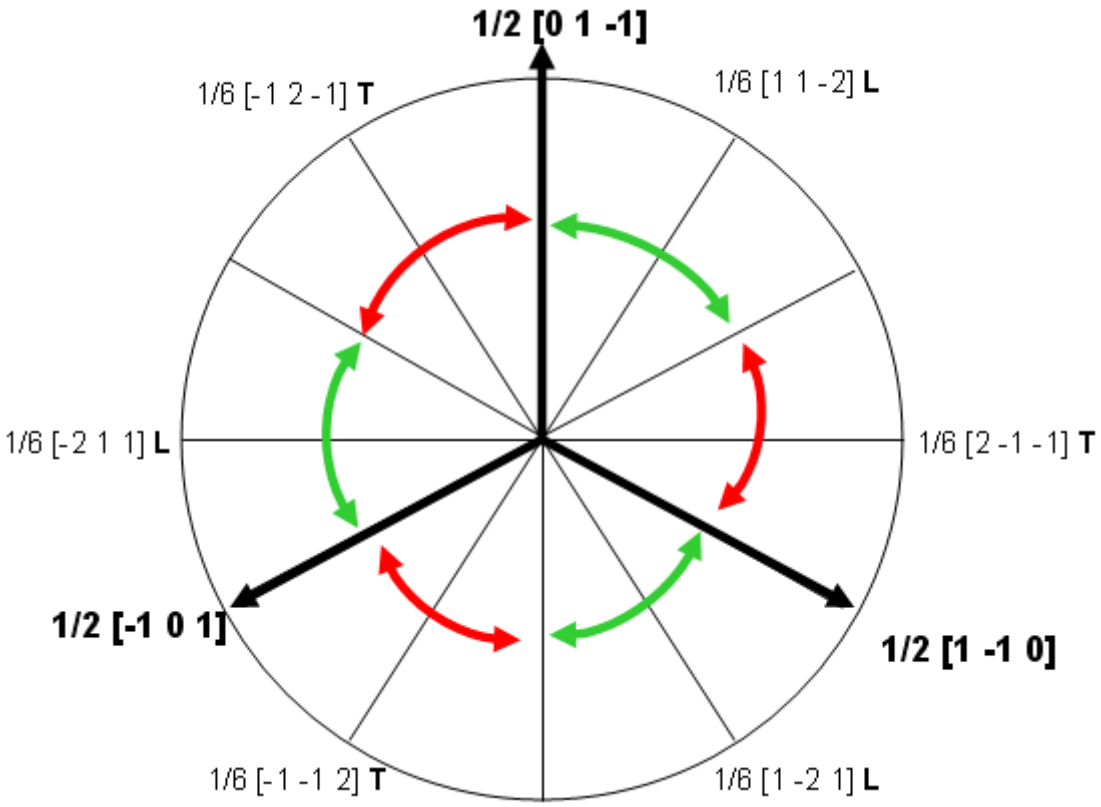

Figure 4.12 Dissociation possible (green arrow) and dissociation free (red arrow) zones based on full/partial Burgers vectors on a (111) plane.

4.6.8 Lower Dissociation Threshold

The lower dissociation threshold stress sets the minimum required resolved shear stress acting on the leading partial dislocation so that a dislocation can dissociate and initiate microtwinning. The lower dissociation threshold stress depends on the channel width and the stacking fault energy. A narrow γ matrix channel width is known to promote dislocation dissociation that can progress to microtwin evolution (Raujol et al., 2006). On the other hand, high stable stacking fault energy elevates the lower dissociation threshold stress as observed in the MPF simulation results shown in Figure 4.7. Therefore, the lower dissociation threshold stress can be estimated as

$$\kappa_{mt,o} = k_{mt} f_1(w) f_2(\Gamma_{SF}) \tag{4.26}$$

where w is the γ matrix channel width between secondary γ′ particles, assuming the disk alloy considered is supersolvus. The lower dissociation threshold stress is physically equivalent to the minimum resolved shear stress level acting on the leading partial dislocation required to initiate microtwinning. The relationship of the lower dissociation threshold stress in terms of γ matrix channel width to the stacking fault energy can be defined through analysis based on phase field model simulations.

4.6.9 Microtwin Dislocation Velocity

The shearing rate generated from microtwinning, according to Karthikeyan et al. (2006), is related to the microtwin velocity. In calculating the velocity, the model originally assumes that the tertiary γ′ particles hinder the dislocation movement and reduce the effective stress, i.e.,

$$\tau_{eff}{}^{\alpha} = \tau^{\alpha} - \frac{f_3 \Gamma_{pt}}{2 b_{tp}} \tag{4.27}$$

where τ is the applied resolved shear stress, b_{tp} is the Burgers vector of the twinning partial, f_3 is the tertiary γ' volume fraction, and Γ_{pt} is the activation energy for the pseudotwin formation.

In this work, however, the resolved shear stress τ^{α}_{lead} from Eq. (4.24) is used instead, neglecting the drag effects of tertiary γ'. Using the resolved shear stress, the dislocation velocity on the α^{th} slip system is estimated following the model of Karthikeyan et al. (2006), i.e.,

$$v^{\alpha} = \frac{b_{tp}}{x^2} D_{ord} \left\{ \ln\left(\frac{f_2\left(\Gamma_{pt} - \Gamma_{tt}\right)}{2\left(\tau^{\alpha}_{lead}\right) b_{tp} - f_2 \Gamma_{tt}} \right) \right\}^{-1} \operatorname{sgn}\left(\tau^{\alpha}_{lead}\right) \quad \text{for} \quad \frac{f_2\Gamma_{tt}}{2b_{tp}} < \tau^{\alpha}_{lead} < \frac{f_2\Gamma_{pt}}{2b_{tp}} \qquad (4.28)$$

To obtain this, the energy drop that results from transforming a pseudotwin to a true twin is equated to the work done by the resolved shear stress as it shears the γ matrix and secondary γ' precipitates via a microtwin. According to Kathikeyan et al. (2006), D_{ord} is the diffusion coefficient for ordering, x is the short range diffusion length, and Γ_{pt}, Γ_{tt} are pseudo and true twin activation energies, respectively. This relation is only valid when τ^{α}_{lead} is high enough to overcome the true twin activation energy and generate twins on the secondary γ' precipitates, $f_2\Gamma_{tt} / 2b_{tp}$; when τ^{α}_{lead} is less than $f_2\Gamma_{pt} / 2b_{tp}$, the theoretical upper limit is set by athermal pseudotwin generation.

4.6.10 Microtwin Density

In Karthikeyan's work (2006), the density of microtwins is assumed to be constant and is based on the value obtained at the end of the creep test by TEM observations; this leads to an overestimation of the density in the early stage of deformation. Therefore, the microtwin density should be assumed to evolve throughout the deformation process.

Microtwin density evolution can be formulated as a heterogeneous nucleation model. First, the microtwinning progress state can be defined as n/N, where n is the number of decorrelation sites and N is the total number of potential decorrelation sites. If $f(\tau_{lead})$ is defined as the probability of distribution of critical shear stress on the leading partial dislocation required for dissociation, the microtwinning progress state can be estimated by integrating $f(\tau_{lead})$ over a stress range, i.e.,

$$\int_{0}^{\tau_{lead}} f\left(\tau_{lead}\right) d\tau_{lead} = \left(\frac{n}{N}\right) \qquad \text{for } \tau_{lead} \in \left(\kappa_{mto}, \kappa_{mtu}\right] \tag{4.29}$$

where κ_{mtu} and κ_{mto} are upper and lower threshold stress for dislocation dissociation estimated in Section 4.6.8. The rate form of the microtwin density ρ_{mt}^{α} in a given volume V can be defined as

$$\frac{d\rho_{mt}^{\alpha}}{dt} = \frac{\bar{l}}{V}\frac{dn}{dt} \tag{4.30}$$

where $\bar{l}$ is the dislocation segment length generated by a decorrelation event. By rearranging Eq. (4.30) and substituting into (Eq. 4.29), the microtwin density evolution may be written as

$$\dot{\rho}_{mt}^{\alpha} \approx \left(\frac{N}{V}\bar{l}\right) f\left(\tau_{lead}^{\alpha}\right) \dot{\tau}_{lead}^{\alpha} \tag{4.31}$$

Here, $\bar{l}$ can be assumed to be equivalent to the critical size of secondary γ′ precipitates d_{diss} which promotes dislocation dissociation. The number of potential dislocation dissociation sites in a give volume is defined as

$$\frac{N}{V} = \frac{1}{\left(d_{diss} + w\right)^3}\left(f_{diss} + f_{p3}\alpha^3\right) \tag{4.32}$$

where f_{diss} is a part of the volume fraction of secondary γ′ precipitates with the critical size d_{diss}, w is the channel width between secondary γ' particles with d_{diss}, and α is an effective volume fraction factor for tertiary γ' particles.

It is assumed that some tertiary γ' particles cluster together and behave similar to the larger secondary γ' particles by promoting dislocation decorrelation. Therefore, the volume fraction of tertiary γ' precipitates is factored in Eq. (4.32) and contributes to the microtwinning potential sites. Within a cluster of small particles, however, narrow γ

matrix channels exist between tertiary γ' particles, and the volume fraction of tertiary γ' precipitates f_{p3} is not a reasonable representation of the volume taken by the clusters. Hence, the effective volume fraction factor α^3 is multiplied to the volume fraction of tertiary γ' particles so that the space between particles can be taken into account. Eq. (4.32) can be substituted into Eq. (4.31) and the microtwin density rate can be given by

$$\dot{\rho}_{mt}^{\alpha} = \frac{d_{diss}}{\left(d_{diss}+w\right)^3}\left(f_{diss}+f_3\alpha^3\right) f\left(\tau_{lead}^{\alpha}\right)\left(\tau_{lead}^{\alpha}-\kappa_{mto}\right)^m \dot{\tau}_{lead}^{\alpha} \tag{4.33}$$

The probability function $f(\tau_{lead})$ can be defined as

$$f\left(\tau_{lead}^{\alpha}\right) = \frac{m+1}{\left(\kappa_{mtu}-\kappa_{mto}\right)^{m+1}}\left(\tau_{lead}^{\alpha}-\kappa_{mto}\right)^m, \qquad \text{for } \kappa_{mtu} < \tau_{lead}^{\alpha} < \kappa_{mto} \tag{4.34}$$

where m is a microstructure parameter with ($0 \le m \le 1$) and controls the rate of the probability distribution reaching 1. Now, the microtwin density evolution can be rewritten by introducing Eq. (4.34) to Eq. (4.31), i.e.,

$$\dot{\rho}_{mt}^{\alpha} = \frac{d_{diss}}{\left(d_{diss}+w\right)^3}\left(f_{diss}+f_3\alpha^3\right)\frac{m+1}{\left(\kappa_{mtu}-\kappa_{mto}\right)^{m+1}}\left(\tau_{lead}^{\alpha}-\kappa_{mto}\right)^m \dot{\tau}_{lead}^{\alpha} \tag{4.35}$$

The formulated microtwin density evolution shows low growth rate in the early stage of microtwinning followed by a rapid increase until it approaches near the microtwin saturated state.

4.6.11 Microtwinning Induced Inelastic Shearing Rate

The microtwin-induced shearing rate suggested in Eq. (4.14) is claimed to satisfactorily estimate the macroscopic strain rate under creep loading conditions, especially for René 104 (Karthikeyan et al., 2006). Therefore, the model can be empirically implemented in a constitutive model at a higher length scale to estimate the

deformation behavior under a microtwin dominant deformation condition. However, the increase in strain rate of Karthikeyan's model (2006) is mainly due to the increase in evolution of the secondary γ' precipitate volume fraction and the decrease in the tertiary γ' precipitate volume fraction, both of which are not defined in the literature.

The shearing rate induced by the microtwinning evolution can be implemented in an ABAQUS User MATerial (UMAT) by computing the magnitudes of the resolved stress states acting on all 24 leading and trailing partial dislocations at each integration point. When the maximum magnitude of the resolved shear stress acting on any of 12 leading partial dislocations exceeds the lower dissociation threshold stress, the slip system associated with the maximum leading partial dislocation is noted, and this triggers the microtwin evolution. For the rest of the slip systems, only the full dislocation glide is considered as the operative deformation mechanism. The microtwin-triggered slip system then drives the microtwin evolution until the resolved shear stress acting on the leading partial reaches the theoretical upper threshold stress discussed in section 4.4 or the upper limit of the maximum resolved shear stress that was introduced in Eq. (4.28) (Kathikeyan et al., 2006).

Table 4.1 Octahedral slip systems and associated Shockley partial dislocations.

Full	Leading	Trailing
$\frac{1}{2}[01\bar{1}]$	$\frac{1}{6}[11\bar{2}]$	$\frac{1}{6}[\bar{1}2\bar{1}]$
$\frac{1}{2}[\bar{1}01]$	$\frac{1}{6}[\bar{2}11]$	$\frac{1}{6}[\bar{1}\bar{1}2]$
$\frac{1}{2}[1\bar{1}0]$	$\frac{1}{6}[1\bar{2}1]$	$\frac{1}{6}[2\bar{1}\bar{1}]$
$\frac{1}{2}[0\bar{1}1]$	$\frac{1}{6}[1\bar{1}2]$	$\frac{1}{6}[\bar{1}\bar{2}1]$
$\frac{1}{2}[\bar{1}0\bar{1}]$	$\frac{1}{6}[\bar{2}\bar{1}\bar{1}]$	$\frac{1}{6}[\bar{1}1\bar{2}]$
$\frac{1}{2}[110]$	$\frac{1}{6}[12\bar{1}]$	$\frac{1}{6}[211]$
$\frac{1}{2}[011]$	$\frac{1}{6}[\bar{1}12]$	$\frac{1}{6}[121]$
$\frac{1}{2}[10\bar{1}]$	$\frac{1}{6}[21\bar{1}]$	$\frac{1}{6}[1\bar{1}\bar{2}]$
$\frac{1}{2}[\bar{1}\bar{1}0]$	$\frac{1}{6}[\bar{1}\bar{2}\bar{1}]$	$\frac{1}{6}[\bar{2}\bar{1}1]$
$\frac{1}{2}[0\bar{1}\bar{1}]$	$\frac{1}{6}[1\bar{2}\bar{1}]$	$\frac{1}{6}[\bar{1}\bar{1}\bar{2}]$
$\frac{1}{2}[101]$	$\frac{1}{6}[112]$	$\frac{1}{6}[2\bar{1}1]$
$\frac{1}{2}[\bar{1}10]$	$\frac{1}{6}[\bar{2}1\bar{1}]$	$\frac{1}{6}[\bar{1}21]$

4.7 Static Thermal Recovery

The creep behavior is often considered as an important deformation process in single crystal Ni-base superalloys, especially for turbine blades. The creep strength is, however, also crucial in disk alloy applications, as constant loads are experienced at high temperatures.

In addition to microtwinning-driven creep deformation, diffusional-assisted dislocation glide also plays an important role in low rate deformation of disk alloys. In Ni-base superalloys, coarsening of γ' precipitates under long term creep due to the diffusional effect at elevated temperatures can also be observed in experiments. As the creep strength is determined by the migration of dislocations which is interrupted by γ' precipitates, incorporating such influence in the crystal plasticity model is crucial if the creep or relaxation are relevant loading types in the application of the material considered.

In single crystal Ni-base superalloys, much research has attempted to model high temperature creep behaviors according to various mechanisms. In the work of MacLachlan et al., (2001), the decrease in strength of superalloys is modeled by a damage mechanics model along with a global damage tensor which incorporates the effect of resolved shear stresses and strain on slip systems in a global sense. On the other hand, the dislocation network spacing at the γ/γ' interface is claimed to be influenced under creep conditions, which affects dislocation climb kinetics; hence it is responsible for an increase in the creep strain rate (Yaguchi et al., 2002). Li and Wahi (1995) analyzed TEM images of polycrystalline Ni-base superalloy IN138LC specimens under creep and concluded that the high local internal stress in γ' phase attributed to the increase in the creep rate. In the work of Svoboda et al., diffusional-assisted creep model considers contributions from the volume change due to generation or annihilation of vacancies and from linear viscous creep independently (2006).

Microtwins usually shear both γ matrix and γ' precipitates providing strains on the order of 1% and extend across entire grains (Kovarik et al., 2009a). This is the dominant

deformation mechanism under creep without prior overloads above the yield point. In order to reflect the tertiary creep behavior observed in the microtwinning dominant deformation condition without implementing coarsening of γ' precipitates, the static thermal recovery effect can be considered in the dislocation density evolution, i.e.,

$$\dot{\rho}_{\lambda}^{\alpha}=h_{\lambda}^{\alpha\alpha}\left\{Z_0+k_1\sqrt{\rho_{\lambda}^{\alpha}}-k_2\rho_{\lambda}^{\alpha}\right\}\left|\dot{\gamma}_{\lambda}^{\alpha}\right|-c_R\left\langle\rho_{\lambda}^{\alpha}-\rho_o^{\alpha}\right\rangle^{m_R}\exp\left(-\frac{Q_s}{kT}\right) \tag{4.26}$$

where ρ_o^{α} is the recovery threshold, and Q_s is the activation energy for the diffusion of the γ'-forming elements within the matrix (Stevens and Flewitt, 1979), and c_R and m_R can be determined from experiments.

CHAPTER 5

CRYSTAL PLASTICITY MODEL ANALYSIS AND STATE VARIABLE CHARACTERIZATION

5.1 Introduction

The crystal plasticity model introduced in the previous chapter is implemented as a User MATerial (UMAT) in a 3D finite element model (FEM) generated in ABAQUS (Simulia, 2006). The UMAT estimates the response for a given input loading condition using a fully implicit integration scheme based on Newton-Raphson iteration and an incremental line search algorithm (McGinty, 2001). The polycrystal model is comprised of 25 grains, and each grain comprises eight of 8-noded cube elements as shown in Figure 5.1(a). The orientation of each grain is determined by the Euler angles which are randomly assigned. Within a grain, all eight elements are oriented with the identical set of Euler angles, but the deformation of each is affected by the surrounding elements, hence each demonstrates a different deformation response. The model is loaded on one surface by displacement to represent strain-controlled loading, or by a force for stress-controlled loading (e.g., creep) in a global axial direction: the surface on the opposite side is constrained in the same axial direction. The model is assumed to be symmetric over the x, y and z axes with respect to one vertex of the constrained face.

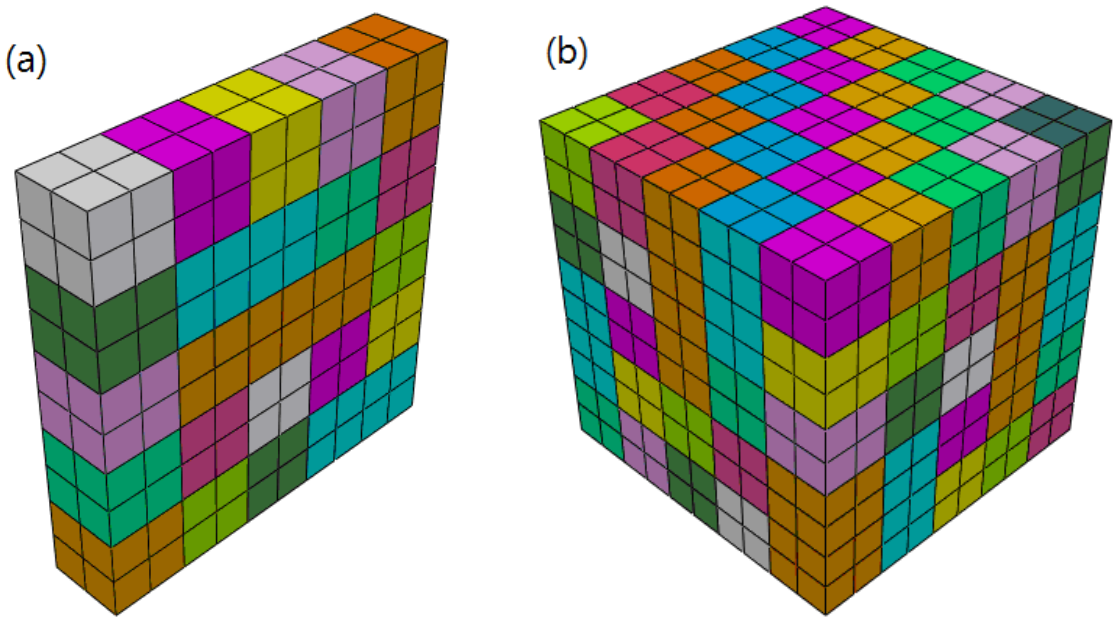

Figure 5.1 The FEM for the crystal plasticity constitutive relation with (a) 200 elements (25 grains and 8 elements per grain) and (b) 1000 elements (125 grains and 8 elements per grain).

The finite element model needs to contain a sufficient number of realistic shaped grains to adequately represent the averaged response of a polycrystal material. However, increasing the number of elements comprising complex shaped grains in a polycrystal model requires substantial computation power and time. The main objective of this analysis is to understand the state variable evolution of the crystal plasticity model, so that a proper foundation of the constitutive relation for hierarchical modeling can be established. Therefore, a reasonably small sized model with a uniform grain shape and size, shown in Figure 5.1(a) has been implemented. The 200 element model has been proved to adequately represent the averaged stress-strain response when compared to 512 grain Voronoi tessellation models (Shenoy, 2006). As an additional validation step, a 1000 element model shown in Figure 5.1(b) was subjected to a simple cyclic load, and its response has been compared to the 200 element model response; the result has been

proved to be very close. The 200 element model, however, can still be insufficient to accurately represent the true response of polycrystal Ni-base superalloys, especially under long term creep. However, for the purpose of characterizing state variable evolution, the 200 element model is extensively used without further verifications, because its quick computational time allows easier modifications to the constitutive relation.

The model analysis presented in this chapter is designed to characterize the role of state variables under different loading conditions and to suggest possible improvements for the model representation. In order to avoid any confusion on state variable evolution analysis, relatively simple loading conditions are employed. The strain-controlled loading begins with two fully reversed cycles with 2% amplitude of strain at a rate of 10^{-3}/s followed by a 500s hold period at 2% tensile strain. Under the stress-controlled loading, tensile stress of 838 MPa is applied and held for 550 hours to observe the creep behavior and to highlight the microtwinning dominant deformation process. All simulations are assumed to be at 650°C.

The microstructure attributes used in this crystal plasticity models are obtained from the averaged values of supersolvus treated ME3 specimens from the rim section of disks measured by Gabb et al. (2004), which are listed in Table 5.1.

Table 5.1 Average microstructure attributes used in the analysis.

Primary γ' volume fraction	Secondary γ' volume fraction	Secondary γ' precipitate size (nm)	Tertiary γ' volume fraction	Tertiary γ' precipitate size (nm)	Grain size (μm)
0	0.52	180	0.01	30	30.4

Except for the microstructure attributes and directly computable constants (e.g., particle spacing), many parameters are based on Shenoy's work which have been previously calibrated to IN-100 experimental data (2006). The parameters associated with the microtwinning-induced shearing rate are tentatively assumed based on preliminary MPF results (e.g., lower and upper dislocation dissociation thresholds), or they are based on the work of Karthikeyan et al. (2006), in which, the authors claim the model response matched fairly well with the experimental data of René104. The implemented model parameters are not calibrated to ME3 data, as experimental data with detailed microstructure attributes are not yet available. The analysis on state variables with the tentative constants, however, appears to be adequate in capturing evolution of state variables and understanding their effects on macroscopic responses.

The analysis can be divided into two categories based on applied loading conditions: strain-controlled and stress-controlled. As the finite element model contains 200 elements with 18 slip systems activated in each element, only four to five elements are randomly selected for analysis. As the trend of state variable evolution in each selected element is found to be similar, analysis on one of the elements is presented in this work. Furthermore, the state variables associated with the most active slip system appear to dominate the evolution in most of cases, while the effects of the less active slip systems are relatively insignificant. Therefore, instead of demonstrating state variable evolution of all 18 slip systems, analysis is of three to four of the most significant slip systems is presented, including the active microtwinning system.

Table 5.2 Slip systems and numbering convention in analysis

		Slip Plane	Slip Direction
Octahedral Slip	Slip 1	(111)	$[01\bar{1}]$
	Slip 2	(111)	$[\bar{1}01]$
	Slip 3	(111)	$[1\bar{1}0]$
	Slip 4	$(1\bar{1}\bar{1})$	$[0\bar{1}1]$
	Slip 5	$(1\bar{1}\bar{1})$	$[\bar{1}0\bar{1}]$
	Slip 6	$(1\bar{1}\bar{1})$	$[110]$
	Slip 7	$(\bar{1}1\bar{1})$	$[011]$
	Slip 8	$(\bar{1}1\bar{1})$	$[10\bar{1}]$
	Slip 9	$(\bar{1}1\bar{1})$	$[\bar{1}\bar{1}0]$
	Slip 10	$(\bar{1}\bar{1}1)$	$[0\bar{1}\bar{1}]$
	Slip 11	$(\bar{1}\bar{1}1)$	$[101]$
	Slip 12	$(\bar{1}\bar{1}1)$	$[\bar{1}10]$
Cube Slip	Slip 13	(100)	$[011]$
	Slip 14	(100)	$[01\bar{1}]$
	Slip 15	(010)	$[101]$
	Slip 16	(010)	$[10\bar{1}]$
	Slip 17	(001)	$[110]$
	Slip 18	(001)	$[\bar{1}10]$

5.2 Loading Histories and Responses

5.2.1. Strain-Controlled Cyclic Loading

The strain-controlled loading analysis was based on the simulation with two cycles at a rate of 10^{-3}/s followed by a strain hold period of 500 seconds. The fully reversed cycles are applied to observe the evolution of state variables subjected to reversed plastic strain,

and the short dwell period is to study the state variable evolution during stress relaxation. The applied strain loading history and the corresponding stress-strain response are presented in Figure 5.2 and Figure 5.3, respectively.

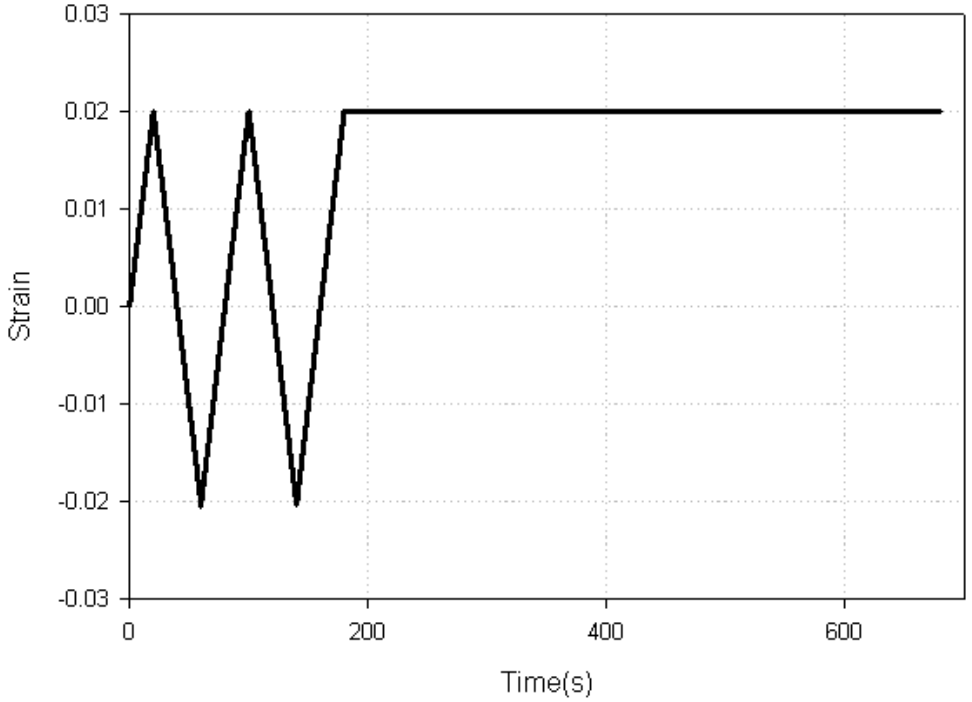

Figure 5.2 Imposed strain-time loading history for the strain-controlled crystal plasticity simulation.

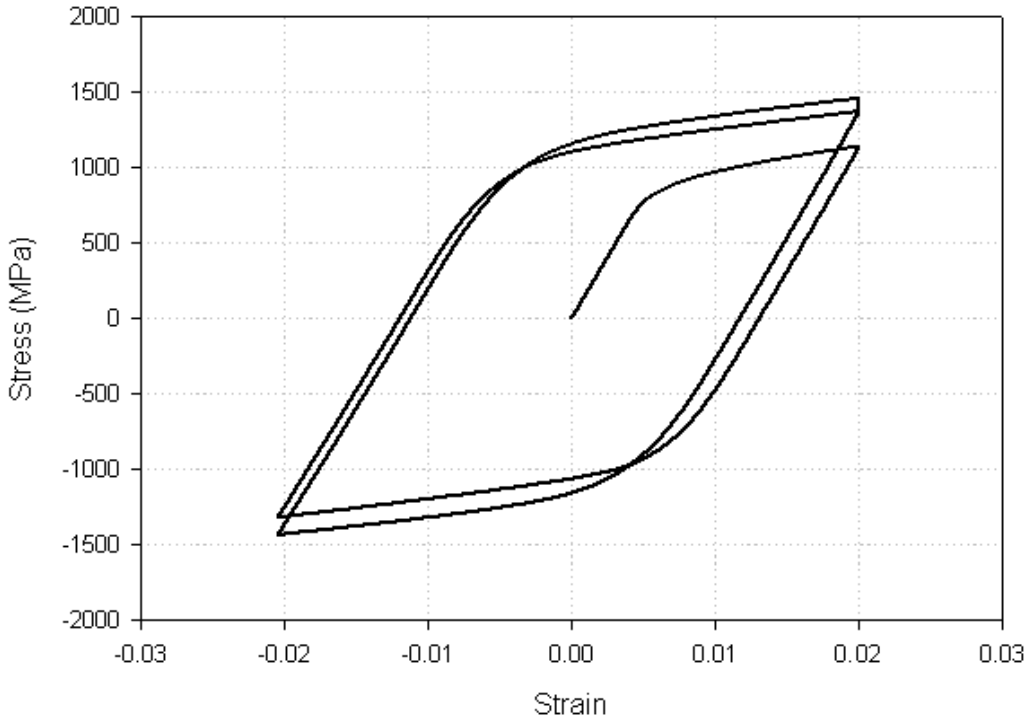

Figure 5.3 Macroscopic stress-strain response for the strain-controlled crystal plasticity simulation at 650°C.

The stress-strain response demonstrates slight hardening over cycles and relaxation during the dwell period. The hardening during the first cycle is found to be more significant compared to the hardening during the second cycle, which is reduced slightly during the 500 second dwell period.

5.2.2 Stress-Controlled Loading (Creep)

The stress-controlled loading condition is applied to highlight deformation dominated by microtwinning under creep loading conditions without prior plastic strain. The stress-controlled loading ramps up to 838MPa over 100 seconds, then force is maintained for 550 hours. The creep strain is estimated by subtracting the strain at the onset of hold from the total strain, and is plotted in Figure 5.4.

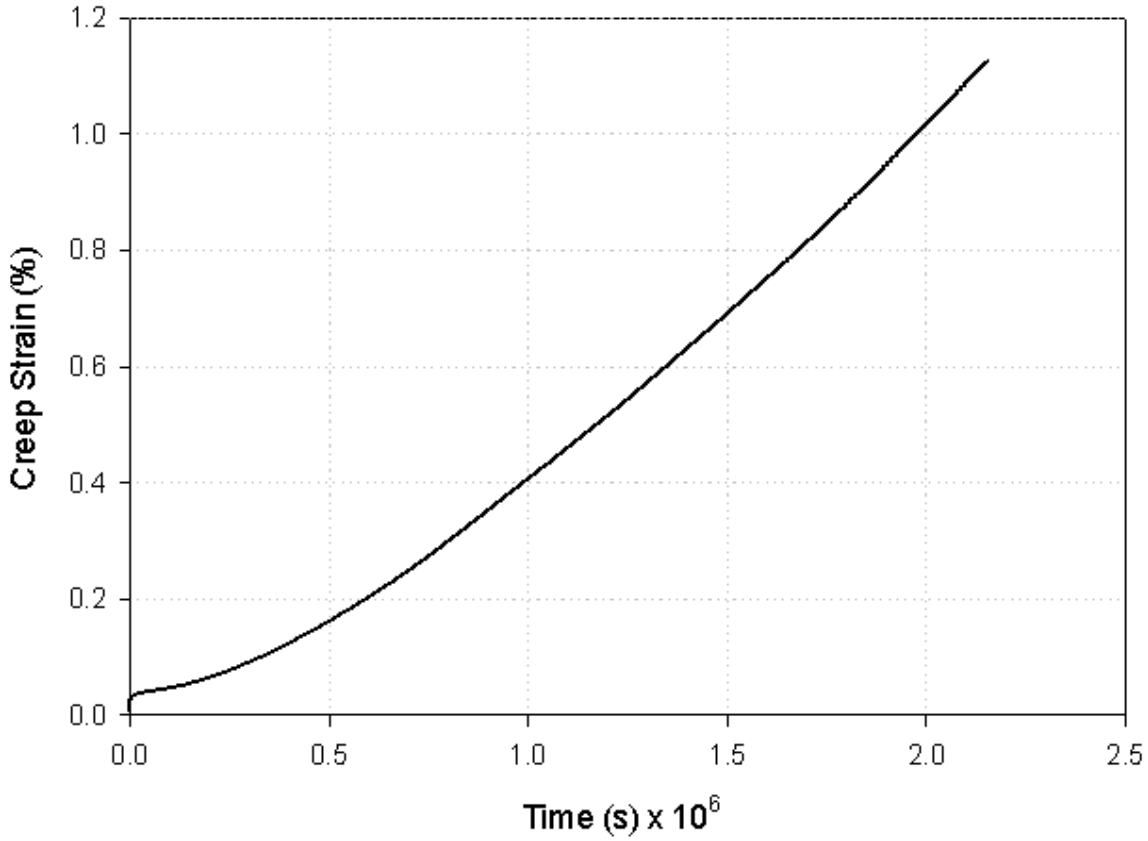

Figure 5.4 Creep response for stress of 838 MPa of stress-controlled crystal plasticity simulation at 650°C.

5.3 State Variable Analysis

5.3.1 Shearing Rate Analysis

In the crystal plasticity model, the shearing strain rate of a slip system is specified by the flow rule using the resolved shear stress acting on the slip system. The flow rule is formulated so that when the flow stress becomes nonzero, the shearing rate magnitude is increased and the inelastic deformation begins. The flow rule of the crystal plasticity model introduced in Chapter 3 is composed of two terms: shearing rate by dislocation glide and the microtwin-induced shearing rate. Both terms are activated only when the

corresponding resolved shear stress on a slip system overcomes the threshold stress of each. The elastic deformation regime is characterized by zero slip system shearing rates.

Each term of the shearing rate is activated individually depending on the applied stress condition. The influence of each shearing rate term on deformation also depends on the loading condition (e.g., stress level, strain rate and temperature), and their features become prominent under distinct conditions. Hence, the analysis conducted in this section is focused on demonstrating the characteristics of each term of the flow rule.

The fully reversed cyclic strain-controlled loading highlights the effect of the shearing rate associated with dislocation glide. When the finite element model is loaded at a rate of 10^{-3}/s, the shearing rate increases rapidly; once the overstress becomes positive and inelasticity is initiated as depicted in Figure 5.5. The shearing rates presented in Figure 5.5 are for the slip systems that have high shearing rate magnitudes compared to other slip systems, which indicates that these slip systems are most favorably oriented with respect to the loading direction

.

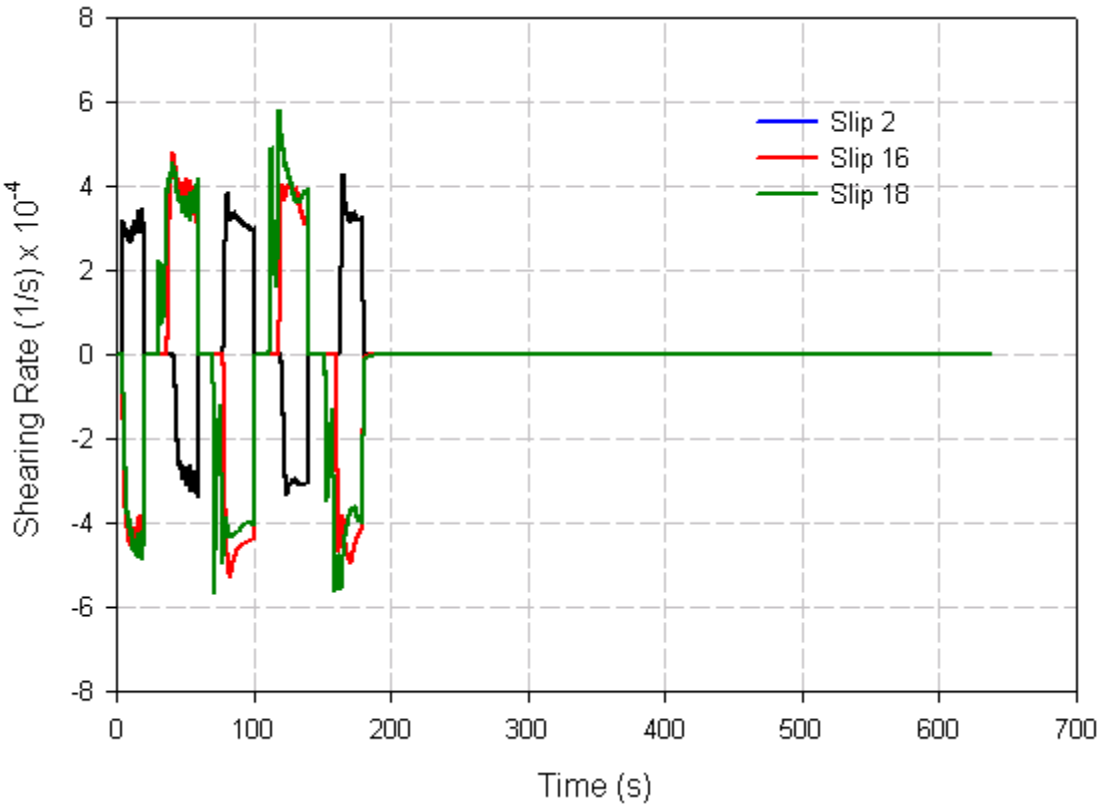

Figure 5.5 Shearing rates comparison under strain-controlled fully reversed cyclic loading with 2% amplitude.

The shearing rate magnitudes suddenly drop to zero when the load is reversed which is the sign of the deformation state returning to the elastic domain. In this circumstance the shearing rates remain zero until the inelastic deformation resumes in the loading direction. The shearing rate jumps back in the opposite direction of the prior reversal when the inelasticity begins, but quickly drops again due to the consequent back stress evolution which lowers the overstress magnitude. Unlike the smooth drop observed in the first cycle, complex waves are observed right after the drop after the first cycle. This complexity emerges from the combined effects of the back stress evolution and the threshold stress evolution which will be discussed in the following sections. The signs of

the shearing rates are determined by the slip directions relative to the loading direction (they are negative when loaded opposite to the slip direction).

In contrast, the microtwin-induced shearing rate is formulated so that it is directly related to the magnitude of the maximum resolved shear stress acting on the leading partial dislocation; it is only active on the microtwinning system. Also, the microtwin-induced shearing rate should not affect the total shearing rate if the loading condition is not favorable for microtwins to initiate. For a better comparison, the microtwin-induced shearing rate is plotted next to the total shearing rate on the microtwinning system (Slip system 2 of Figure 5.5) in Figure 5.6 for the same strain-controlled load. The microtwin induced shearing rate stays inactive or extremely low, minimally affecting the total shearing rate on the slip system. Under cyclic loading conditions with a high strain rate, the shearing rate is dictated by the first term of the flow rule, which indicates deformation by dislocation glide as observed experimentally.

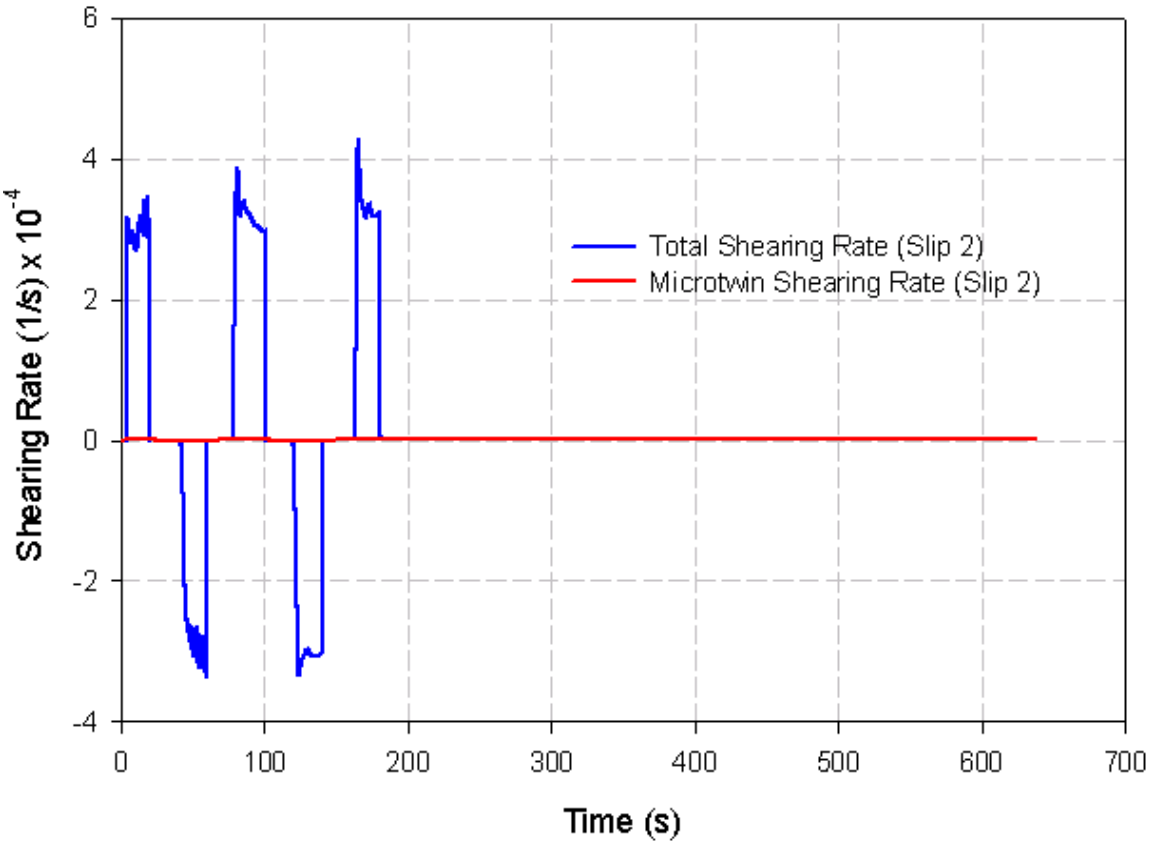

Figure 5.6 Total shearing rate and microtwin associated shearing rate on Slip 2 (microtwinning system) under strain-controlled fully reversed cyclic loading with 2% amplitude.

Under the stress-controlled creep condition, the shearing rate behaves quite differently. When measured from the initial point of the creep, the shearing rate magnitude increases rapidly, as the input stress rate is on the order of 10 MPa/s. Once the stress level is held at the maximum load (i.e., 838 MPa), however, the shearing rate quickly drops, as demonstrated in Figure 5.7.

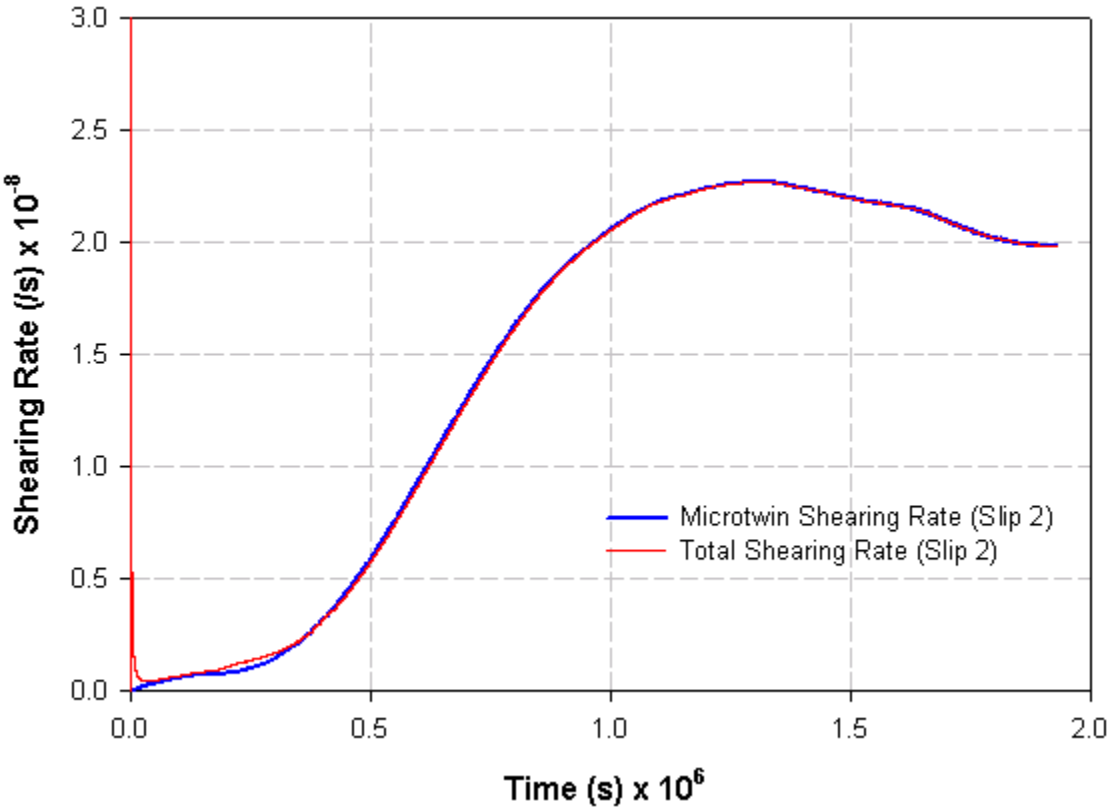

Figure 5.7 Total shearing rate and microtwin-induced shearing rate under stress-controlled creep at 838 MPa.

Once the load is held and the shearing rate driven by dislocation glide is decreased, the shearing rate is controlled by microtwinning. The shearing rate gradually increases and deformation beyond the initiation of the creep load is governed by microtwinning. Although the maximum magnitude of the shearing rate instantly reached by dislocation glide surpasses the magnitude reached by microtwinning (beyond approximately 10^4s), the total shear strain generated by dislocation glide is not significant. The strain experienced by the slip system can be approximated by the area under the shearing rate curve, and it is clear that the creep behavior is dominated by microtwinning.

5.3.2. Dislocation Density Analysis

The dislocation density is closely related to the inelastic deformation and the hardening behavior of Ni-base superalloys. Therefore, evolution of state variables in the crystal plasticity framework (e.g., back stress and the threshold slip resistance) is based on the evolution of dislocation density. Dislocation density evolves when the shearing rate of the slip system is nonzero. For all slip systems shown in Figure 5.8, the dislocation density stays constant when the loading direction is reversed in the elastic domain, then restarts to grow upon reverse yielding. The dislocation density evolution is more rapid and of higher magnitude for the Slip system 18, which implies that substantial inelastic deformation has occurred on the slip system.

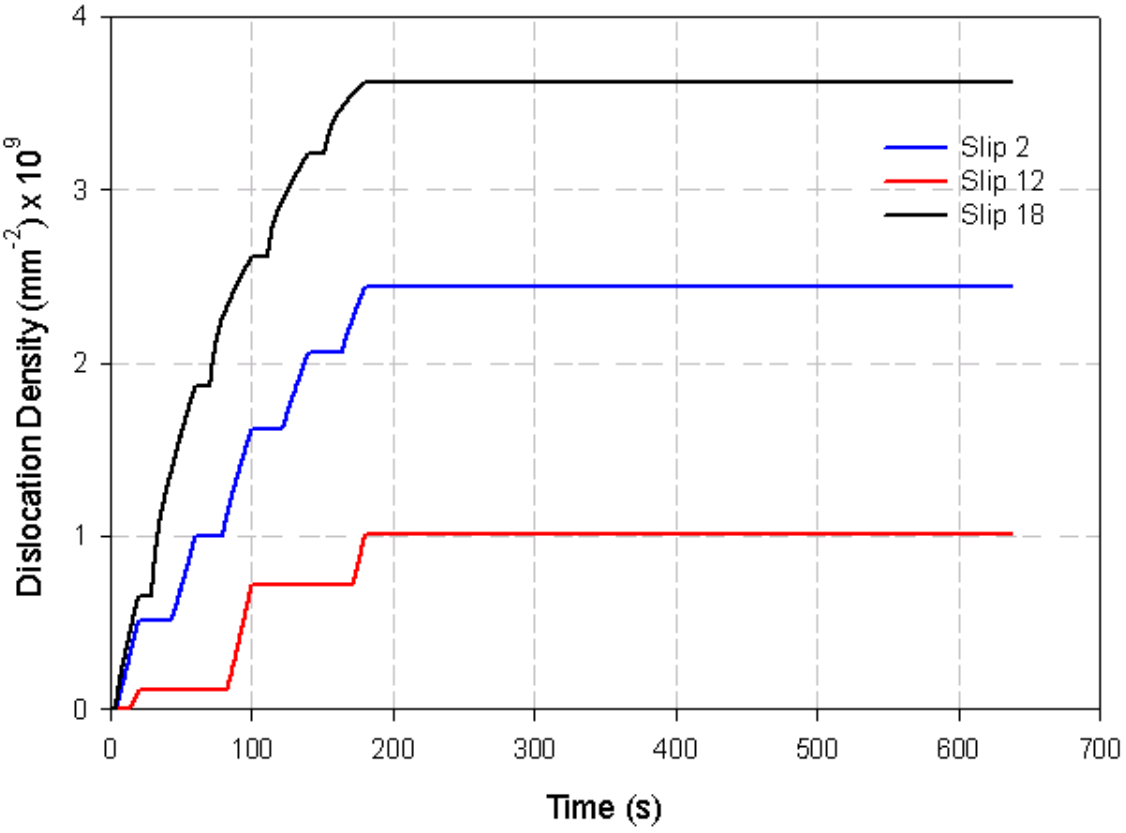

Figure 5.8 Dislocation density under strain-controlled fully reversed cyclic loading at 2% amplitude.

The dislocation density evolution of the same grain/element exhibits a slightly different behavior when it is subjected to stress-controlled loading. The dislocation density keeps increasing even after the load is held at a constant stress, because both the shearing rate and the overstress are nonzero under creep.

5.3.3. Back Stress Analysis

The back stress can be considered as the single most influential crystal plasticity state variable on the macroscopic behavior of Ni-base superalloys. The back stress captures the directional effect and determines the overall shape of the stress-strain curve. The back stress of three slip systems under cyclic strain-controlled load is displayed in Figure. 5.9.

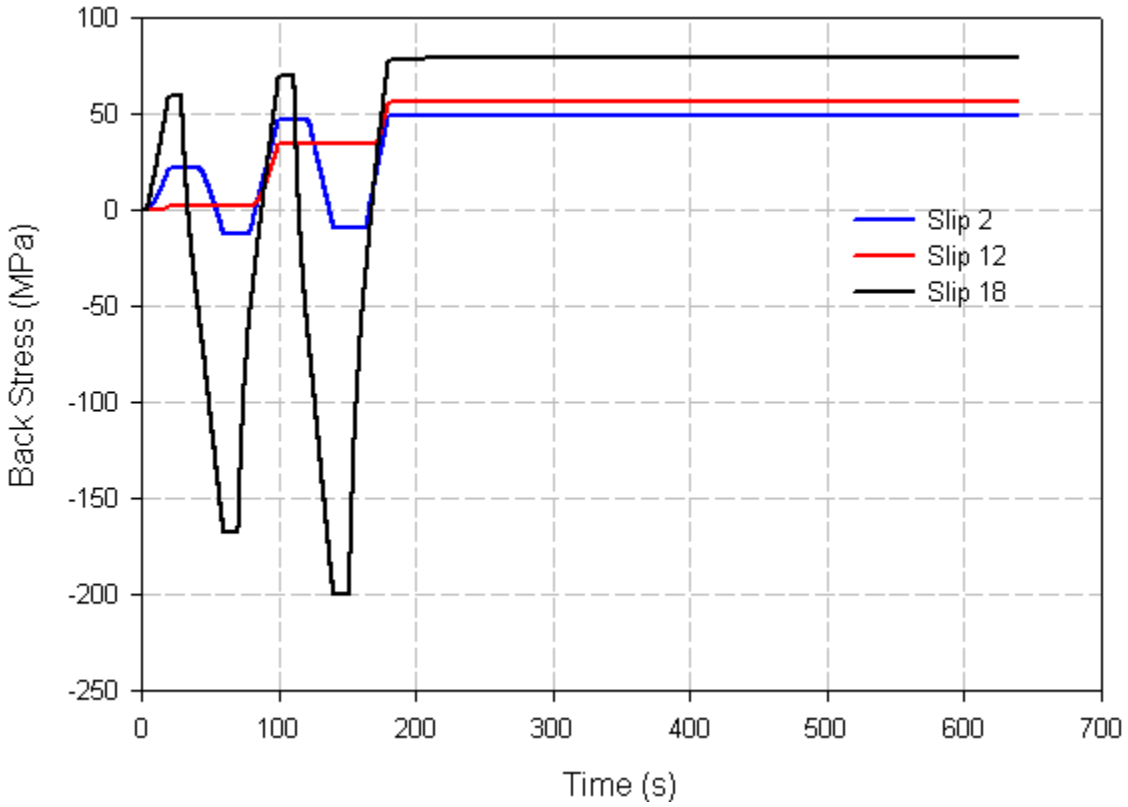

Figure 5.9 Back stress evolution under strain-controlled fully reversed cyclic loading at 2% amplitude.

Back stress in the crystal plasticity model is formulated to rapidly evolve depending on the magnitude of the shearing rate. In Figure 5.9, the back stress of each slip system has a small plateau at the local maxima or minima occurring at the end of each reversal, which indicates the elastic regime defined by zero shearing rates. Therefore, the subsequent rapid increase or decrease of back stress is due to the slip system undergoing inelastic deformation. On the Slip system 12 of Figure 5.9, back stress is evolving only in one direction (tensile), and this is because only elastic deformation is experienced in the opposite direction (compressive).

5.3.4 Threshold Slip Resistance

The threshold slip resistance of each slip system is proportionally related to the square root of the dislocation density via the Taylor hardening term. Therefore, the growth of the dislocation density is the main source of hardening in the threshold slip resistance. In contrast, the initial critical resolved shear stress κ_o^α of the octahedral slip system involves a non-Schmid stress on primary, secondary and cube slip systems τ_{pe}^α, τ_{se}^α, τ_{cb}^α, respectively. This means that the resolved shear stresses are independent on the other slip systems of the slip plane due to dislocation core spreading effects. Therefore, the threshold slip resistance evolution of the cube slip system does not contribute to the non-Schmid stress, and it is only dependent on the dislocation density evolution. In contrast, on the octahedral slip system, the slip direction effect is added to the evolution of the threshold slip resistance via the non-Schmid stress, particularly volume fraction of γ' precipitates is high. Therefore, when cyclically loaded, the initial threshold stress of all slip systems is equivalent around 300 MPa as seen in Figure 5.12. The increase and

decrease of the threshold slip resistance on Slip systems 2, 10 and 12 is due to the non-Schmid effect. In contrast, the threshold slip resistance on Slip system 18 is relatively smoothly growing with absence of any non-Schmid effect.

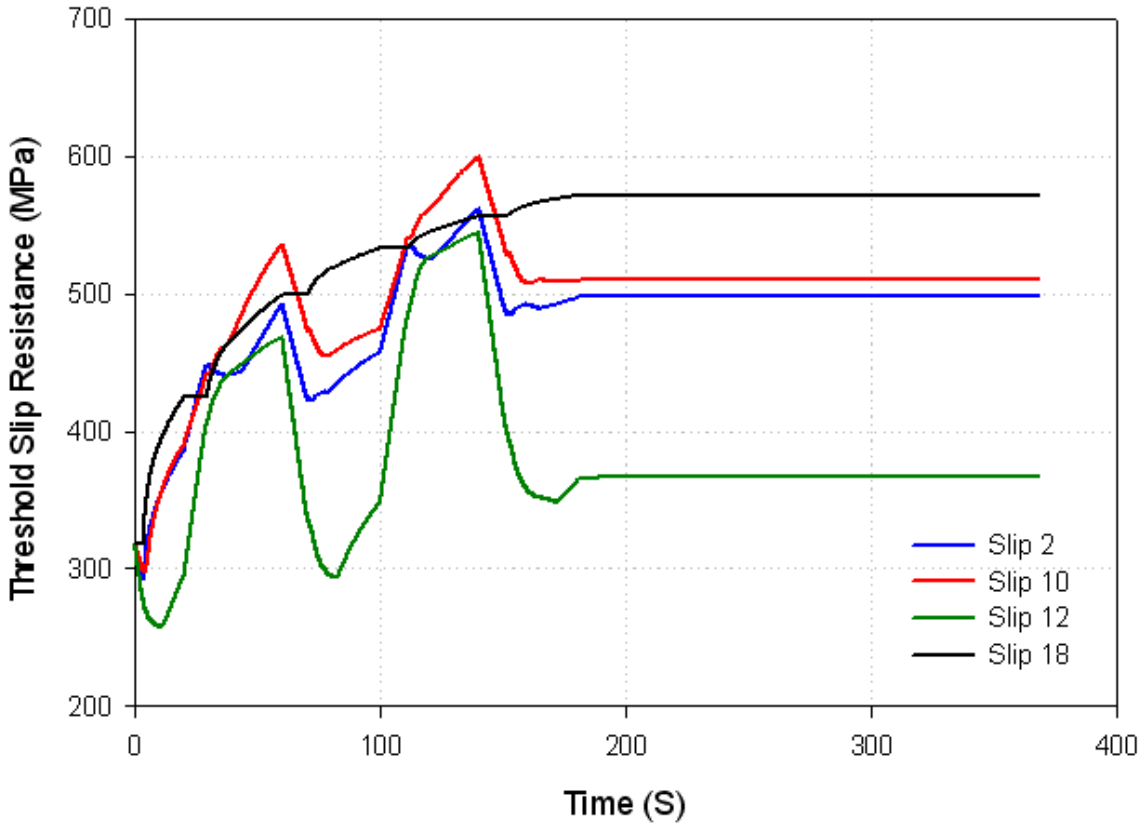

Figure 5.10 Slip resistance threshold stress under strain-controlled fully reversed cyclic loading with 2% amplitude.

5.3.5. Microtwin Velocity and Density

Microtwinning is assumed to occur on only one slip system within a grain. Therefore, both microtwin velocity and density are analyzed only on the microtwinning slip system (Slip system 2 for the selected grain).

The microtwin velocity is nearly proportional to the resolved shear stress acting on the leading partial direction, which indicates that the movement of a microtwin is proportional to the magnitude of stress resolved on the leading partial. Therefore, the

microtwin velocity subjected to stress-controlled creep conditions remains fairly linear as shown in Figure 5.11.

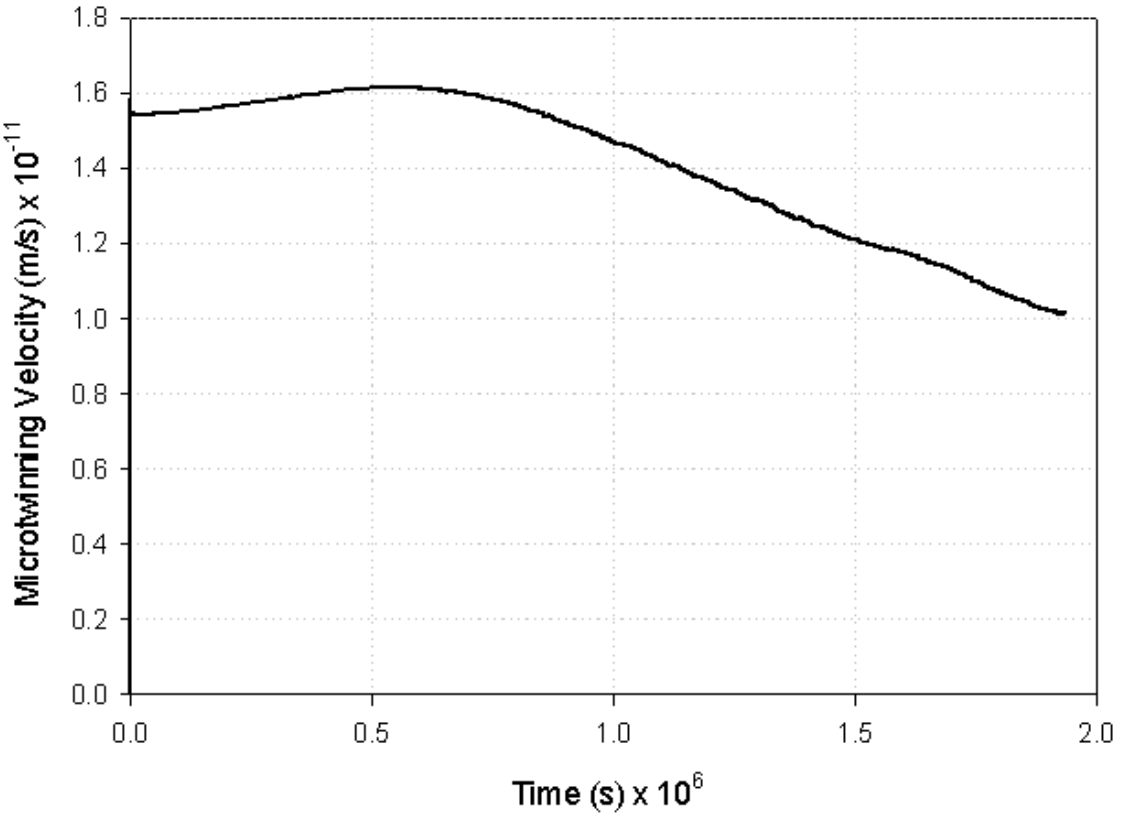

Figure 5.11 Microtwin velocity on microtwinning system under stress-controlled creep loading condition at 838 MPa.

In contrast, the microtwin density is formulated so that its evolution is governed by both the magnitude and the rate of the resolved shear stress acting on the leading partial. The microtwin density is also formulated to evolve slowly near the lower threshold stress, after which the evolution rate gradually increases until it settles near the upper limit of the resolved shear stress as shown in Figure 5.12.

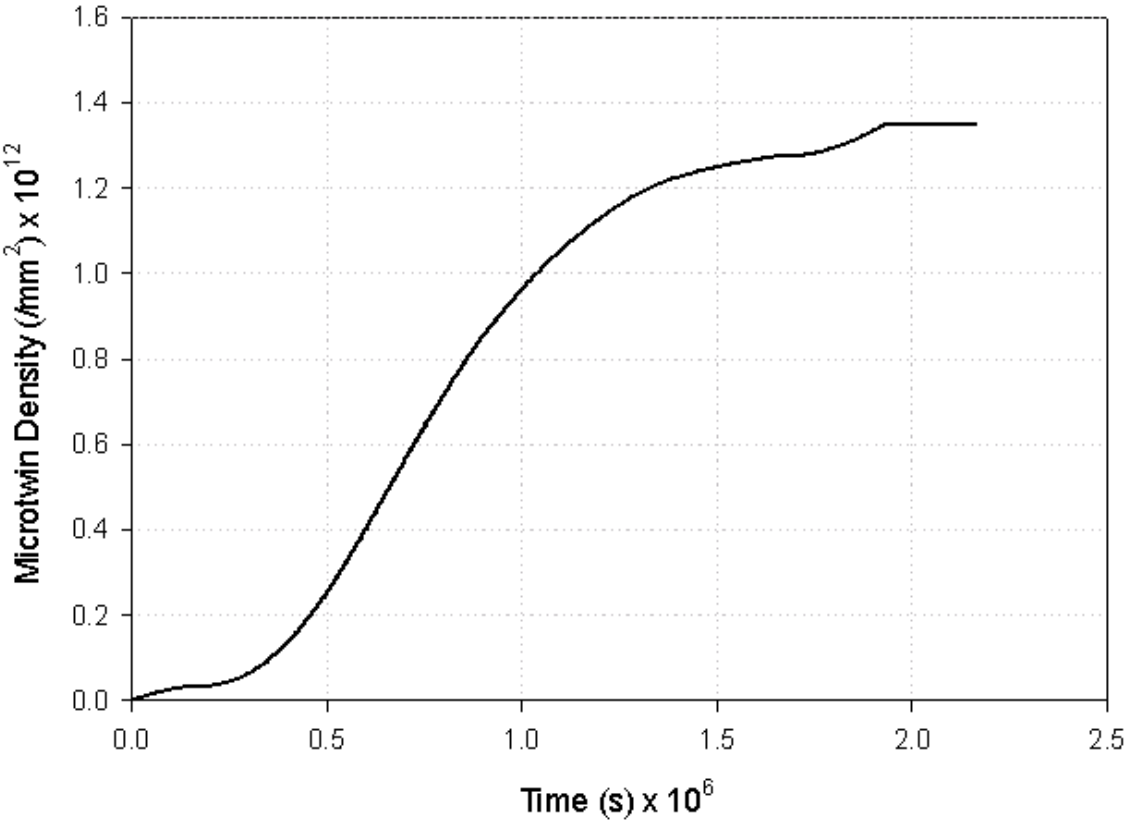

Figure 5.12 Microtwin density on microtwinning system under stress-controlled creep loading condition at 838 MPa.

CHAPTER 6

SUMMARY AND CONCLUSIONS

6.1 Conclusions

In this thesis, a multilevel hierarchical modeling scheme of a constitutive relation is developed for Ni-base superalloys to predict the macroscopic mechanical response under various conditions. The performance of aircraft turbine engines can be greatly improved by enhancing the high temperature strength and creep resistance of Ni-base superalloys, which are influenced by the microstructure and related deformation mechanisms. The microstructure attributes of Ni-base superalloys can be controlled by thermomechanical processing (heat treatment and cooling rate schedule), but implementing microstructure sensitive constitutive relations, such as a crystal plasticity model, at a component level is computationally impractical (Kozar et al., 2009). Furthermore, experimentally characterizing microstructure sensitivity and implementing the results in an empirical macroscale model requires significant time and monetary resources. Therefore, a multilevel hierarchical scheme for a constitutive model is extremely desirable, as fine length scale phenomena can be implicitly embedded in the component level macroscale model. The constitutive relation can also be employed to predict the mechanical response of the material such as stress-strain response, crack growth, creep behavior or fatigue crack initiation life. Additionally, the hierarchical modeling framework should provide a

generic constitutive relation that can estimate the material response over a sufficiently wide range of conditions (microstructure, temperature and load histories).

The framework developed in this thesis uses information from phase field model simulations at the length scale of tertiary γ′ precipitates (~10 nm) to augment a crystal plasticity model at the length scale of grains (5-30 μm), ultimately informing a macroscale viscoplastic ISV model.

A modified Chaboche-type macroscale viscoplastic ISV model with a two term flow rule is used to capture complex behaviors of Ni-base superalloys at the component scale. The model is formulated with various evolving ISVs that include the isotropic hardening variable and the two-term back stress. In order to efficiently calibrate the macro ISV model parameters to multiple complex experimental data, a three-level hierarchical parameter estimation scheme and a parameter clustering strategy have been developed. The level 1 parameter estimation scheme is conducted on multiple partitions of an experiment, and influential clusters of parameters are optimized using ModelCenter 9.0 (Phoenix Integration, Inc., 2009). At the level 2 of the parameter estimation scheme, the quantified discrepancies obtained from partitions of an experiment are combined into a single total error and used as the objective of parameter estimation. Finally, the level 3 of the parameter estimation scheme is employed to multiple experimental tests on a material in order to identify a single set of constitutive model parameters that can produce responses adequately close to experiments.

The microstructure-sensitive crystal plasticity model at length scales of grains has been designed to incorporate microtwinning, which has recently gained attention as a significant deformation mechanism under creep conditions at intermediate temperatures.

Simulations obtained from the phase field model can provide insights on the dislocation dissociation mechanism, which is known to be a precursor of microtwinning. Based on phase field model simulation results, the dislocation dissociation process is controlled by the resolved shear stresses acting on the leading and trailing partial slip systems. Using the criteria set by the resolved shear stresses on each slip system of the crystal plasticity model, the shearing rate induced by microtwinning has been implemented into the flow rule of the crystal plasticity model using the Orowan equation (Karthikeyan et al., 2006).

The crystal plasticity model, modified to implement microtwinning, is analyzed by conducting simulations with strain- and stress-controlled loading on a finite element model. The evolution of state variables on slip systems has been analyzed on randomly selected elements of the finite element model. It was confirmed that the role of microtwinning under creep condition is substantial, whereas effect of microtwinning is shown to be minimal under cyclic loading with a reasonably high strain rate; this observation coincides with experimental observations.

Neither the crystal plasticity nor the macroscale ISV model has been completely validated, as experimental data with corresponding detailed microstructure are not yet available to calibrate the parameters. However, a hierarchical modeling scheme has been completely formulated and a link across length scales has been established. Additionally, the hierarchical parameter estimation scheme supports an effective way to formulate the hierarchical model of the constitutive relation, which can be applied to a critical component level with the microstructure-sensitivity.

6.2 Recommendations for Future Work

The present work establishes a complete framework of the hierarchical multiscale modeling scheme, but some details are absent. Various improvements can be made on the established multiscale hierarchical framework as follows:

- The model can be further improved by obtaining an ore extensive database of the phase field model results such as the effects of precipitate morphology, size, volume fractions and distributions. Once available, such information can be implemented in the crystal plasticity model as coefficients associated with the microtwinning process and can be compared to microtwinning dominant experimental responses.
- Experimentally, a wide range of microstructures with complex loading histories under various conditions (e.g., temperature and strain rate) can ensure the validity of microstructure sensitivity. Also, a TEM analysis of microstructures such as the distributions of γ matrix channel width, morphology and sizes of γ' precipitate can support the fine scale models used in the hierarchical scheme. Furthermore, microstructural details and deformation mechanism observations obtained from interrupted creep experiments can improve understanding of the microtwinning density evolution as well as understanding of the coarsening effect of γ' particles observed under creep.
- The crystal plasticity model assumes constant microstructure attributes (γ' precipitate sizes, volume fractions and grain sizes). Once the evolving relation of microstructure attributes is known, the microstructure sensitive crystal plasticity

model should be updated to apply such variations with respect to time. Also, turbine disks are manufactured so that the microstructure within the component is gradually varied for optimum performance. Therefore, the crystal plasticity model and the finite element model should be able to assess and assign a gradient to the microstructure attributes (e.g., γ' precipitate sizes and volume fractions) with respect to the location of the component. This capability can provide a concurrent component-material design tool for turbine disks.

- The hierarchical parameter estimation scheme and parameter clustering strategy have to be modified for the crystal plasticity model. The hierarchical parameter estimation scheme for the crystal plasticity model should also employ different sizes of finite element models so that a small model is used for the parameter estimation step with multiple iterations, whereas a large model is used only for validation purposes.
- Once an artificial neural network is trained with experimental data and the calibrated crystal plasticity model, parametric studies and microstructure sensitivity analysis should be conducted.

REFERENCES

ABAQUS (2006) Version 6.7, Simulia Inc., Providence, RI.

Ardakani, M. G., McLean, M., and Shollock, B. A. (1999). "Twin formation during creep in single crystals of nickel-based superalloys." *Acta Materialia*, 47(9), 2593-2602.

Asaro, R. J. (1983). "Micromechanics of crystals and polycrystals." *Advances in Applied Mechanics*, 23, 1-115.

Cailletaud, G., and Chaboche, J. L. (1979). "Macroscopic description of the microstructural changes induced by varying temperature: example of IN100 cyclic behaviour." 2, 23-32.

Chaboche, J. L. (1983). "ON THE CONSTITUTIVE EQUATIONS OF MATERIALS UNDER MONOTONIC OR CYCLIC LOADINGS." *Recherche Aerospatiale (English Edition)*(5), 31-43.

Chaboche, J. L. (1989). "Constitutive equations for cyclic plasticity and cyclic viscoplasticity." *International Journal of Plasticity*, 5(3), 247-302.

Estrin, Y., and Mecking, H. (1984). "A unified phenomenological description of work hardening and creep based on one-parameter models." *Acta Metallurgica*, 32(1), 57-70.

Frederick, C. O., and Armstrong, P. J. (1966). "Convergent internal stresses and steady cyclic states of stress." *Journal of Strain Analysis*, 1(2), 154-159.

Gabb, T., P., Garg, A., Ellis, D., L., and O'Connor, K., M. (2004). "Detailed Microstructural Characterization of the Disk Alloy ME3." *NASA Technical Memorandum*, E-14533.

Haddou, H., Risbet, M., Marichal, G., and Feaugas, X. (2004). "The effects of grain size on the cyclic deformation behaviour of polycrystalline nickel." *Materials Science and Engineering: A*, 379(1-2), 102-111.

Kakehi, K. (2000). "Effect of plastic anisotropy on the creep strength of single crystals of a nickel-based superalloy." *Metallurgical and Materials Transactions A*, 31(2), 421-430.

Karthikeyan, S., Unocic, R. R., Sarosi, P. M., Viswanathan, G. B., Whitis, D. D., and Mills, M. J. (2006). "Modeling microtwinning during creep in Ni-based superalloys." *Scripta Materialia*, 54(6), 1157-1162.

Khan, A. S., and Huang, S. (1995). *Continuum theory of plasticity*, Wiley., New York.

Knowles, D. M., and Chen, Q. Z. (2003). "Superlattice stacking fault formation and twinning during creep in γ γ / γ ' single crystal superalloy CMSX-4." *Materials Science and Engineering A*, 340(1-2), 88-102.

Kolbe, M. (2001). "The high temperature decrease of the critical resolved shear stress in nickel-base superalloys." *Materials Science and Engineering A*, 319-321, 383-387.

Kovarik, L., Unocic, R. R., Li, J., and Mills, M. J. (2009a). "The intermediate temperature deformation of Ni-based superalloys: Importance of reordering." *JOM*, 61(2), 42-48.

Kovarik, L., Unocic, R. R., Li, J., Sarosi, P., Shen, C., Wang, Y., and Mills, M. J. (2009b). "Microtwinning and other shearing mechanisms at intermediate temperatures in Ni-based superalloys." *Progress in Materials Science*, 54(6), 839-873.

Kozar, R. W., Suzuki, A., Milligan, W. W., Schirra, J. J., Savage, M. F., and Pollock, T. M. (2009). "Strengthening Mechanisms in Polycrystalline Multimodal Nickel-Base Superalloys." *Metallurgical and Materials Transactions A*, 40(7), 1588-1603.

Lee, D., and Zaverl Jr, F. (1978). "GENERALIZED STRAIN RATE DEPENDENT CONSTITUTIVE EQUATION FOR ANISOTROPIC METALS." 26(11), 1771-1780.

Li, J., and Wahi, R. P. (1995). "Investigation of γ / γ ' lattice mismatch in the polycrystalline nickel-base superalloy IN738LC: Influence of heat treatment and creep deformation." *Acta Metallurgica et Materialia*, 43(2), 507-517.

Lowe, T. C., and Miller, A. K. (1984). "IMPROVED CONSTITUTIVE EQUATIONS FOR MODELING STRAIN SOFTENING - PART I: CONCEPTUAL DEVELOPMENT." *Journal of Engineering Materials and Technology, Transactions of the ASME*, 106(4), 337-342.

MacLachlan, D. W., Wright, L. W., Gunturi, S., and Knowles, D. M. (2001). "Constitutive modelling of anisotropic creep deformation in single crystal blade alloys SRR99 and CMSX-4." *International Journal of Plasticity*, 17(4), 441-467.

Malinin, N. N., and Khadjinsky, G. M. (1972). "Theory of creep with anisotropic hardening." *International Journal of Mechanical Sciences*, 14(4), 235-246.

Manonukul, A., Dunne, F. P. E., and Knowles, D. (2002). "Physically-based model for creep in nickel-base superalloy C263 both above and below the γ solvus." *Acta Materialia*, 50(11), 2917-2931.

McDowell, D. L. "Two surface model for transient nonproportional cyclic plasticity: part 1. development of appropriate equations." Albuquerque, NM, USA, ASME, New York, NY, USA; ASCE, New York, NY, USA.

McDowell, D. L. (1992). "Nonlinear kinematic hardening theory for cyclic thermoplasticity and thermoviscoplasticity." *International Journal of Plasticity*, 8(6), 695-728.

McDowell, D. L. (2008). "Viscoplasticity of heterogeneous metallic materials." *Materials Science and Engineering: R: Reports*, 62(3), 67-123.

McGinty, R. D. (2001). "Multiscale representation of polycrystalline inelasticity," Georgia Institute of Technology.

Mecking, H., and Kocks, U. F. (1981). "Kinetics of flow and strain-hardening." *Acta Metallurgica*, 29(11), 1865-1875.

Moosbrugger, J. C., and McDowell, D. L. "On a class of kinematic hardening rules for nonproportional cyclic plasticity." Chicago, IL, USA, 79-89.

Mourer, D. P., and Williams, J. L. "Dual heat treat process development for advanced disk applications." Champion, PA, United states, 401-407.

Nouailhas, D. (1989). "Unified modelling of cyclic viscoplasticity. Application to austenitic stainless steels." *International Journal of Plasticity*, 5(5), 501-520.

Ohno, N. (1982). "CONSTITUTIVE MODEL OF CYCLIC PLASTICITY WITH A NONHARDENING STRAIN REGION." *Journal of Applied Mechanics, Transactions ASME*, 49(4), 721-727.

Paidar, V., Pope, D. P., and Vitek, V. (1984). "A theory of the anomalous yield behavior in L12 ordered alloys." *Acta Metallurgica*, 32(3), 435-448.

Przybyla, C. P., and McDowell, D. L. (2010). "Microstructure-sensitive extreme value probabilities for high cycle fatigue of Ni-base superalloy IN100." *International Journal of Plasticity*, 26(3), 372-394.

Raujol, S., Benyoucef, M., Locq, D., Caron, P., Pettinari, F., Clement, N., and Coujou, A. (2006). "Decorrelated movements of Shockley partial dislocations in the -phase channels of nickel-based superalloys at intermediate temperature." *Philosophical Magazine*, 86(9), 1189-1200.

Reed, R. C. (2006). *The superalloys: fundamentals and applications*, Cambridge University Press., Cambridge.

Sarosi, P. M., Viswanathan, G. B., and Mills, M. J. (2006). "Direct observation of an extended complex stacking fault in the γ' phase of a Ni-base superalloy." *Scripta Materialia*, 55(8), 727-730.

Schwertel, J., and Schinke, B. (1996). "Automated Evaluation of Material Parameters of Viscoplastic Constitutive Equations." *Journal of Engineering Materials and Technology*, 118(3), 273-280.

Sheh, M. Y., and Stouffer, D. C. (1990). "A crystallographic model for the tensile and fatigue response for Rene N4 at 982C." *Transactions of the ASME. Journal of Applied Mechanics*, 57(1), 25-31.

Shen, C., Mills, M. J., and Wang, Y. (2003). "Modeling Dislocation Dissociation and Cutting of γ' Precipitates in Ni-Based Superalloys by the Phase Field Method." *Materials Research Society Symposium*, v 753, p 309-314.

Shenoy, M. (2006). "Constitutive modeling and life prediction in nickel-base superalloys," Georgia Institute of Technology.

Stevens, R. A., and Flewitt, P. E. J. (1979). "The effects of γ' precipitate coarsening during isothermal aging and creep of the nickel-base superalloy IN-738." *Materials Science and Engineering*, 37(3), 237-247.

Svoboda, J., Fischer, F. D., and Fratzl, P. (2006). "Diffusion and creep in multi-component alloys with non-ideal sources and sinks for vacancies." *Acta Materialia*, 54(11), 3043-3053.

Tong, J., Zhan, Z. L., and Vermeulen, B. (2004). "Modelling of cyclic plasticity and viscoplasticity of a nickel-based alloy using Chaboche constitutive equations." *International Journal of Fatigue*, 26(8), 829-837.

Unocic, R. R., Viswanathan, G. B., Sarosi, P., Karthikeyan, S., Li, J., and Mills, M. J. (2008). "Mechanisms of creep deformation in polycrystalline Ni-base disk superalloys." *Materials Science and Engineering A*, 483-484(1-2C), 25-32.

Viswanathan, G. B., Karthikeyan, S., Sarosi, P. M., Unocic, R. R., and Mills, M. J. (2006). "Microtwinning during intermediate temperature creep of polycrystalline Ni-based superalloys: mechanisms and modelling." *Philosophical Magazine*,, Vol. 86(Nos. 29–31), 4823–4840.

Viswanathan, G. B., Sarosi, P. M., Henry, M. F., Whitis, D. D., Milligan, W. W., and Mills, M. J. (2005). "Investigation of creep deformation mechanisms at intermediate temperatures in René 88 DT." *Acta Materialia*, 53(10), 3041-3057.

Yaguchi, M., Yamamoto, M., and Ogata, T. (2002). "A viscoplastic constitutive model for nickel-base superalloy, part 1: kinematic hardening rule of anisotropic dynamic recovery." *International Journal of Plasticity*, 18(8), 1083-1109.

Zhan, Z. L., and Tong, J. (2007). "A study of cyclic plasticity and viscoplasticity in a new nickel-based superalloy using unified constitutive equations. Part II: Simulation of cyclic stress relaxation." *Mechanics of Materials*, 39(1), 73-80.

Zhao, L. G., Tong, J., Vermeulen, B., and Byrne, J. (2001). "On the uniaxial mechanical behaviour of an advanced nickel base superalloy at high temperature." *Mechanics of Materials*, 33(10), 593-600.